NUMERICAL SIMULATION OF FLOW AND HEAT TRANSFER OF INTERNAL COOLING PASSAGE IN GAS TURBINE BLADE

A Dissertation

by

GUOGUANG SU

Submitted to the Office of Graduate Studies of
Texas A&M University
in partial fulfillment of the requirements for the degree of

DOCTOR OF PHILOSOPHY

December 2005

Major Subject: Mechanical Engineering

NUMERICAL SIMULATION OF FLOW AND HEAT TRANSFER OF INTERNAL COOLING PASSAGE IN GAS TURBINE BLADE

A Dissertation

by

GUOGUANG SU

Submitted to the Office of Graduate Studies of
Texas A&M University
in partial fulfillment of the requirements for the degree of

DOCTOR OF PHILOSOPHY

Approved by:

Co-Chairs of Committee,	Je-Chin Han
	Hamn-Ching Chen
Committee Members,	N. K. Anand
	Sai Lau
Head of Department,	Dennis O'Neal

December 2005

Major Subject: Mechanical Engineering

ABSTRACT

Numerical Simulation of Flow and Heat Transfer of Internal Cooling Passage in Gas Turbine Blade. (December 2005)

Guoguang Su, B.S., Chongqing University, Chongqing, China;

M.S., Chinese Academy of Science, Beijing, China

Co-Chairs of Advisory Committee: Dr. Je-Chin Han
Dr. Hamn-Ching Chen

A computational study of three-dimensional turbulent flow and heat transfer was performed in four types of rotating channels.

The first type is a rotating rectangular channel with V-shaped ribs. The channel aspect ratio (AR) is 4:1, the rib height-to-hydraulic diameter ratio (e/D_h) is 0.078 and the rib pitch-to-height ratio (P/e) is 10. The rotation number and inlet coolant-to-wall density ratio were varied from 0.0 to 0.28 and from 0.122 to 0.40, respectively, while the Reynolds number was varied from 10,000 to 500,000. Three channel orientations (90 degrees, −135 degrees, and 135 degrees from the rotation direction) were also investigated.

The second type is a rotating rectangular channel with staggered arrays of pin-fins. The channel aspect ratio (AR) is 4:1, the pin length-to-diameter ratio is 2.0, and the pin spacing-to-diameter ratio is 2.0 in both the stream-wise and span-wise directions. The rotation number and inlet coolant-to-wall density ratio varied from 0.0 to 0.28 and from 0.122 to 0.20, respectively, while the Reynolds number varied from 10,000 to

100,000. For the rotating cases, the rectangular channel was oriented at 150 degrees with respect to the plane of rotation.

In the rotating two-pass rectangular channel with 45-degree rib turbulators, three channels with different aspect ratios (AR=1:1; AR=1:2; AR=1:4) were investigated. Detailed predictions of mean velocity, mean temperature, and Nusselt number for two Reynolds numbers (Re=10,000 and Re=100,000) were carried out. The rib height is fixed as constant and the rib-pitch-to-height ratio (P/e) is 10, but the rib height-to-hydraulic diameter ratios (e/D_h) are 0.125, 0.094, and 0.078, for AR=1:1, AR=1:2, and AR=1:4 channels, respectively. The channel orientations are set as 90 degrees, the rotation number and inlet coolant-to-wall density ratio varied from 0.0 to 0.28 and from 0.13 to 0.40, respectively.

The last type is the rotating two-pass smooth channel with three aspect ratios (AR=1:1; AR=1:2; AR=1:4). Detailed predictions of mean velocity, mean temperature and Nusselt number for two Reynolds numbers (Re=10,000 and Re=100,000) were carried out. The rotation number and inlet coolant-to-wall density ratio varied from 0.0 to 0.28 and from 0.13 to 0.40, respectively.

A multi-block Reynolds-averaged Navier-Stokes (RANS) method was employed in conjunction with a near-wall second-moment turbulence closure.

To my daughter

ACKNOWLEDGMENTS

I would like to express my sincere appreciation to my advisors , Dr. Je-Chin Han and Dr. Hamn-Ching Chen, for their patience and insightful guidance without which I could not have finished my dissertation. I am also grateful to my academic committee members, Dr. N. K. Anand and Dr. Sai Lau, for their valuable time and helpful guidance.

Acknowledgements should also go to my colleagues from the Turbine Heat Transfer Laboratory for their valuble discussions with me.

I am most grateful to my wife for her patience and sacrifice. I believe this work would not have been possible without her.

The computations were performed on the K2 supercomputer at the Texas A&M Supercomputer Center under a supercomputer research grant. Their support is greatly appreciated.

TABLE OF CONTENTS

Page

CHAPTER Page

LIST OF FIGURES

Page

Page

Page

Page

Page

Page

Page

LIST OF TABLES

TABLE Page

CHAPTER I

INTRODUCTION

Gas turbines are extensively used for aircraft propulsion, land-based power generation, and industrial applications. There is a strong demand for efficient energy utilization; one of the most powerful means of achieving higher efficiency in industrial gas turbine engines is to raise the turbine inlet temperature (TIT). Sophisticated cooling techniques must be employed to cool the components to maintain the performance requirements. A widely used method for cooling turbine blades is to bleed lower-temperature air from the compressor and circulate it within and around each blade. The coolant typically flows through a series of straight ducts connected by 180° turns and roughened with ribs or pin fins to enhance heat transfer. Fig. 1.1 shows the basic concept of common cooling technique in gas turbine.

The channel bend complexes the flow physics, the presence of turbulators (rib, pin and dimples) adds a further complexity since these turbulators produce complex flow fields such as flow separation, reattachment and secondary flow, which produce a high turbulence level that leads to high heat transfer coefficients. The rotation of the turbine blade cooling passages adds another complexity to the problem. It gives rise to Coriolis and buoyancy forces that can significantly alter the local heat transfer in the internal coolant passages from the non-rotating channels. The complex coupling of the Coriolis

---

This dissertation follows the style of Journal of the Thermophysics and Heat Transfer.

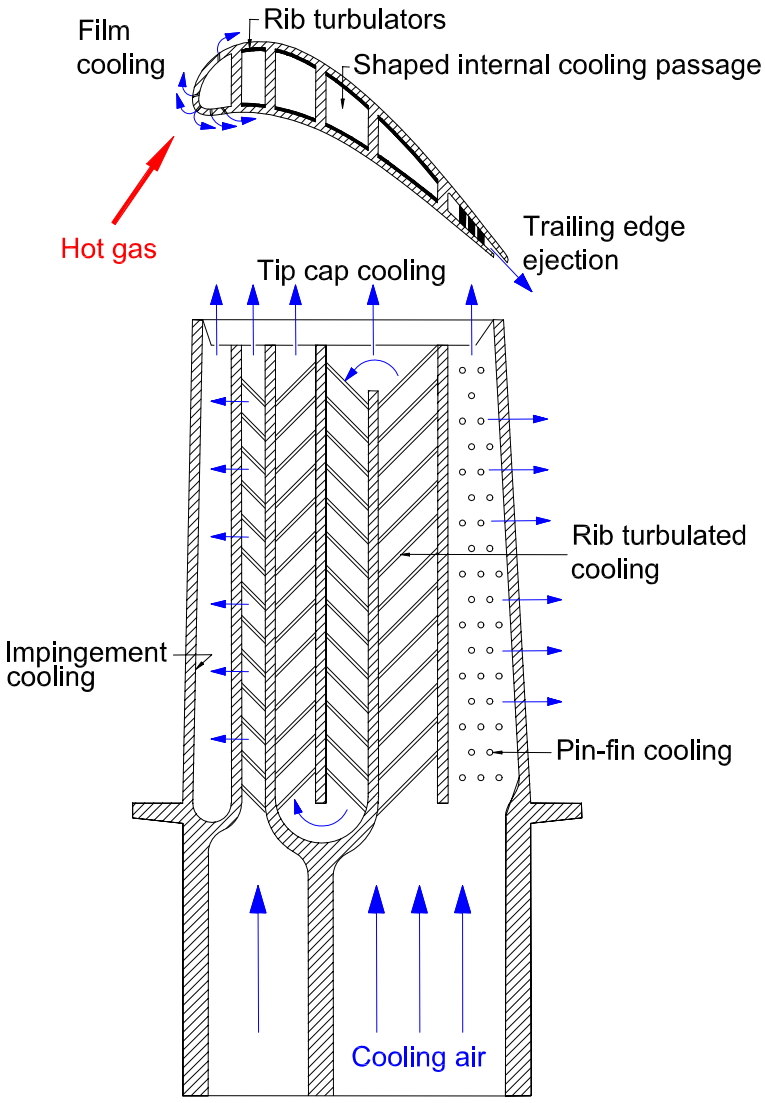

Fig.1.1 Conceptual View of Internal Cooling Passage in a Gas Turbine

and buoyancy forces with flow separation/reattachment by ribs or pin fins has prompted many investigators to study respectively, therefore several topics will grouped in the following literature survey.

1.1 Literature Survey

Part I. Coolant passage with rib turbulators

Several studies have been made to predict numerically the flow and heat transfer in rotating smooth and ribbed ducts. Stephens et al.[1, 2] studied inclined ribs in a straight non-rotating square duct. Lin et al.[3] investigated the effect of angled ribs on the heat transfer coefficients in a rotating two-passage duct using a shear-stress transport (SST) turbulence model. They studied the effects of Reynolds numbers, rotation numbers, and buoyancy parameters. Prakash and Zerkle[4], employing a high Reynolds number k-ε turbulence model with wall function, performed a numerical prediction of flow and heat transfer in a rectangular duct with 90° ribs with and without rotation. However, their calculations used periodicity and neglected buoyancy effects. They suggested that a low Reynolds number turbulence model is necessary to simulate real gas turbine engine conditions and a Reynolds stress model is required to capture anisotropic effects. Bonhoff et al.[5] calculated the heat transfer coefficients and flow fields for rotating U-shaped coolant channels with 45° angled ribs. They used a Reynolds stress turbulence model with wall functions in the FLUENT CFD code. Using the periodicity of the flow, Iacovides[6] computed flow and temperature fields in a rotating straight duct with 90° ribs. Two zonal models of turbulence were tested: a k-ε with an one-equation model of k

transport across the near-wall region and a low-*Re* differential stress model. He concluded that the differential stress model thermal computations were clearly superior to those of the *k*-ε/one-equation model.

Chen et al.[7,8] employed a multi-block numerical method for the calculation of three-dimensional flow and heat transfer in rotating two-pass square channels (AR=1:1) with smooth walls. Using the same model, Jang et al.[9, 10] studied flow and heat transfer behavior in a non-rotating two-pass square channels with 60° and 90° ribs, respectively. Their results were in good agreement with Ekkad and Han's[11] detailed heat transfer data, and demonstrated the second-moment closure model superiority in predicting flow and heat transfer characteristics in the ribbed duct. In a later study, Jang et al.[12] predicted flow and heat transfer in a rotating square channel with 45° angled ribs by the same second-moment closure model. Heat transfer coefficient prediction matched very well with the data obtained by Johnson et al.[13] for both stationary and rotating cases. Al-Qahtani et al.[14] predicted flow and heat transfer in a rotating two-pass rectangular channel (AR = 4:1) with 45° angled ribs using the second-moment closure model of Chen et al.[7, 8] Their heat transfer coefficient prediction was compared with the data of Azad et al.[15] for both stationary and rotating cases. Their study predicted fairly well the complex three-dimensional flow and heat transfer characteristics resulting from angled ribs, sharp 180° turn, rotation, centrifugal buoyancy forces, and channel orientation. Al Qahtani et al.[16] also conducted a numerical study of flow and heat transfer in one-pass rotating rectangular channels (AR = 4:1) with 45-degree rib turbulators using the same second-moment closure model. Their flow and heat transfer predictions were in good

agreement with the experimental data of Griffith et al.[17] Using a Reynolds stress turbulence model, Jia et al.[18] predicted local heat transfer and fluid flow characteristics in straight stationary square ducts with transverse and V-shaped ribs for Reynolds number from 14,000 to 35,000. They concluded that V-shaped ribs pointing upstream performed superior to V-shaped ribs pointing downstream and transverse ribs.

In addition to the numerical studies mentioned above, there were several experimental studies focused on internal cooling passages in non-rotating ducts, such as Han and Park [19], Han et al.[20], Ekkard and Han[11], and Liou et al.[21] Wagner et al.[22], Dutta and Han[23], Soong et al.[24] and Azad et al.[15] investigated rotating ducts with smooth and ribbed walls. Wagner et al.[25], Johnson et al.[13, 26], Parsons et al.[27] and Zhang et al.[28] reported studies on rotating square channels with normal and angled ribs. Azad et al.[15] also investigated the effect of channel orientation on rotating ribbed two pass rectangular channel. Griffith et al.[17] studied the effect of channel orientation on rotating smooth and ribbed rectangular channels with channel aspect ratio of 4:1. They investigated a broad range of flow parameters including Reynolds number (Re = 5,000 – 40,000), rotation number (Ro = 0.04 – 0.3) and coolant to wall density ratio ($\Delta\rho/\rho$= 0.122).

The present study is concerned specifically with the numerical prediction of flow and heat transfer in rectangular channels with V-shaped ribs. Several experimental studies have been conducted to investigate the heat transfer enhancement in square and rectangular channels with V-shaped ribs. Han et al.[20] found that the 60° and 45° V-shaped ribs perform better than the 60° and 45° parallel angled ribs in square channels. Ekkad and Han[11] also showed that the non-rotating square channel with 60° V-shaped rib

produced more heat transfer enhancement than 60° and 90° angled ribbed channels. Al-Hadhrami et al.[29, 30] studied the effect of rotation on heat transfer in rotating two-pass square and rectangular channels (AR = 2:1) with rib turbulators for five different channel orientations. They found that the parallel and V-shaped ribs produced better heat transfer enhancement than the crossed and inverted V-shaped ribs. Lee et al.[31] studied the heat transfer in rotating rectangular channels (AR = 4:1) with V-shaped and angled rib turbulators with and without gaps. They concluded that the V-shaped ribs produced more heat transfer enhancement than the angled ribs for both the stationary and rotating cases, and the enhancement on both the leading and trailing surfaces increases with rotation. The experimental results of Lee et al.[31] for narrow rectangular channels (AR = 4:1) with V-shaped ribs provided a validation database for the present work.

The above experimental studies show that V-shaped ribs produce overall better heat transfer enhancement than the angled ribs. However, the effects of rotation, channel orientation and large channel aspect ratio on the secondary flow and heat transfer calculations in rectangular channels with V-shaped ribs have not been systematically investigated in previous numerical studies. Furthermore, there is no reported information on the flow and heat transfer behaviors in stationary/rotating rectangular channels with V-shaped ribs under very high Reynolds number flow conditions ($Re \sim 500{,}000$).

Part II. Cooling passage with pin-fins

Many experimental investigations have proven that pin-fins perform better in low aspect ratio channels for gas turbine blades. Metzger et al. [32] studied the developing heat

transfer of short pin-fins in stationary staggered arrays. They observed that the heat transfer coefficient gradually increases over the first several rows of pins, reaches a maximum around the third row, and gradually decreases through the remaining rows of the array. Metzger and Haley [33] then studied the effects of pin material and pin spacing on heat transfer in staggered arrays. They found that the Nusselt number values for the non-conducting pin-fins closely followed the values of the conducting pin-fins. They also showed that as the stream-wise spacing was increased, the Nusselt number values decreased. Later, Metzger et al. [34] examined the row resolved heat transfer variation in pin-fin arrays. VanFossen [35] also investigated stationary cooling channels with pin-fin arrays. The study showed that the heat transfer from an array of short pins is lower than the heat transfer from an array of long pins. It was also found that the heat transfer coefficients on the pin surface were approximately 35% greater than those on the endwall. In a later study, Brigham and VanFossen [36] investigated the effect of pin-fin length on the heat transfer coefficient and concluded that the pin height-to-diameter ratio is the dominant factor affecting the amount of heat transferred from short pin-fin arrays (end walls included). With the mass transfer technique, Chyu and Goldstein [37] observed the peak distribution of the Sherwood number and concluded that the staggered pin arrangement performs better than inline arrangement.

In more recent studies, Chyu and Hsing [38] investigated the effect of pin shape on heat transfer. They concluded that the cubic pin-fin yields the highest heat transfer (in both staggered and inline arrays), followed by the diamond and then the circular pin-fins. Chyu et al. [39] also studied the heat transfer contribution of pin-fins and end walls in pin-

fin arrays. This study found that conducting pin-fins have a significantly higher heat transfer coefficient (10 to 20%) than the end walls. Uzol and Camci[40] investigated the end wall heat transfer and total pressure loss within various arrays of pin-fins. This investigation used a liquid crystal technique to measure the end wall heat transfer downstream of two rows of fins. This study compared the heat transfer enhancement of circular pins and two elliptical pin-fin arrays. They found that the heat transfer in the wake of circular pins is 25% higher than that of the elliptical arrays. However, the elliptical geometry is viewed as a more desirable configuration due to the relatively small pressure drop penalty (when compared to the circular array).

Hwang et al.[41,42] presented experimental heat transfer and pressure drop results for air flows through trapezoidal pin-fin channels with the liquid crystal technique. They concluded that straight wedge duct with a staggered pins array produces the highest heat transfer coefficient enhancement with a moderate pressure drop penalty.

Lau et al.[43] conducted experiments to study the effects of lateral ejection through slots on the local wall heat transfer and the pressure drop for turbulent flow through a pin fin channel. They found that the heat transfer is higher in the vicinity of the ejection slots adjacent to the channel entrance. Lau et al [44] conducted experiments to study the effects of lateral flow ejection on the overall heat transfer and pressure drops. They found that the overall Nusselt number decreased by as much as 25% as the ejection ratio was increased. Lau et al.[45] also examined the effects of the length of the trailing edge holes on the heat transfer, pressure drops, and mass flow rates in pin fin channels.

In an experiment conducted by Willett and Bergles[46], the heat transfer in rotating channels with conducting pin-fins was studied. They found that the heat transfer enhancement due to rotation and buoyancy was much less than the enhancement observed from their study of a smooth narrow duct (Willett and Bergles[47]). They showed that pin-fins significantly reduce the effect of rotation, but they do not eliminate the effect. Wright et al.[48] studied a staggered array of pins under the rotating condition and found that the heat transfer in a stationary pin-fin channel can be enhanced up to 3.8 times that of a smooth channel, and they confirmed the finding of Willett and Bergles[46] that the effect of rotation is mitigated in the pin-fin channel.

Recently, Donahoo et al.[49] employed a Galerkin finite element procedure to perform a 2D study of a staggered cross pin array to determine an optimal row spacing considering both heat dissipation and required pumping power. Subsequently, Donahoo et al.[50] performed a 3D calculation with the k-ε turbulence model to study the same problem including the end wall effects. More recently, Hamilton et al.[51] used the ANSYSTM commercial code to model the incompressible fluid flow in a pin-fin channel using the standard k-ε turbulence model in conjunction with the Van Driest coupling model for the wall region. In general the few numerical studies in the literature primarily focus on the cooling techniques in electric circuit cooling or the shell and tube heat exchangers. Although there are some similarities with the pin-fin channels in gas turbine blades, these simulation results are not directly applicable for turbine blade cooling applications at high Reynolds number and high rotation number conditions.

Part III. Two-pass cooling passage with low aspect ratio

As mentioned in **Part I,** there are a lots of experiment study in the two-pass duct, Parsons et al.[52,53] studied the effects of channel orientation and wall heating condition on the local heat transfer coefficients in a rotating two-pass square channel with ribbed walls. They found that the effect of the Coriolis force and cross-stream flow were reduced as the channel orientation changed from the normal β=90° to an angled orientation of β=135°. Dutta and Han[23] also investigated the local heat transfer coefficients in rotating smooth and ribbed two-pass square channels with three channel orientations. Dutta et al.[54] presented experimental heat transfer results for turbulent flow through a rotating two-pass rib-roughened triangular channel for two channel orientations with respect to the axis of rotation. In addition, Park and Lau[55] and Park et al.[56] conducted experimental work using naphthalene sublimation to study the effects of the Coriolis force, 180° turn, channel orientation, and the different rib arrangements on local heat/mass transfer distributions on the leading and trailing walls of a two-pass square channel. Chen et al.[57] used naphthalene sublimation method to measure the detailed mass transfer along four walls of a square duct containing a sharp 180° bend with normal ribs on two opposite walls under the non-rotating condition. They found that the ribbed walls have more span-wise uniformity than the smooth side walls. Al-Hadhrami and Han[58] studied the rotation effect on heat transfer in a rotating two pass square duct with five different orientations of 45° angled rib turbulators. They concluded that the parallel rib orientation (ribs in first and second passes are parallel and ribs on

leading and trailing walls are parallel) provides higher overall Nusselt number ratio than cross rib orientation, particularly, for the increased rotation numbers.

Liou et al.[59] studied the effect of divider thickness in a two pass non-rotating smooth square duct. They found the turn effect can extend up to 8 hydraulic diameters downstream of the turn. Liou and Chen[60,61] studied the heat transfer and flow field in two pass rotating smooth duct with AR=1:1 and 1.25. They concluded that the rotation effect raises the turbulence level near the leading or trailing walls, which in turn leads to the local heat transfer enhancement.

The limitation in experiment demands the numerical study in the two-pass channel. Lin et al.[3] used a shear-stress transport (SST) turbulence model in the investigation of heat transfer in a rotating two-passage square duct. Chen et al.[7,8] employed a multi-block numerical method for the calculation of three-dimensional flow and heat transfer in rotating two-pass square channels (AR=1:1) with smooth walls. Using the same model, Jang et al.[9,10] studied flow and heat transfer behavior in a non-rotating two-pass square channel with 60-deg and 90-deg ribs. Their results were in good agreement with experiment data. In a later study, Jang et al.[12] predicted flow and heat transfer in a rotating square channel with 45-deg angled ribs by the same second moment closure model. More recently, Al-Qahtani et al.[14] predicted flow and heat transfer in rotating two-pass rectangular channels (AR=2:1) with 45-deg rib turbulators. These results demonstrated the capability of the second-moment closure model for accurate prediction of sophisticated cooling channel configurations.

Almost all of the studies have focused on square or close to square ducts and the previous numerical research focused on the validation of turbulence models and the physical behavior of the flow and heat transfer in the square duct (AR=1:1) or channels with aspect ratios greater than one (AR=2:1, and AR=4:1). However, confined by the blade configurations, the cooling passage should include not only these higher aspect ratio ducts, but also the lower aspect ratio ducts, such as the AR=1:2 and AR=1:4 channels considered in the present study.

1.2 Research Objectives

The objective of this study is to use the second-moment RANS method of Chen et al.[7, 8] (1) to predict the three-dimensional flow and heat transfer for rotating one-pass rectangular ducts (AR = 4:1) with V-shaped ribs and compare with the experimental data of Lee et al.[31]; (2)to evaluate the effects of lower aspect ratio rectangular smooth channels (AR = 1:1, AR = 1:2, and AR = 1:4) on heat transfer for both the non-rotating and rotating conditions; (3) to evaluate the effects of lower aspect ratio rectangular ribbed channels (AR = 1:1, AR = 1:2, and AR = 1:4) on heat transfer for both the non-rotating and rotating conditions; (4) to facilitate efficient simulation of detailed three-dimensional flow and heat transfer in stationary and rotating pin-fin channels under high Reynolds number and high rotation number conditions; (5) to investigate the effect of high rotation number, high Reynolds number, and high density ratio on the secondary flow field and the heat transfer characteristics in a rectangular duct with turbulators rotating at –135°, 90°, 135° and 150° orientations.

CHAPTER II

GOVERNING EQUATION AND NUMERICAL METHOD

A multi-block Reynolds-averaged Navier-Stokes (RANS) method was employed in conjunction with a near-wall second-moment turbulence closure. In the present method, the convective transport equations for momentum, energy, and turbulence quantities are solved in curvilinear, body-fitted coordinates using the finite-analytic method.

2.1 The Governing Equation and Chimera Method

For unsteady incompressible flow, the continuty equation and momentum equation were to be solved to get the velocity field,

$$\frac{\partial \rho}{\partial t} + (\rho U^m)_{,m} = 0 \tag{2-1}$$

$$\rho\left(\frac{\partial U^i}{\partial t} + U^m U^i_{,m} + R^{im}_{,m}\right) + 2\rho g^{il} e_{lmn} \Omega^m U^n + \rho g_{mn}\left(\Omega^i \Omega^m \xi^n - \Omega^m \Omega^n \xi^i\right) = -g^{im} p_{,m} + \mu\left(g^{mn} U^i_{,n}\right)_{,m} \tag{2-2}$$

The Reynolds stress tensor is the solution of the Reynolds stress transport equation :

$$\frac{\partial R^{ij}}{\partial t} + U^m R^{ij}_{,m} = P^{ij} + D^{ij}_u + D^{ij}_p + D^{ij}_v + \Phi^{ij} - \varepsilon^{ij} \tag{2-3}$$

where $P^{ij}, D^{ij}_u, D^{ij}_p, D^{ij}_v, \Phi^{ij}$ and ε^{ij} are the production term, diffusion by momentum fluctuation, diffusion by pressure fluctuation, viscous diffusion, pressure strain and dissipation term for Reynolds stress transport.

The flow is considered to be incompressible since the Mach number is quite low. However, the density in the centrifugal force terms is approximated by $\rho=\rho_o T_o/T$ to account for the density variations caused by the temperature differences. ρ_o and T_o are

the density and temperature at the inlet of the cooling channel. In general, the density is also a function of the rotating speed because the centrifugal force creates a pressure gradient along the duct. In the experiments of Lee et al.[31], the maximum pressure variation between the channel inlet and the exit is approximately 0.0113 atm for the highest rotation number of 0.28 considered in the present study. This gives a maximum density variation of only about 1.1% from the inlet to the exit of the duct at the highest rotation number. It is therefore reasonable to omit the density variation caused by the pressure gradients induced by the channel rotation.

The temperature T is obtained from the energy equation:

$$\overline{\rho} C_p \left[\frac{\partial T}{\partial t} + U^m T_{,m} + \left(\overline{u^m T'} \right)_{,m} \right] = g^{mn} \left(K T_{,n} \right)_{,m} + \frac{Dp}{Dt} + \Phi \qquad (2\text{-}4)$$

where T and T' are the mean and fluctuating temperature fields, Cp is the specific heat at constant pressure, K is the thermal conductivity.

The present method solves the mean flow and turbulence quantities in arbitrary combination of embedded, overlapped, or matched grids using a chimera domain decomposition approach. In this approach, the solution domain is first decomposed into a number of smaller blocks which facilitate efficient adaption of different block geometries, flow solvers and boundary conditions for calculations involving complex configurations and flow conditions. Within each computational block, the finite-analytic numerical method was employed to solve the unsteady RANS equations. The coupling between the pressure and velocity is accomplished using a hybrid PISO/SIMPLER algorithm. To ensure the proper conservation of mass and momentum between linking grid blocks, the grid interface conservation techniques of Hubbard and Chen[62] were

employed to eliminate unphysical mass source resulting from the interpolation errors between the chimera grid blocks.

2.2 Grid Generation

The grid was generated using an interactive grid generation code GRIDGEN. It was then divided into several overlapped chimera grid blocks to facilitate the implementation of the near-wall turbulence model and the specification of the boundary conditions. To provide adequate resolutions of the viscous sublayer and buffer layer adjacent to a solid surface, the minimum grid spacing for the Re = 10,000 cases is maintained at 10^{-3} of the hydraulic diameter which corresponds to a wall coordinate y^+ of the order of 0.1; the minimum grid spacing for the Re = 500,000 cases is maintained at 2×10^{-5} of the hydraulic diameter which corresponds to wall coordinate y^+ of the order of 0.1. In all calculations, the root-mean-square (rms) and maximum absolute errors for both the mean flow and turbulence quantities were monitored for each computational block to ensure complete convergence of the numerical solutions and a convergence criterion of 10^{-5} was used for the maximum rms error.

CHAPTER III

FLOW AND HEAT TRANSFER COMPUTATIONS IN ROTATING RECTANGULAR CHANNELS WITH V-SHAPED RIBS

In this chapter, we present calculation for a rotating/non-rotating single pass square channel with V-shape ribs as tested by Lee et al[31], using the near wall second-order Reynolds stress closure model.

3.1 Description of Problem

A schematic diagram of the geometry is shown in Figure 3.1. The channel has a rectangular cross section with a channel aspect ratio (AR) of 4:1. Of the four side walls, the two in the rotational direction are denoted as leading and trailing surfaces, while the other two are denoted as top and bottom surfaces. The channel hydraulic diameter, D_h, is 0.8in (2.03cm). The distance from the inlet of the channel to the axis of rotation is given by $R_r/D_h = 20.0$. The total length of the channel, L, equals to $22.5D_h$. The channel consists of an unheated smooth starting section ($L_1/D_h = 9.92$), a heated ribbed section ($L_2/D_h = 7.58$), and an unheated smooth exit section ($L_3/D_h = 5.00$). In the ribbed section, as shown in Figure 3.1, the leading and trailing surfaces are roughened by nine equally-spaced 45° V-shaped ribs with square cross section. The in-line V-shaped ribs are parallel and point upstream. The rib height-to-hydraulic diameter ratio (e/D_h) is 0.078. The rib pitch-to-height ratio (P/e) is 10. Three channel orientations ($\beta = 90°$, $\beta = -135°$, $\beta = 135°$) are studied, with $\beta = 90°$ corresponding to the mid-portion and $\beta =$

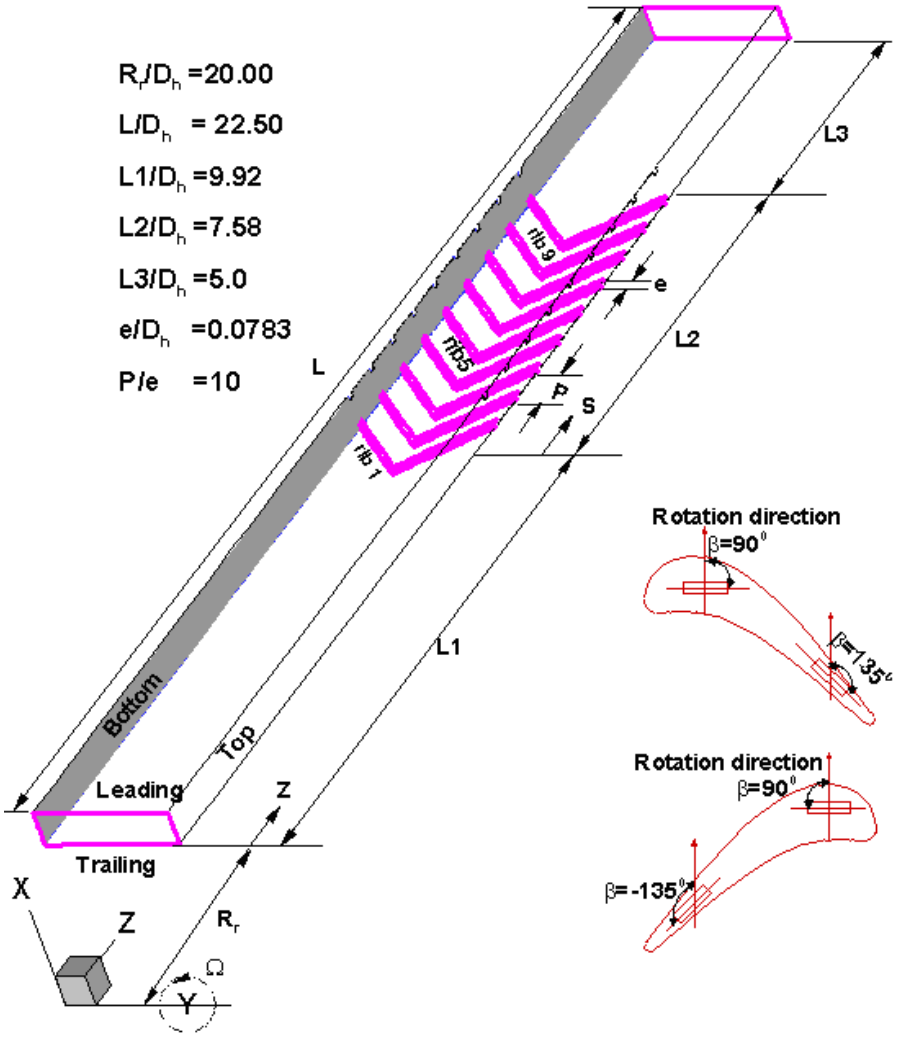

Fig. 3.1 Geometry and Conceptual View of Rotating Channel Orientation for Rectangular Duct (Ar = 4:1) with In-Line V-Shaped Ribs on Leading and Trailing Surfaces

−135° and β = 135° to the trailing edge region of a blade. A summary of all eight cases studied is given in Table 3.1.

Computational grid details

Figure 3.2(a) shows the computational grid around the ribs for the ribbed duct. The number of grid points in the streamwise direction is 402 (with 373 in the ribbed section), and the number of grid points in the cross-stream plane is 43×75 for *Re* = 10,000 cases. For the high Reynolds number (*Re* = 100,000 and 500,000) cases, the number of grid points in the cross-stream plane was increased from 33×75 to 43×85 while the number of grid points in the streamwise direction was maintained at 373 for the ribbed section. It is clearly seen from the grid refinement studies shown in Figures 3.2(b) and 3.2(c) that these grid distributions produced nearly grid-independent solutions for the *Re* =10,000 and 500,000 cases, respectively.

3.2 Velocity and Temperature Fields

As summarized in Table 3.1, computations were performed with Reynolds number (Re) ranging from 10^4 to 5×10^5, rotation number (Ro) from 0 to 0.28, inlet coolant-to wall density ratio ($\Delta\rho/\rho$) from 0.122 to 0.4, and channel orientations from −135° to 90° to 135°. The Nusselt numbers presented here are normalized with a smooth tube correlation by Dittus-Boelter for fully developed turbulent non-rotating tube flow:

$$Nu_o = 0.023\, Re^{0.8}\, Pr^{0.4} \tag{3-1}$$

Fig. 3.3 shows the velocity vector field and dimensionless temperature contour (θ) near the ribbed surface for the non-rotating case (case 1) listed in Table 3.1. As we can see from the figure, since the ribs are oriented at a 45° angle pointing upstream, the fluid

Table 3.1: Summary of cases studied for channel with v-shape ribs

Case #	**Ro**	$\Delta\rho/\rho$	β	**Re**
1	0.00	0.122	-	10,000
2	0.14	0.122	90°	10,000
3	0.14	0.122	135°	10,000
4	0.14	0.122	–135°	10,000
5	0.00	0.122	-	100,000
6	0.00	0.122	-	500,000
7	0.28	0.200	135°	500,000
8	0.28	0.400	135°	500,000

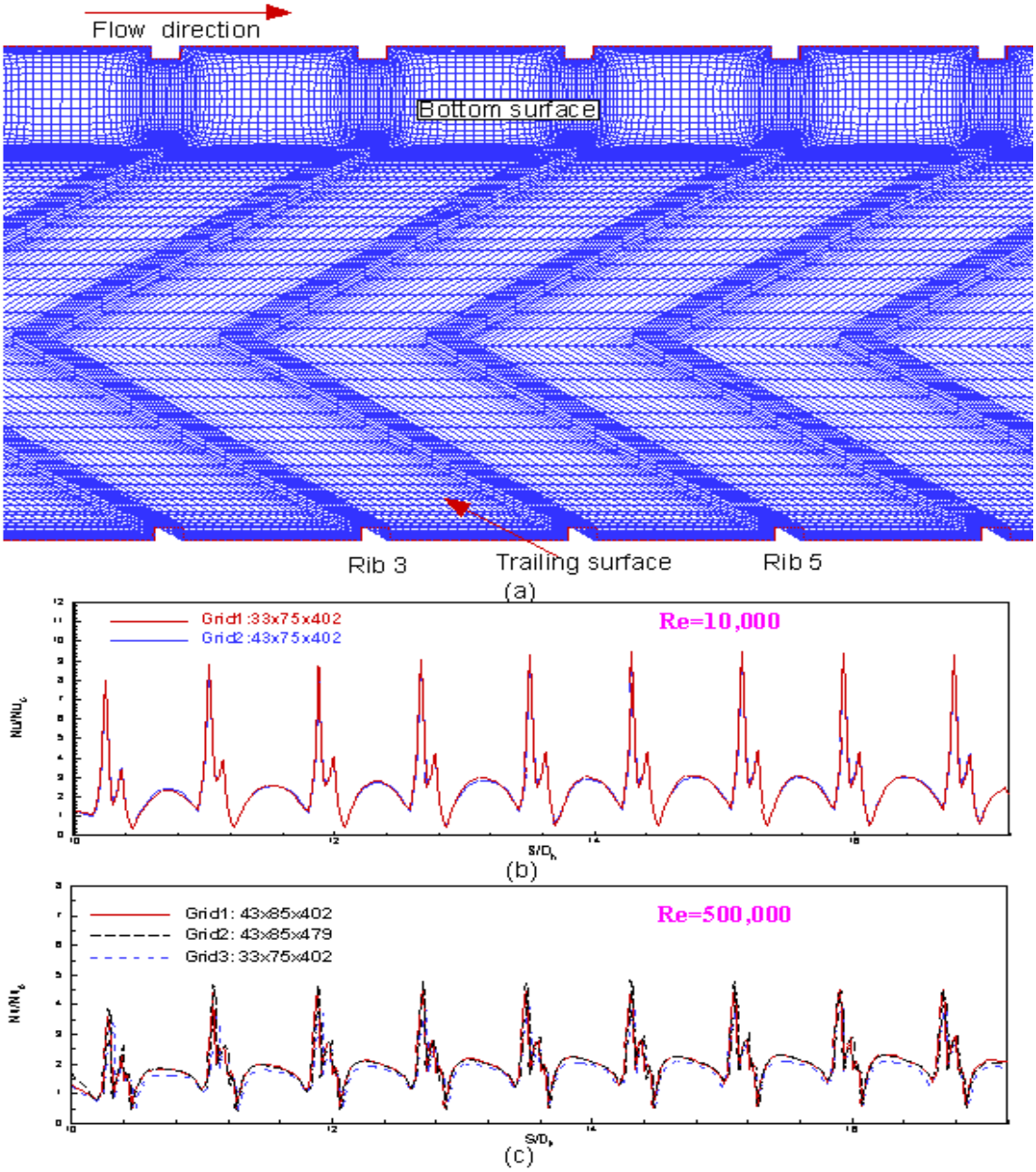

Fig. 3.2 (a) Numerical Grid, (b) Grid Refinement Study for Re = 10,000, (c) Grid Refinement Study for Re = 500,000

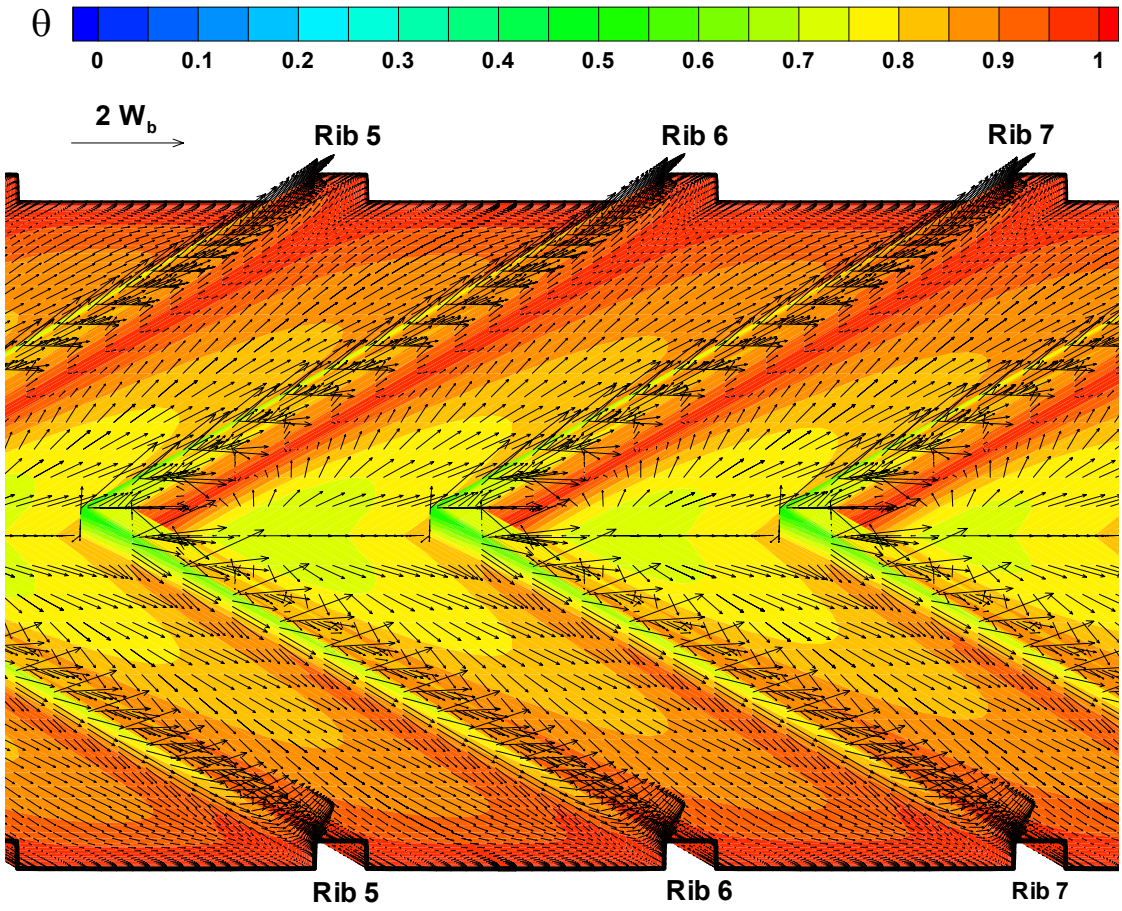

Fig. 3.3 Velocity and Dimensionless Temperature [$\theta = (T-T_i)/(T_w-T_i)$] Contours Close to the Rib Surface for Non-Rotating Duct (Re = 10,000, Ro =0.0, $\Delta\rho/\rho$ = 0.122)

in the center of the channel reaches the ribs first and moves along the ribbed surfaces toward the side walls, i.e., the top and bottom surfaces. It is also observed that the ribs produce repeated flow separations and reattachment in the streamwise direction. The cooler fluid impingement induced by the V-shaped ribs leaves behind each rib a V-shaped temperature contour. This dimensionless temperature contour is closely related to the streamwise velocity and secondary flow patterns induced by the V-shaped ribs. The temperature is high immediately downstream of each rib due to flow separations behind the ribs. In the middle section between the ribs, however, the temperature is relatively low due to the impingement of cooler fluids in the flow reattachment zone. As the coolant flow near the ribbed surface is directed towards the side walls by the ribs, the value level of the V-shaped temperature contour increases, i.e., the coolant gets hotter, in the direction of the inclined ribs.

Fig. 3.4 shows the secondary flow vectors and dimensionless temperature contours both on top of and between several selected V-shaped ribs for Case 1. The secondary flow vectors show that the V-shaped ribs produce very strong tangential velocities which carry the cooler fluid from the center of the channel towards the side walls. The flow on top of the ribs is nearly parallel to the ribbed surface and its vertical velocity components are rather weak. The vertical velocity components of the flow behind ribs are significantly stronger due to flow reattachment (impingement) between ribs. Also observed from Fig. 3.4 is the early stage development of two pairs of counter-rotating vortices on top of each rib, which grow into four full symmetric counter-rotating vortices in the midsection between ribs.

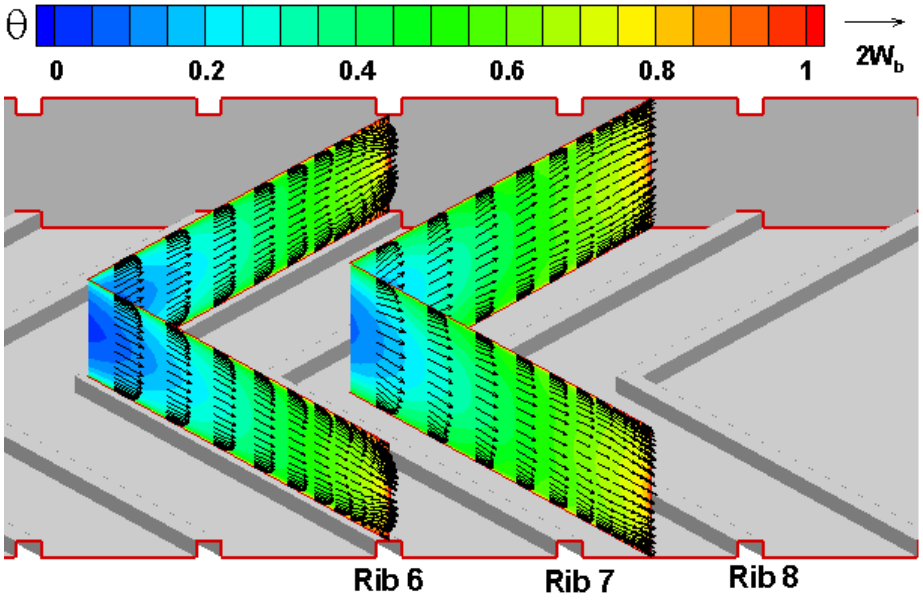

(a) Tangential velocity vectors

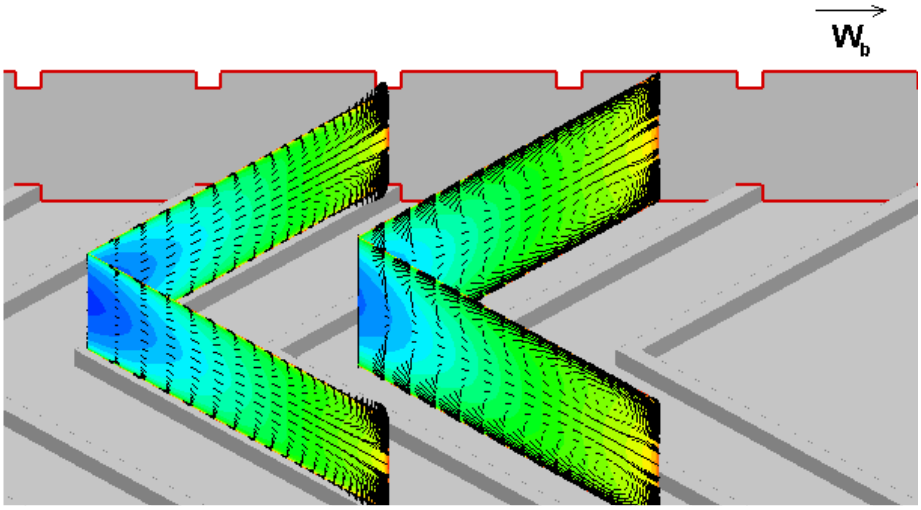

Fig. 3.4 Tangential Velocity and Secondary Flow Vectors and Dimensionless Temperature [$\Theta = (T- T_i)/(T_w-T_i)$] Contours on and between Ribs for Non-Rotating Duct

Figure 3.5 gives the calculated dimensionless temperature contours near the ribbed surface and at selected cross sections for the non-rotating case (case 1). As it is shown on the symmetric plane along the channel centerline, coolant temperature increases in the streamwise direction as the coolant flows down the channel and is heated by the channel walls. The temperature contours near the ribbed surfaces show small areas of low temperature on the front edge of the ribs, indicating coolant impingement on the ribs. High temperatures right behind ribs indicate flow separation. Relatively lower temperatures between ribs indicate coolant impingement and reattachment. Temperature contours between two ribs expand in the 45° angle from the center plane, indicating that the coolant near the ribbed surface is flowing along the 45° inclined ribs from the center of the channel to the side walls. The temperature contours on the cross sections cut in the direction of the inclined ribs show that the temperature is relatively low near the center of the channel, but increases gradually towards the side walls in the direction of the V-shaped ribs as the coolant flows along the inclined ribs. Similar temperature contour patterns are observed between and above ribs. However, as coolant flows down the channel, the temperature gradient in the spanwise direction is gradually weakened due to the continuous heating of the coolant by the wall.

Figure 3.6 shows velocity vectors and temperature contours on two selected planes in a rotating duct (Case 2). These two planes are parallel to the mainstream direction and perpendicular to the leading and trailing surfaces. Plane 1 spans over ribs 7 and 8, while Plane 2 spans over ribs 4 and 5. The distance between Plane 1 and the bottom

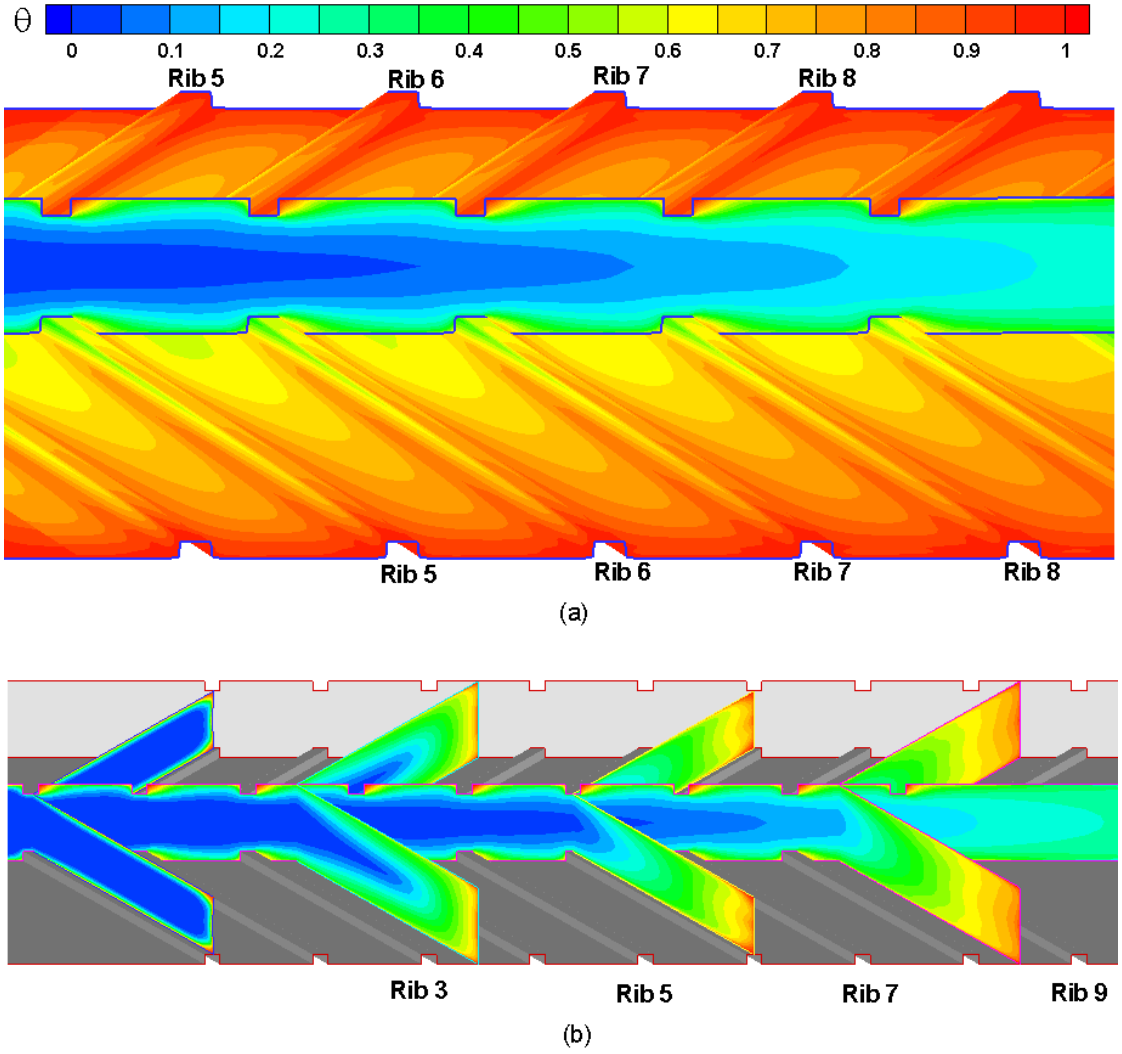

Fig. 3.5 Temperature [$\theta = (T-T_i)/(T_w-T_i)$] Contours for Non-Rotating Ducts: (a) Close to the Rib Surface and along the Center Plane of Symmetry; (b) Selected Cross Sections

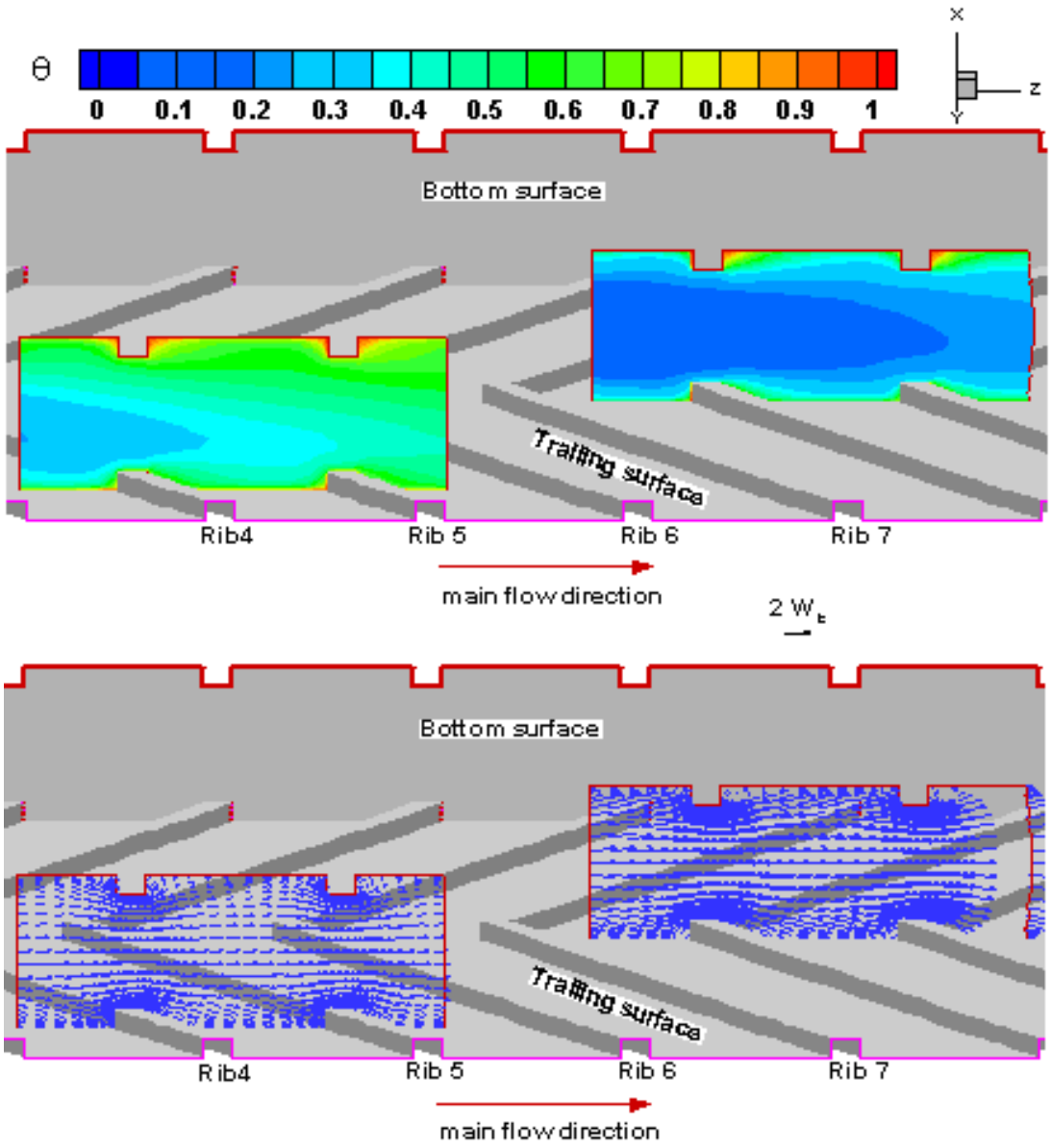

Fig. 3.6 Flow along Mainstream Direction and Dimensionless Temperature [$\theta = (T-T_i)/(T_w-T_i)$] Contours for Rotating Duct ($Re = 10^4$, $\Delta\rho/\rho = 0.122$, $Ro = 0.14$, $\beta = 90°$)

surface is $1.25D_h$ and that between Plane 2 and the top surface is $0.31D_h$. Velocity vectors in Planes 1 and 2 indicate that there is flow separation right behind each rib and flow reattachment (impingement) happens in the middle section between every two neighboring ribs. Due to duct rotation and Coriolis force effect (relatively small rotation effect at $Ro = 0.14$), velocity vectors in Plane 1 are slightly distorted towards the trailing surface as compared to the non-rotating Case 1. This flow distortion is even more obvious in Plane 2 since it is farther away from the center of the channel. Temperature contours on both planes are affected accordingly. The coolant flow is pushed towards the trailing surface by the Coriolis force, causing the temperature on the leading side to be higher than that on the trailing side. It is observed from Figure 3.6 that the low-temperature core of the coolant flow shrinks significantly in the spanwise direction as the fluid flows down the duct. Although Plane 1 spans over two ribs downstream of Plane 2, the temperatures of Plane 1 are much lower than those of Plane 2 because Plane 2 is much closer to the side wall.

In order to provide a more detailed understanding on the heat transfer enhancement due to V-shaped ribs, it is worthwhile to examine the secondary flow vectors and temperature contours along the ribbed channel in the manner shown in Figures 3.7, 3.8, and 3.9. Figures 3.7, 3.8, and 3.9 provide the secondary flow and dimensionless temperature contours at selected cross sections for Cases 1, 2, and 3. The channel orientation is 90° in Case 2 and 135° in Case 3. Both Cases 2 and 3 have a rotating number of 0.14.

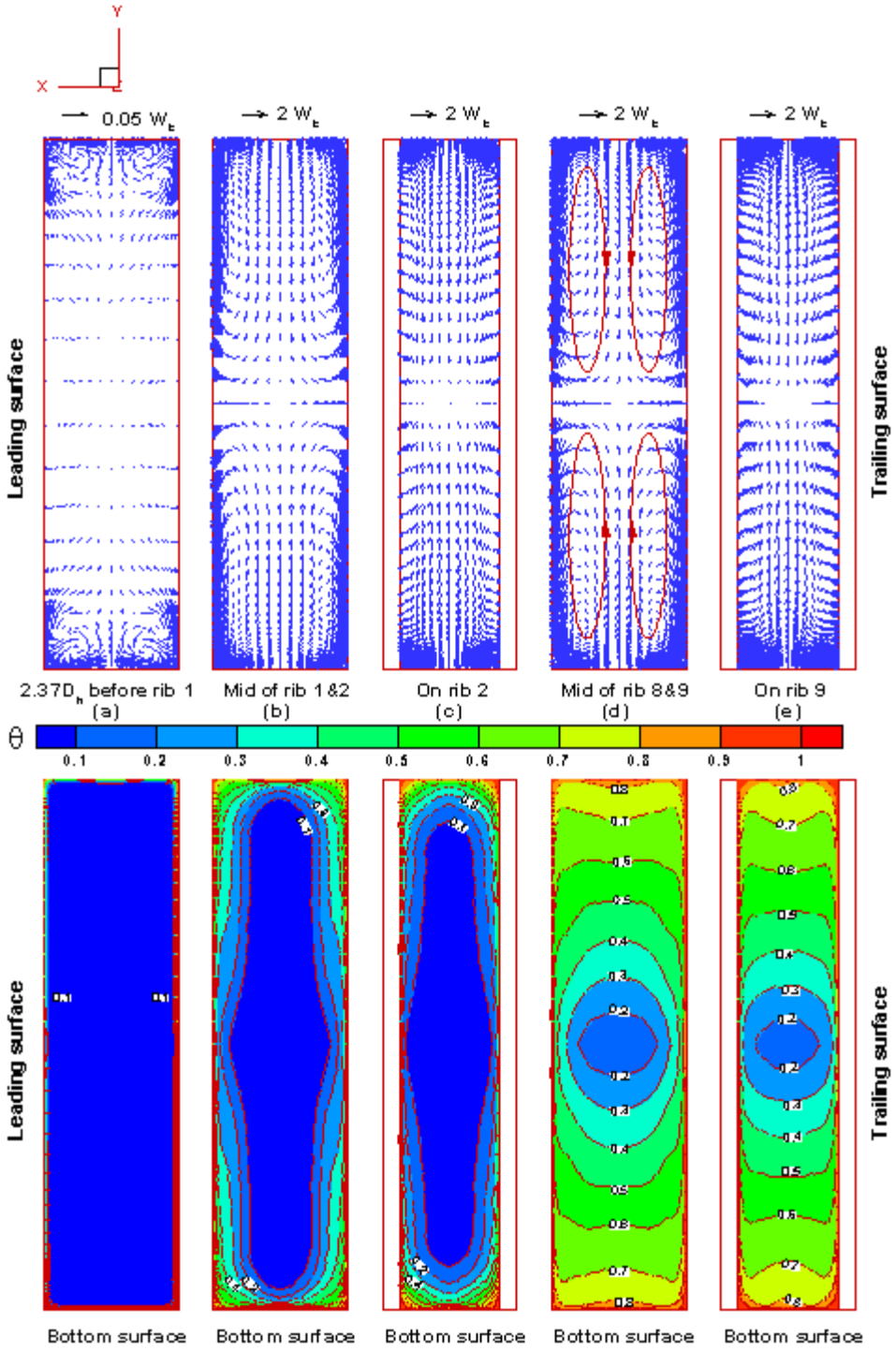

Fig. 3.7 Secondary Flow and Dimensionless Temperature [$\theta = (T-T_i)/(T_w-T_i)$]

Contours for Non-Rotating Duct (Re = 10,000, Ro = 0.0, $\Delta\rho/\rho = 0.122$)

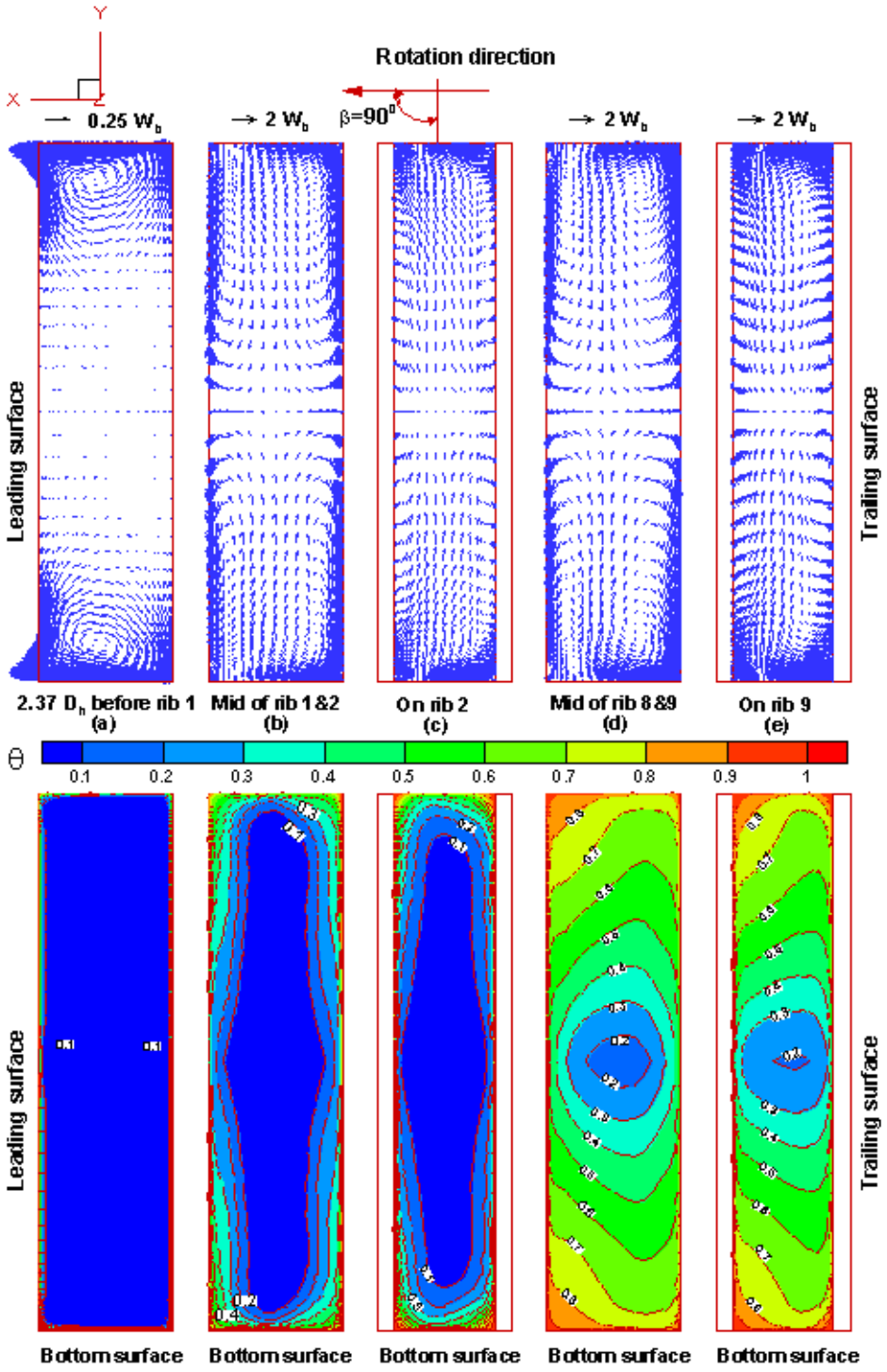

Fig. 3.8 Secondary Flow and Dimensionless Temperature [$\theta = (T-T_i)/(T_w-T_i)$]

Contours for Rotating Duct (Re = 10,000, $\Delta\rho/\rho = 0.122$, Ro = 0.14, $\beta = 90°$)

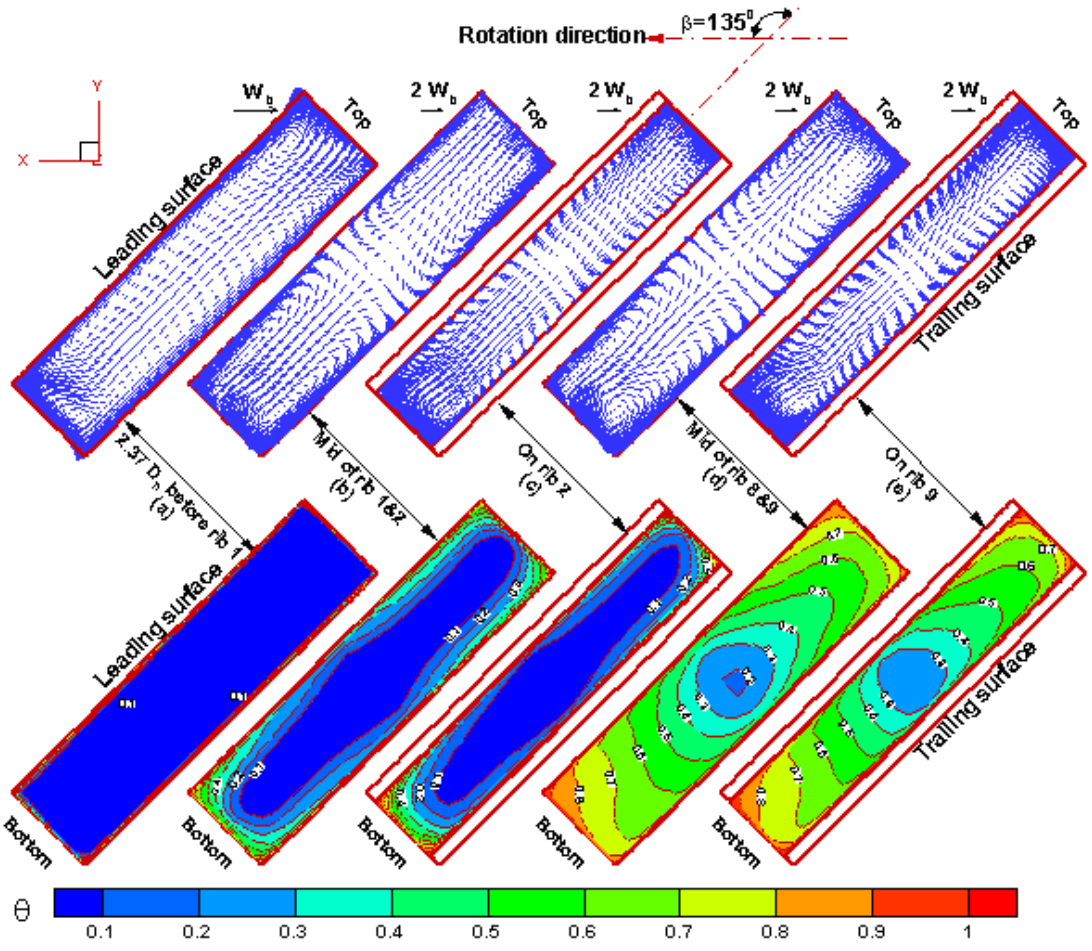

Fig. 3.9 Secondary Flow and Dimensionless Temperature [$\theta = (T-T_i)(/T_w-T_i)$] Contours for Rotating Duct (Re = 10,000, $\Delta\rho/\rho = 0.122$, Ro = 0.14, $\beta = 135°$)

As shown in Figure 3.7, in the smooth section before the first rib, four pairs of corner vortices are generated as a result of the Reynolds stress anisotropy. As the flow approaches the V-shaped ribs, these corner vortices are overpowered by two new pairs of V-shaped rib-induced vortices. The strength of these four rib-induced vortices increases considerably in the middle section between two ribs. The size of these four counter-rotating vortices oscillates along the streamwise direction from the largest in the middle of each inter-rib distance to the smallest on the rib tops. This pattern of oscillation repeats itself till the end of the last rib. The effect of this secondary flow on the temperature field is that the cooler fluid in the core region is convected along the ribbed surface to the top and bottom surfaces, i.e., the side walls. This results in steep temperature gradients and high heat transfer coefficients on the ribbed surfaces as seen in the corresponding temperature contours.

Figure 3.8 shows that the Coriolis force produces in front of the first rib a cross-stream two-vortex flow structure. The two vortexes are symmetric along the x-axis. As the flow approaches the rib, the secondary flow induced by the Coriolis force starts to distort the secondary flow induced by the V-shaped rib. A comparison between Figure 3.8 and Figure 3.7 shows that: (1) The magnitude of the secondary flow induced by the Coriolis force is weaker than that induced by the V-shaped rib; (2) Due to the Coriolis force effect, the size and strength of the two vortices adjacent to the trailing surface increases while that of the other two vortices adjacent to the leading surface decreases; (3) Vortices on top of ribs shrink in size and get significantly distorted by the Coriolis force only in the region near the top and bottom surfaces. The general effect of the

Coriolis force induced secondary flow is to distort the rib-induced vortices. Consequently, the temperature contours are shifted toward the trailing surface as shown in the corresponding temperature contour plot in Figure 3.8. The heat transfer on all four side surfaces is affected accordingly: divided by plane *yz*, regions near the trailing side, including the trailing surface and a portion of the top and bottom surfaces adjacent to the trailing surface, have steeper temperature gradient and thus higher heat transfer than the non-rotating case; regions near the leading side, including the leading surface and a portion of the top and bottom surfaces adjacent to the leading surface, have gentler temperature gradient and thus lower heat transfer than the non-rotating case.

Figure 3.9 shows the cross-stream velocity vectors and temperature contours for the $\beta = 135°$ case at the same planes as in Cases 1 and 2. In the smooth section before the first rib, the Coriolis force produces a distorted cross-stream two-vortex flow structure. The left corner of the vortex near the top surface stretches along the leading surface all the way to the bottom surface, while the vortex at the bottom shrink into the corner between the trailing surface and the bottom surface. This Coriolis force induced secondary flow pushes the cold fluid away from the corner between the leading and bottom surfaces towards the corner between the trailing and top surfaces. A comparison between Figure 3.9 and Figure 3.7 shows that: (1) Due to the Coriolis force effect, the size and strength of the rib-induced vortex adjacent to the top-trailing corner increases and this vortex predominates the top half of the cross section; the size and strength of the rib-induced vortex adjacent to the bottom-trailing corner increase and dominate the triangular region in the bottom-trailing corner of the cross section; (2) Vortices on top of

ribs shrink in size and are significantly distorted by the Coriolis force only in the region near the top and bottom surfaces; (3) A net upward fluid motion from the bottom to the top is observed in the core region of the channel. The net effect of the secondary flow field is to push the cooler fluid towards the top surface, as illustrated by the temperature contours shown in Figure 3.9. Compared to Cases 1 and 2, Case 3 has steeper temperature gradient on both the top and trailing surfaces and thus higher heat transfer coefficients in this area.

3.3 Heat Transfer Coefficient Distribution

Effect of rotation and channel orientation on heat transfer coefficient distribution

Figure 3.10 gives the local Nusselt number ratio contours on the ribbed leading and trailing surfaces for Cases 1, 2, 3, and 4, respectively. The non-rotating case in Figures 3.10(1a) and (1b) is used as a baseline for comparison and discussion. The entrance and exit regions are cut to focus on the ribbed heated section. Figures 3.10(1a) and (1b) show that the Nusselt number ratio distribution is the same on both the leading and trailing surfaces for the non-rotating case. Highest Nusselt number ratios are located near the tip of the V-shaped ribs, while lowest Nusselt number ratios are located right before and after the ribs as well as near the top and bottom surfaces. The Nusselt number ratios between any two ribs are higher in the central area and decrease along the inclined ribs. The high-Nusselt-number region behind the ribs grows from a small heart shape behind the first several ribs to a V shape with two long wings as the coolant flows along in the duct and the rib-induced secondary flow develops.

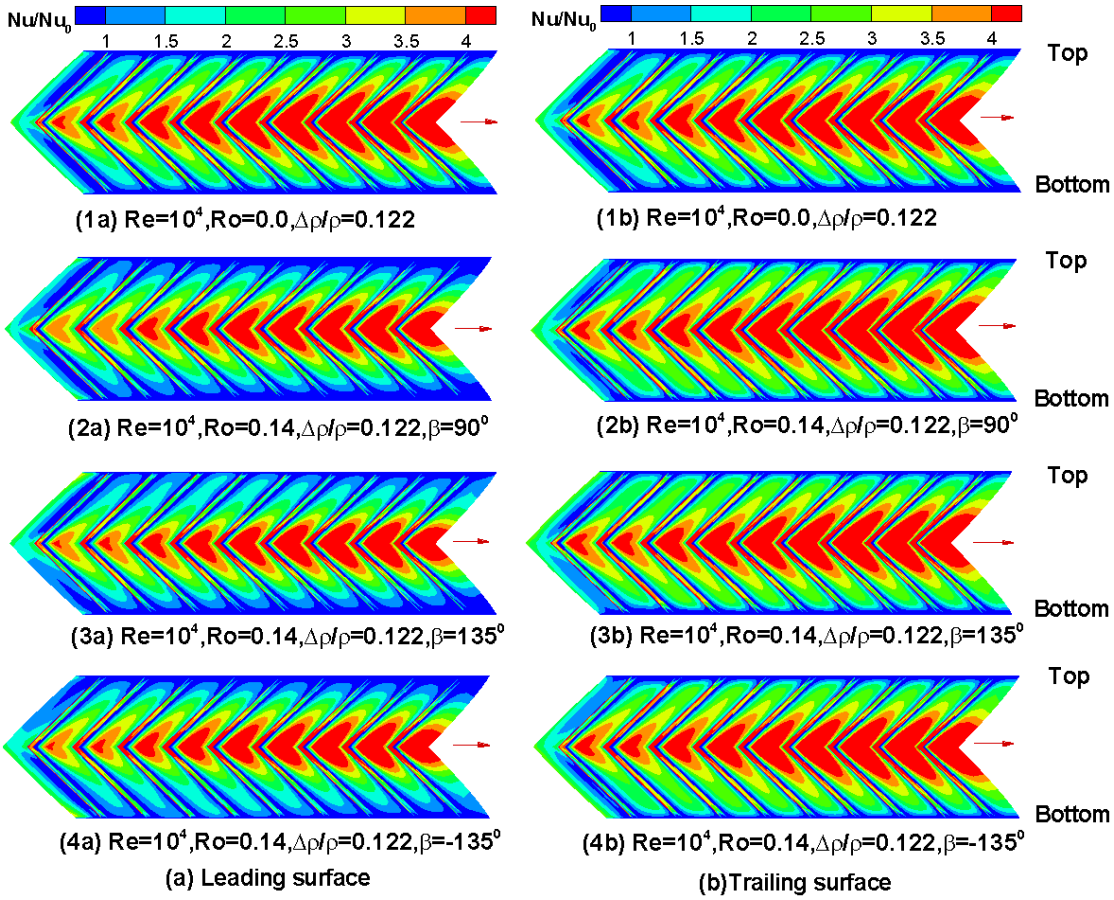

Fig. 3.10 Nusselt Number Ratio Contours on (a) Leading and (b) Trailing Surface for Lower Reynolds Number (Re = 10,000) Cases

In the three rotating cases shown in Figures 3.10 (2a) to 3.10 (4b), the rotation number is 0.14 while the density ratio is kept at 0.122. Overall, compared to the non-rotating case, it is quite clear that channel rotation leads to a significant decrease in the Nusselt number ratios on the leading surface. Rotation pushes the cooler fluid away from the leading surface. Therefore, unlike what happens in the non-rotating case, the heart-shaped high-Nusselt-number regions behind the first several ribs are somewhat restrained from developing into V-shaped high-Nusselt-number regions. On the other hand, the Nusselt number ratios on the trailing surface increase as a result of channel rotation. The regions of high Nusselt number ratio on the trailing surface spread toward the side walls as compared to the non-rotating case. This is due to the rotation-induced secondary flow that pushes the cooler fluid towards the trailing surface and the side walls adjacent to the trailing surface.

The effect of orientation on Nusselt number ratios can be seen by comparing the rotating cases shown in Figures 3.10(2) to 3.10(4). Rotation with a channel orientation of 90°, as shown in Figures 3.10(2), decrease the Nusselt number ratios on the leading surface and increase the Nusselt number ratios on the trailing surface, and the Nusselt number ratio distributions on both surfaces are symmetric along the centerline of the duct. However, rotation with a channel orientation of 135°, as shown in Figures 3.10(3), pushes the cooler fluid away from the corner between the leading surface and the bottom surface towards the corner between the trailing surface and the top surface. Therefore, the high-Nusselt-number regions, especially the four regions between the first five ribs, on both the leading and trailing surfaces are asymmetric and shifted towards the side

walls. Similarly, rotation with a channel orientation of -135°, as shown in Figures 3.10(4), pushes the cooler fluid away from the corner between the trailing surface and the top surface towards the corner between the leading surface and the bottom surface. Thus, the high-Nusselt-number regions on both the leading and trailing surfaces are asymmetric and shifted towards the side walls.

Figure 3.11 presents the spanwise Nusselt number ratios for the non-rotating Case 1, and the rotating Case 4 ($\beta = -135°$). In addition, regionally averaged Nusselt number ratios are also presented in Figure 3.11 to facilitate a direct comparison with the experimental data of Lee et al.[31] for the same test conditions. It is clearly seen that the numerical predictions for both the non-rotating and rotating cases are in very good agreement with the corresponding measurements. For the non-rotating case, the average discrepancy between the predicted and measured Nusselt number ratios is only about 3.0%. Similar level of agreement was observed for the rotating case with an average discrepancy of 4.2%. These results clearly illustrated the capability of the present second-moment RANS method for accurate prediction of the flow and heat transfer characteristics induced by the V-shaped ribs.

Figure 3.12 compares the numerically predicted spanwise-averaged Nusselt number ratios of Case 2 ($\beta = 90°$) and Case 3 ($\beta = 135°$) with those of the non-rotating case. In all cases shown in Figure 3.11 and Figure 3.12, the spanwise-averaged Nusselt number distributions on both the leading and trailing surfaces show periodic spikes. The higher spikes which occur on the rib tops are caused by flow impingement on the ribs;

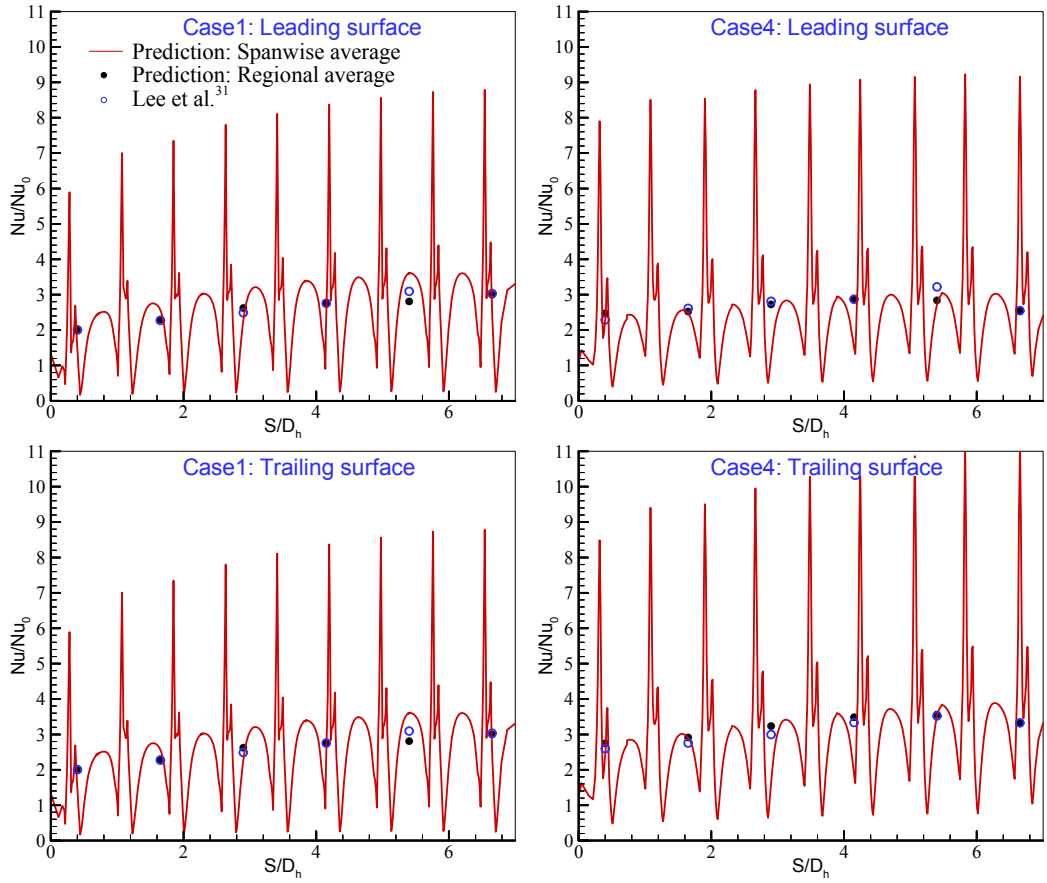

Fig. 3.11 Comparison between Calculated and Measured Nusselt Number Ratios for Non-Rotating (Case 1) and Rotating (Case 4: Ro=0.14, β = –135°) Ribbed Ducts

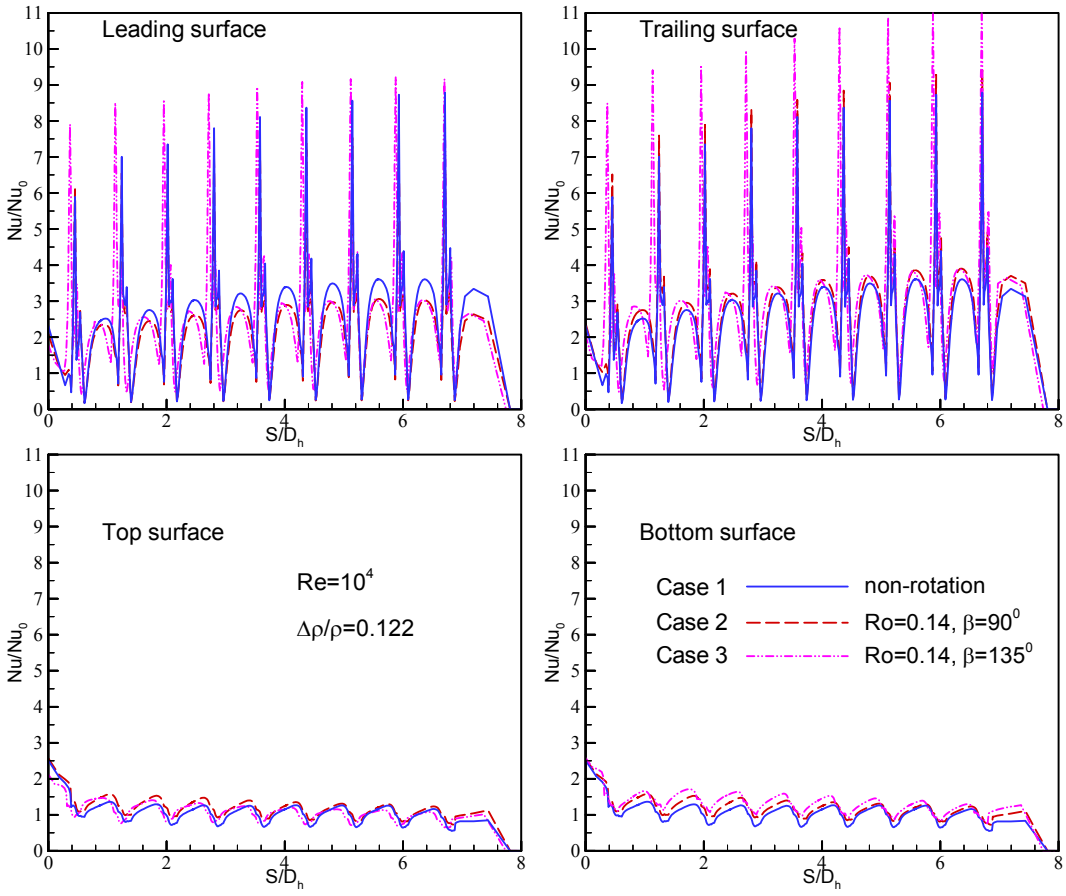

Fig. 3.12 Effect of Rotation and Channel Orientation on Spanwise-Averaged Nusselt Number Ratios for Lower Reynolds Number (Re = 10,000) Cases

the lower and rounded spikes are caused by flow reattachment between ribs. The Nusselt number ratios reach a peak value around the eighth rib, indicating a continuously growing rib-induced secondary flow along the duct.

As noted earlier, channel rotation leads to an increase in Nusselt number on the trailing surface and a decrease in Nusselt number on the leading surface. The Nusselt number ratios also increase on the top and bottom surfaces as a result of the secondary flow impingement on the side walls. The change of channel orientation from $\beta = 90°$ to $\beta = 135°$ leads to an increase of the spanwise-averaged Nusselt number ratios on the bottom surface and a minor decrease of the spanwise-averaged Nusselt number ratios on the top surface, but it has negligible effects on the magnitude of the spanwise-averaged Nusselt number ratios on both the leading and trailing surfaces. For the $\beta = 135°$ case, the coolant was pushed towards the corner between the trailing and top surfaces and thus slightly shifts those high Nusselt number regions towards the upstream direction. This leads to a forward displacement of the spanwise-averaged Nusselt number ratio curves on all four walls. However, the overall rotation effects are quite small at $Ro = 0.14$ when compared to the heat transfer enhancement caused by the rib-induced flows.

Effect of high Reynolds number on heat transfer coefficient distribution

Due to the limitation of experimental facility, Lee et al.[31] did not investigate the high Reynolds number ($Re \sim 500{,}000$) and high density ratio ($\Delta\rho/\rho \sim 0.4$) conditions that could be applied for the blade coolant passage designs of the large power-generation turbines. After successful validations with the experimental data of Lee et al.[31] at low Reynolds number and low density ratio conditions, it is desirable to extend the present

second-moment RANS method for turbine blade cooling applications involving high Reynolds number and high density ratio and high rotation number conditions listed in Table 3.1 (i.e., Cases 5 – 8). In these calculations, the Reynolds number was increased from10^4 to 10^5 and 5×10^5, the rotation number was doubled from 0.14 to 0.28, and the density ratio was increased from 0.122 to 0.2 and 0.4. This enables us to evaluate the heat transfer enhancement in blade coolant passages under more realistic turbine operating conditions.

Figure 3.13 shows the detailed Nusselt number ratio contours of the ribbed leading and trailing surfaces for high *Re* cases. The entrance and exit regions are cut to focus on the ribbed heated region. For the non-rotating cases shown in (5) and (6), the highest Nusselt number ratios are located near the tip of the V-shaped ribs, and the lower Nusselt number ratios are obtained right before and after the ribs. Between any two ribs, the Nusselt number ratios near the center are the highest and decrease along the direction of the inclined ribs. When the Reynolds number was increased from 10^4 (Case 1) to 10^5 (Case 5) and 5×10^5 (Case 6), the Nusselt number ratio in the middle section of the channel decreases significantly, indicating that the heat transfer enhancement caused by the rib-induced secondary flow is reduced when the thermal boundary layer becomes thinner at high Reynolds numbers.

Figure 3.14 gives the spanwise-averaged Nusselt number ratios for the non-rotating duct at three different Reynolds numbers of 10^4, 10^5, and 5×10^5. In general, the Nusselt number ratios on the leading and trailing surfaces decrease as the Reynolds number increases. On the other hand, the Nusselt number ratios on the top and bottom surfaces

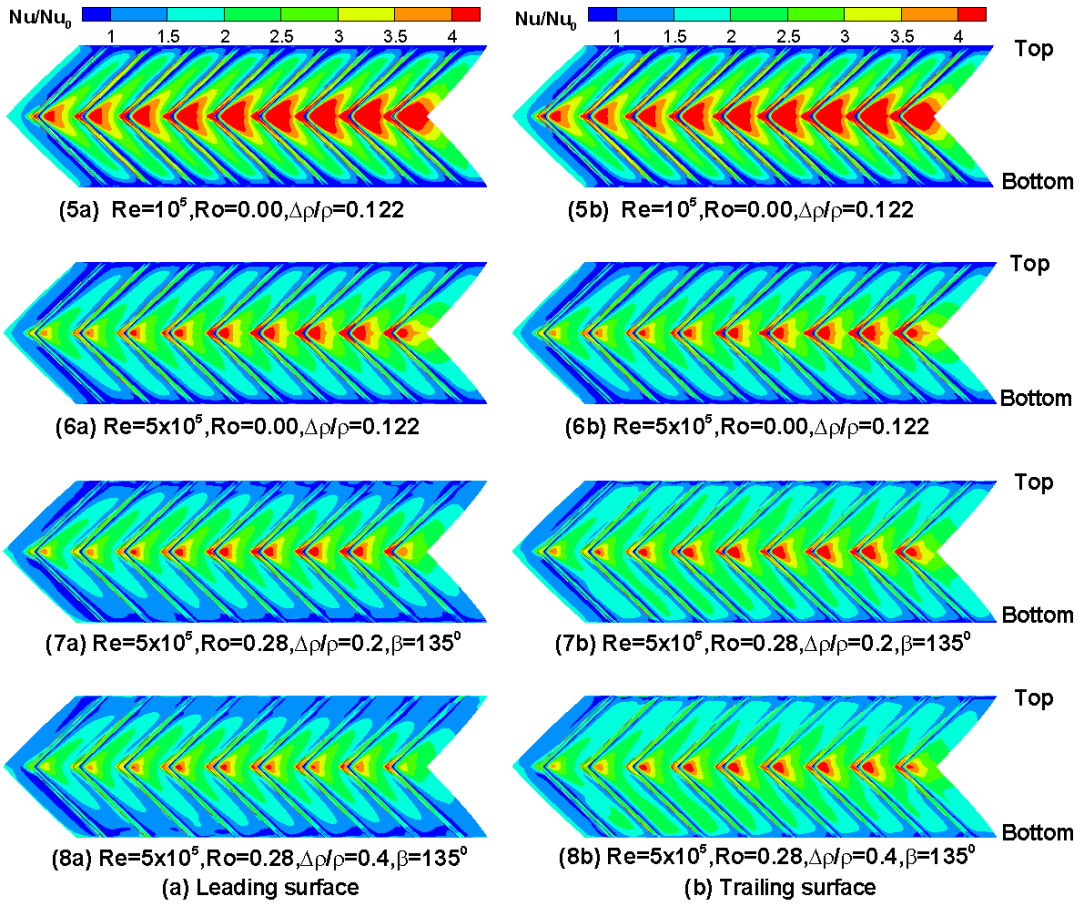

Fig. 3.13 Nusselt Number Ratio Contours on (a) Leading and (b) Trailing Surface for Higher Reynolds Number (Re = 500,000) Cases

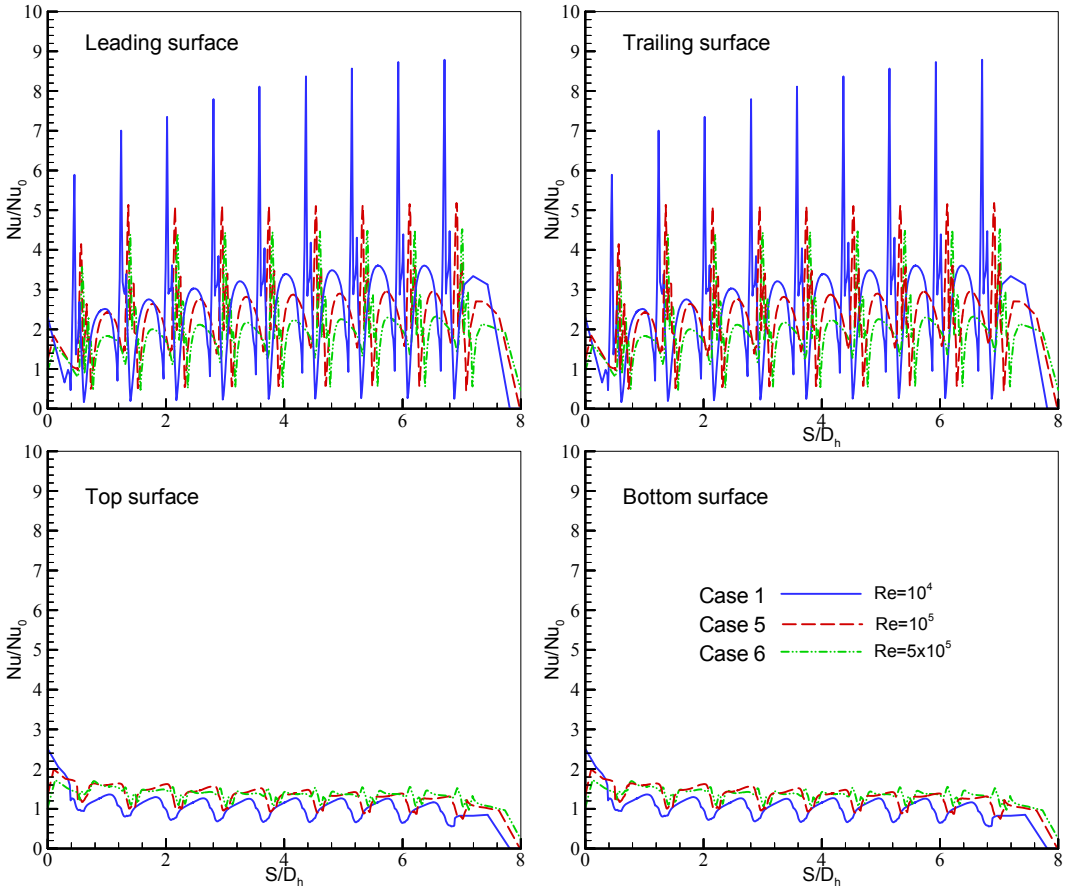

Fig. 3.14 Effect of Reynolds Number on Spanwised-Averaged Nusselt Number Ratios for Non-Rotating Duct (Ro = 0.0, $\Delta\rho/\rho$ = 0.122)

increase with the Reynolds number. However, it should be noted that the actual Nusselt numbers are much higher for the high Re cases because the Nu_o for smooth duct (proportional to $Re^{0.8}$) is already very high in these cases due to high turbulence and high temperature gradient inside the boundary layer.

Effect of rotation and density ratio on heat transfer coefficient distribution

A comparison between Figures 3.13(6), the high *Re* non-rotating case, and 3.13(7), the high *Re* and high *Ro* case, shows that channel rotation leads to a significant decrease in Nusselt number ratio on the leading surface. On the other hand, the Nusselt number ratios on the trailing surface increase slightly due to the effect of channel rotation. It is also noted that the high Nusselt number ratio regions on the trailing surface spread toward the side walls. This is due to the rotation-induced secondary flow that pushes the cooler fluid towards the trailing surface and side walls. In cases shown in Figures 3.13(7) and 3.13(8), the density ratio is increased from 0.20 to 0.40, while the Reynolds number and rotation number are kept the same. It is quite clear that an increase in density ratio leads the Nusselt number ratios to further decrease on the leading surface and slightly decrease on the trailing surface. This is because an increased density ratio intensifies the effect of the rotation-induced Coriolis force.

Figure 3.15 compares the spanwise-averaged Nusselt number ratios of Case 6 with those of Cases 7 and 8. Case 7 has a density ratio of 0.2 and Case 8 has a density ratio of 0.4. As noted earlier, channel rotation leads to an increase in Nusselt number on the trailing surface and a decrease in Nusselt number on the leading surface. At a rotation number of 0.28, an increase in density ratio (from $\Delta\rho/\rho = 0.2$ to $\Delta\rho/\rho = 0.4$) reduces the

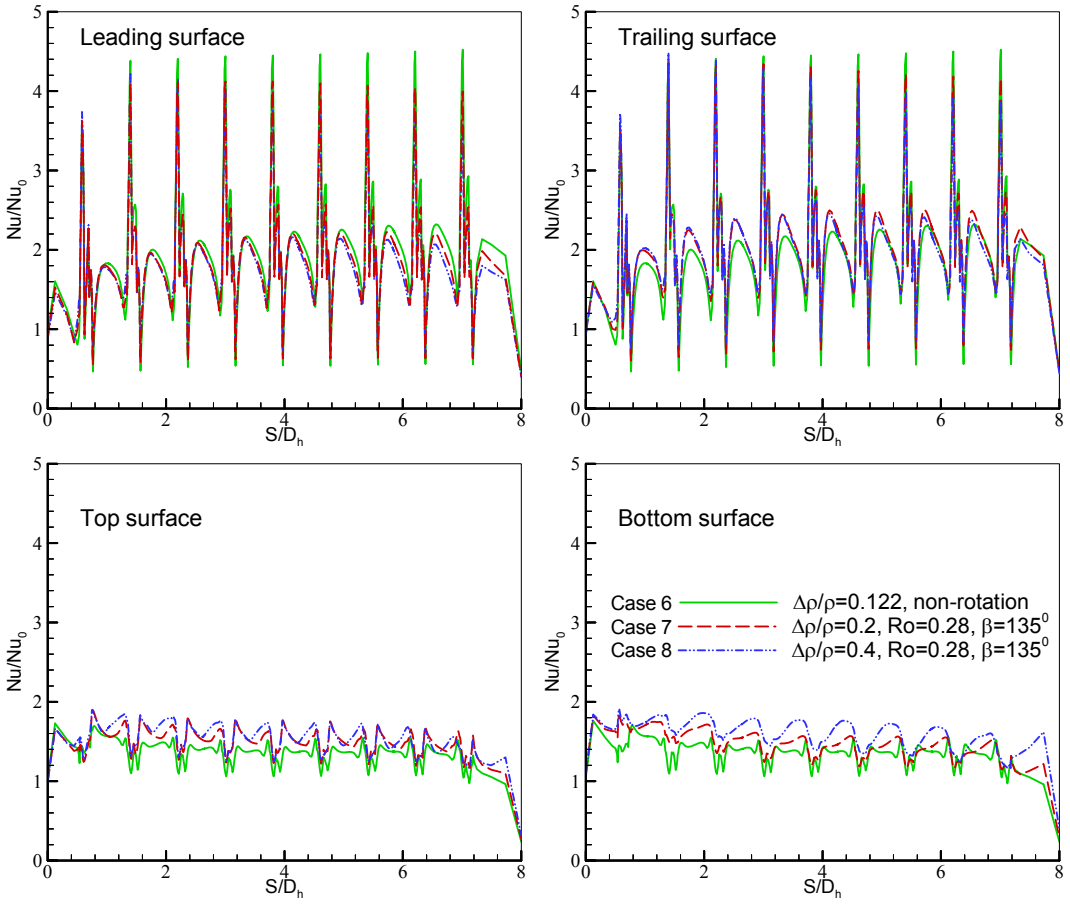

Fig. 3.15 Effect of Rotation and Density Ratio on Spanwise-averaged Nusselt Number Ratios for High Reynolds Number (Re = 500,000) Cases

heat transfer coefficients on both the leading and trailing surfaces. In general, a change in density ratio does not have an obvious effect on the Nusselt number ratios on the leading and trailing surfaces until the flow reaches about halfway of the heated channel section. The combination of rotation and higher density ratio has a net effect of reducing the Nusselt number ratios on the leading surface. The effects of rotation and higher density ratio tend to offset each other on the trailing surface, but the total effect is still to increase the Nusselt number ratios on the trailing surface. As the density ratio increases from 0.2 to 0.4, significant enhancements in Nusselt number ratios are observed on the top and bottom surfaces.

CHAPTER IV

FLOW AND HEAT TRANSFER COMPUTATIONS IN ROTATING RECTANGULAR CHANNELS (AR=4:1) WITH PIN-FINS

In this chapter, we perform calculations for rotating/non-rotating two pass rectangular channels (AR=4:1) with pin-fins as tested by Wright et al.[48] using the near wall second-order Reynolds stress closure model.

4.1 Description of the Problem

A schematic diagram of the pin-fin configuration used in the present study is shown in Fig. 4.1. This test section shown in Fig. 4.1(a) has 12 rows of pins in the flow direction and is identical to that used by Wright et al. in their experimental investigations. For the non-rotating case, the flow is symmetric with respect to both the y and z coordinates at each longitudinal cross-section. Therefore, it is possible to simulate only one-quarter of the channel cross-section but include all 12 rows of pin-fins. Under rotating conditions, however, the flow is no longer symmetric due to the presence of centrifugal and Coriolis forces induced by the channel rotation. Consequently, it will be necessary to include the full channel cross-section for the rotating pin-fin channels. Due to the limitation in available computer resources, the present rotating channel flow simulations were performed for the full channel cross-section but with only 6 rows of pin-fins, as shown in Fig. 4.1(b). The channel has a rectangular cross section with a channel aspect ratio (*AR*) of 4:1. Of the four sidewalls, the two in the rotational direction are denoted as the leading and trailing surfaces, while

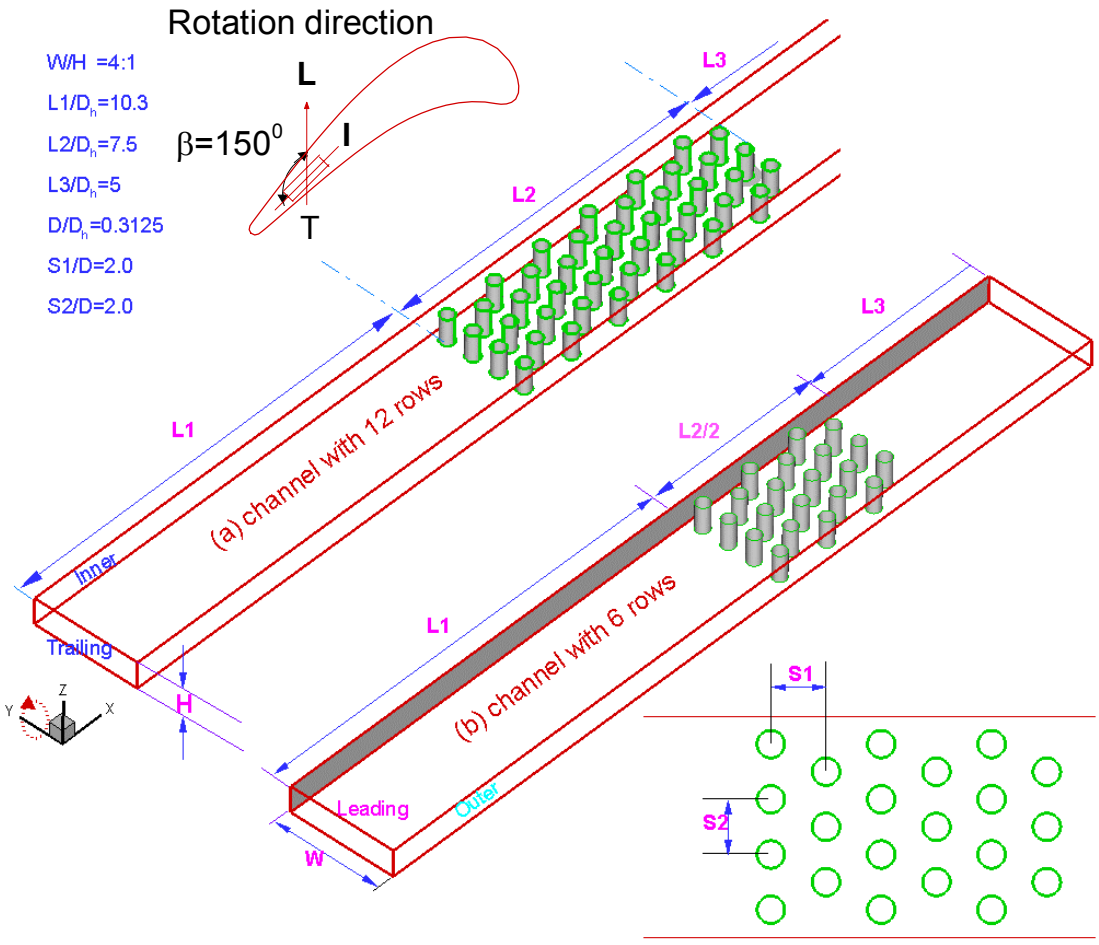

Fig. 4.1 Geometry and Conceptual View of the Rotating Channel for the Rectangular Duct (Ar=4:1) with Pin-Fins

the other two are denoted as the inner and outer surfaces. The channel hydraulic diameter, D_h, is 0.8in (2.03cm). The distance from the inlet of the channel to the axis of rotation is given by R_r/D_h = 20.0. The channel consists of an unheated smooth starting section (L_1/D_h = 10.3), a heated section with pins (L_2/D_h = 7.5 for channel A and L_2/D_h = 3.75 for channel B in Fig.4.1), and an unheated smooth exit section (L_3/D_h = 5.00). A summary of all six cases studied is given in Table 4.1.

Computational grid details

Fig. 4.2(a) shows the computational grid around the pins which model channel A with the AR=4:1 in Fig. 4.1(a). In this multi-block chimera grid system, the computational domain was divided into 25 overlapping and embedding chimera grid blocks (one block is for the rectangular duct and the other 24 blocks are for the pins) to simplify the grid generation process. Fig. 4.2(b) shows the computational grid around the pins which models channel B (Fig. 4.1(b)) which has a total of 6 rows of pins. For numerical grid (B), the number of grid points in the rectangular duct is 296 × 171 × 33 and the number of grid points for each pin is 62× 31 × 33, the identical grid distribution was applied in numerical grid (A). The total number of grid points is just over 3 million. Fig. 4.3(a) and 4.3(b) present grid refinement studies for *Re* =10,000 and 100,000, respectively, which indicates the present simulation results are nearly grid-independent.

4.2 Velocity and Temperature Fields

As summarized in Table 4.1, computations were performed with the Reynolds number (Re) ranging from 10^4 to 10^5, rotation number (Ro) from 0 to 0.28, inlet coolant-

Table 4.1: Summary of cases studied for duct with pin-fins

Case #	**Ro**	**$\Delta\rho/\rho$**	**β**	**Re**
1	0.00	0.122	-	10,000 (12 rows)
2	0.00	0.122	-	10,000
3	0.14	0.122	150°	10,000
4	0.00	0.122	-	100,000
5	0.14	0.122	150°	100,000
6	0.28	0.2	150°	100,000

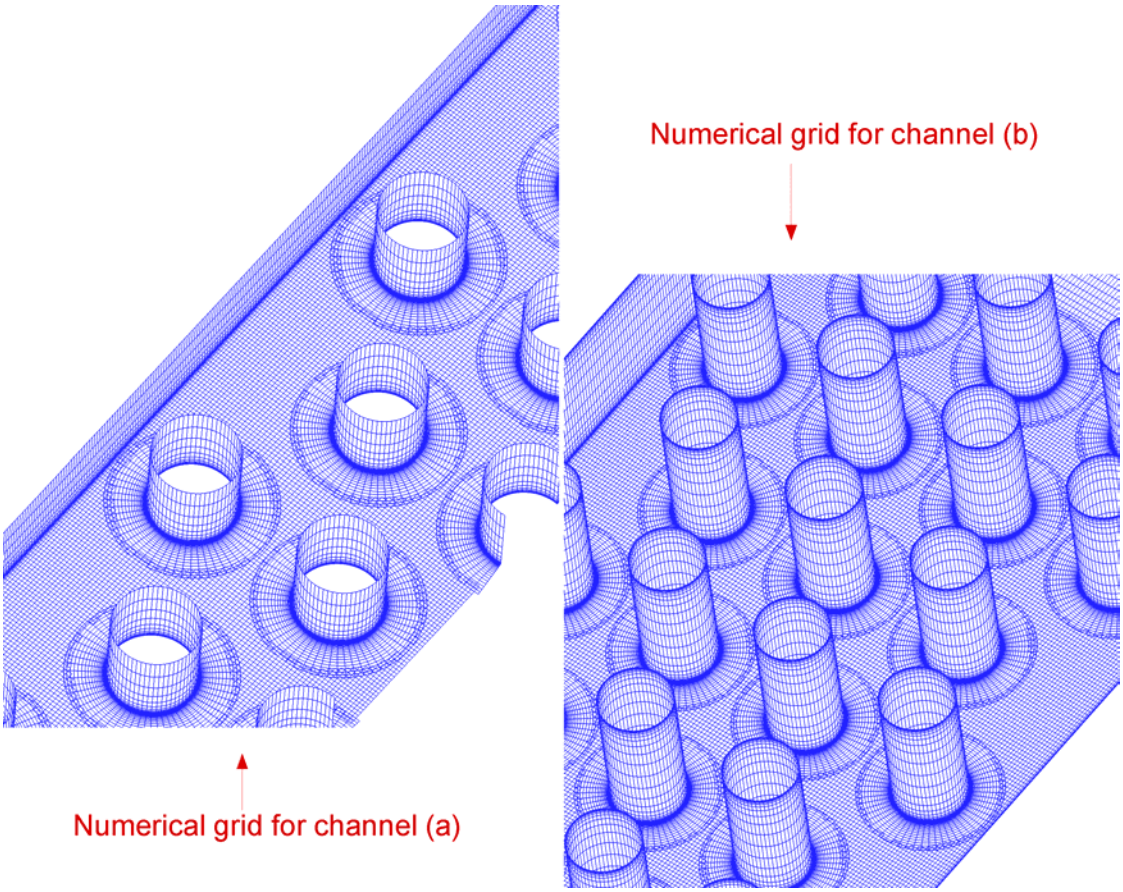

Fig. 4.2 Numerical Grid for (a) Full Channel and (b) One-Half Channel

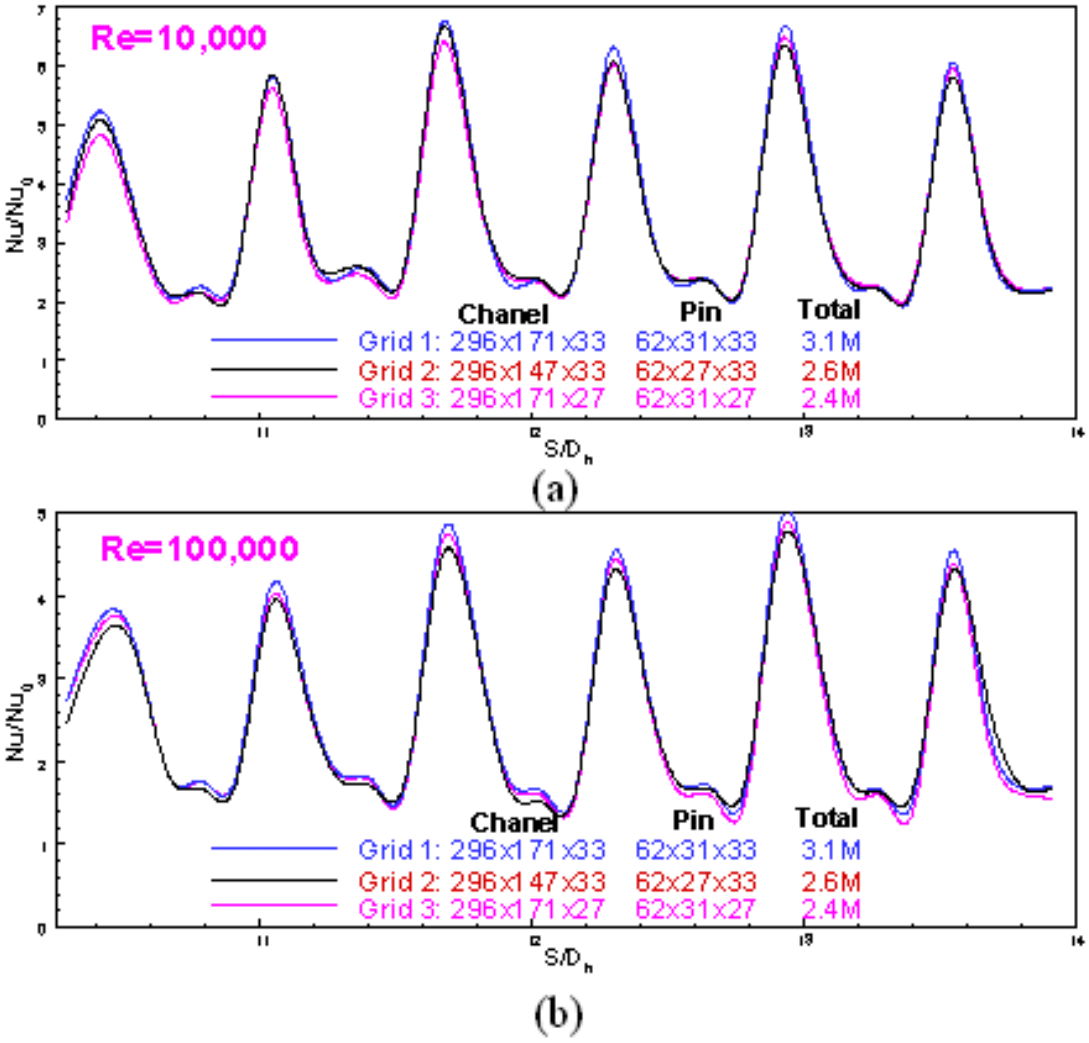

Fig. 4.3 Grid Refinement Study for Channel B at (a) Re = 10,000, Ro=0.0 and (b) Re = 100,000, Ro=0.00

to wall density ratio ($\Delta\rho/\rho$) from 0.122 to 0.2, and for the rotating cases, the channel orientation was fixed at 150^o.

Fig. 4.4 shows the velocity vector field and dimensionless temperature contours (θ) on the middle plane of symmetry between the leading and trailing surfaces for the non-rotating duct with 12 rows (Case 1) of pin-fins. As noted earlier, computations were performed for only one quarter of the channel since the flow is symmetric with respect to both y and z coordinates. As the flow approaches the first row of pin-fins, it accelerates around the circular pin-fins and boundary layer flow separation is observed downstream of the pin-fins. A pair of counter-rotating vortices are formed on the downstream face of each pin-fin. Due to the narrow spanwise spacing (S_2/D = 2) between the pin-fins, the mainstream flow accelerates in the gap region before impinging on the leading edge of the second row of pin-fins which are staggered to the first row pin-fins. In the present staggered pin-fin arrangement, the coolant was accelerates toward the leading edge of each pin and high heat transfer is produced on the front face of the pin-fin surface. As the mainstream flow is directed through the narrow passages between the second row of pin-fins, it also has a desirable effect of accelerating the wake flow behind the first row of pin-fins, and hence reduces the size of the separation bubble behind the first row. The relatively small pin-fin spacing (S_1/D = 2) in the streamwise direction also limited the longitudinal extent of the upstream pin-fin wakes to less than one pin-fin diameter due to strong mixing between the mainstream flow and the pin-fin wakes. As the mainstream flow moves around the second row of pin-fins, boundary layer separation occurs again and new wakes are formed downstream

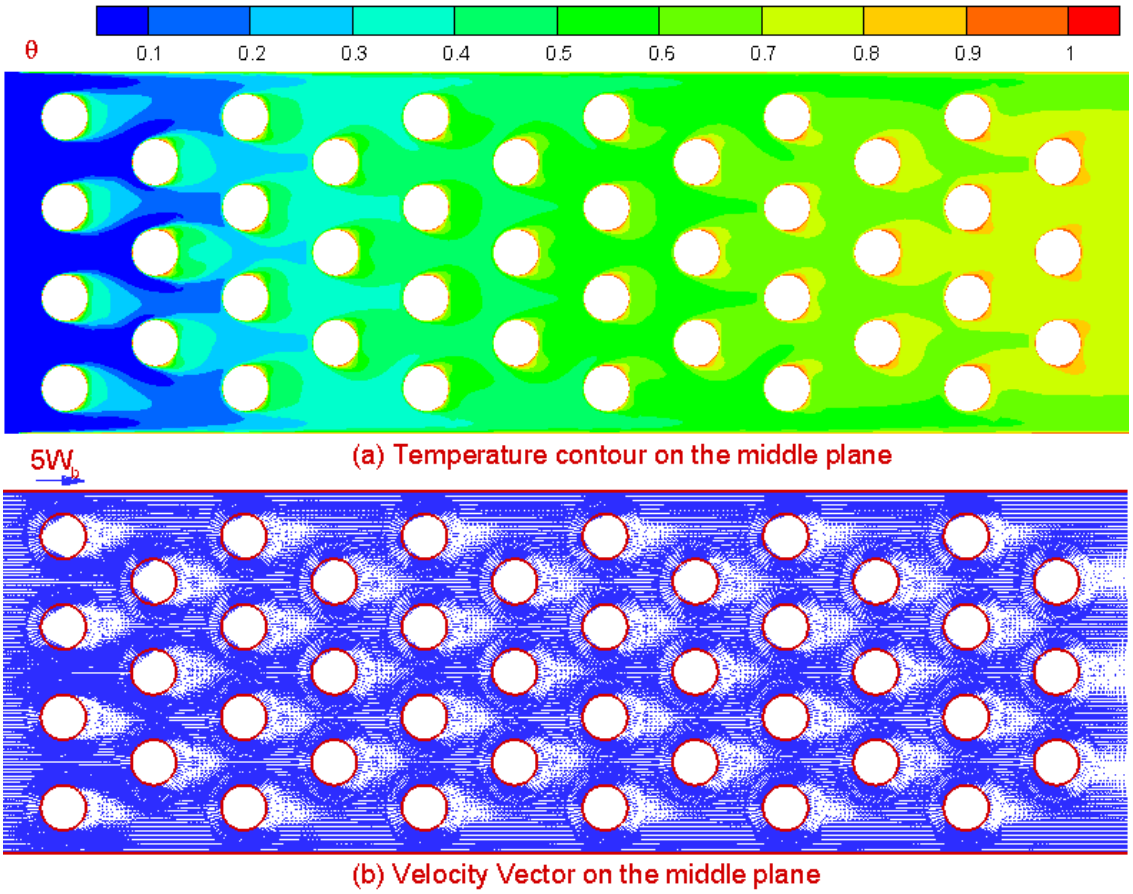

Fig. 4.4 Velocity and Dimensionless Temperature [$\theta = (T-T_i)/(T_w-T_i)$] Contours in the Middle Plane of Symmetry of the Non-Rotating Channel (Re = 10,000, $\Delta\rho/\rho = 0.122$)

of the pin-fins. The mainstream flow is redirected towards the leading edge of the third row pin-fins. The flow pattern around the third row pin-fins is similar to that observed earlier for the second row pin-fins except near the side wall regions. Due to the staggered pin-fin arrangement, there is strong interaction between the pin-fins and side walls for the odd row pin-fins. On the other hand, the side wall effects are negligible for even row pin-fins. It can be clearly seen from both the temperature contours and velocity vector plots that the wakes are skewed behind the odd row pin-fins since the wake flow is only partially blocked by the even row pin-fins in the side wall regions. A detailed examination of the temperature and velocity profiles indicate that the flow is sufficiently mixed with nearly periodic flow patterns beyond the third row pin-fins. It should also be noted that the wakes behind the last row of pin-fins are considerably wider and longer than those observed in previous rows due to the absence of a downstream row of pin-fins.

It is quite clear that the dimensionless temperature contours shown in Fig. 4.4 are closely related to the mainstream and secondary flow patterns induced by the pin-fins. The temperature is relatively low in the leading edge region of each pin-fin due to the impingement of the cooler mainstream fluid. On the other hand, the temperature is high immediately downstream of each pin-fin due to flow separation in the wake region. Near the side walls, the temperature is relatively low adjacent to odd row pin-fins due to the impingement of cooler mainstream fluid on the end walls.

Fig. 4.5 shows the dimensionless temperature contours on the planes near the trailing (or leading) surface of the non-rotating channel, as well as the pin-fin surfaces

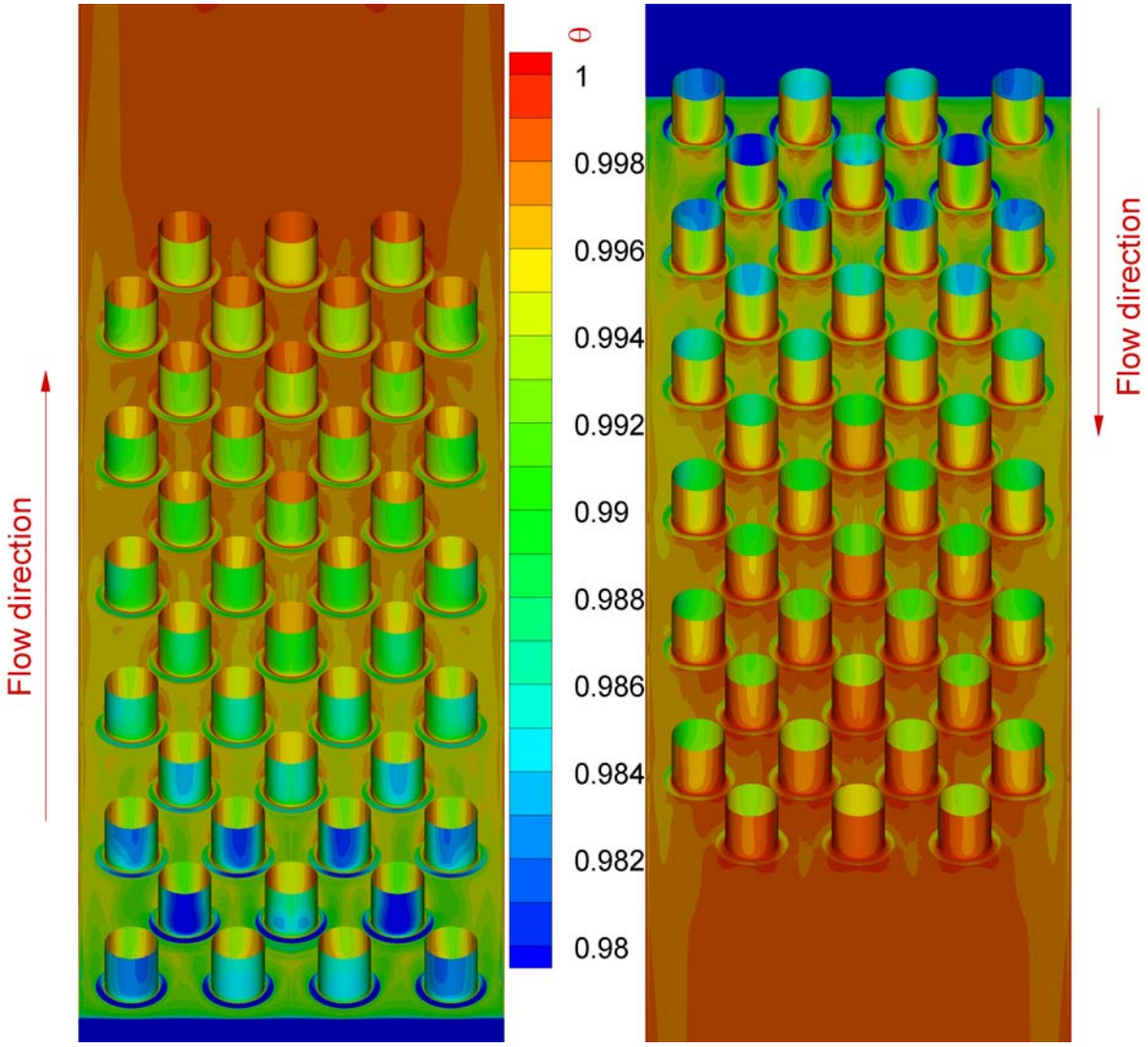

Fig. 4.5 Temperature [$\theta=(T-T_i)/(T_w-T_i)$] Contours Close to the Pin-Fins and the Trailing Surface of Non-Rotating Channel (Re = 10,000, $\Delta\rho/\rho = 0.122$)

($y^+ \sim 0.4$). Two different views, from upstream and downstream, of the channel are presented to provide a better understanding of the three-dimensional temperature around the leading and trailing edges of the pin-fins. It is clearly seen that the temperature is low on the front face of the pin-fins due to the impingement the of mainstream flow on the pin-fin leading edge. There is also a distinct low temperature region around the junction of each pin and the end wall. This ring-shaped low temperature region is produced by the horseshoe vortices which wrap around the junction of the pin-fin and channel end walls as shown in Fig. 4.6. The horseshoe vortices bring cooler fluid from the core region of the channel toward the channel end walls and produce high heat transfer on the leading and trailing surfaces of the cooling channel. On the other hand, the temperature on the downstream face of the pin-fins is quite high due to flow separation in the pin-fin wake.

It is interesting to note that the temperature of the second row pin-fins is lower than that of the first row since the mainstream flow accelerates between the first row pin-fins before impinging on the leading edge of the second row pin-fins. After the second row, the coolant temperature increases gradually downstream toward the channel exit. In general, the pin-fins induced strong turbulent mixing between the coolant in the core region and the hotter air near the channel end walls and pin-fins. The heat transfer is also enhanced around the junction of pin-fins and channel end walls due to the horseshoe vortices.

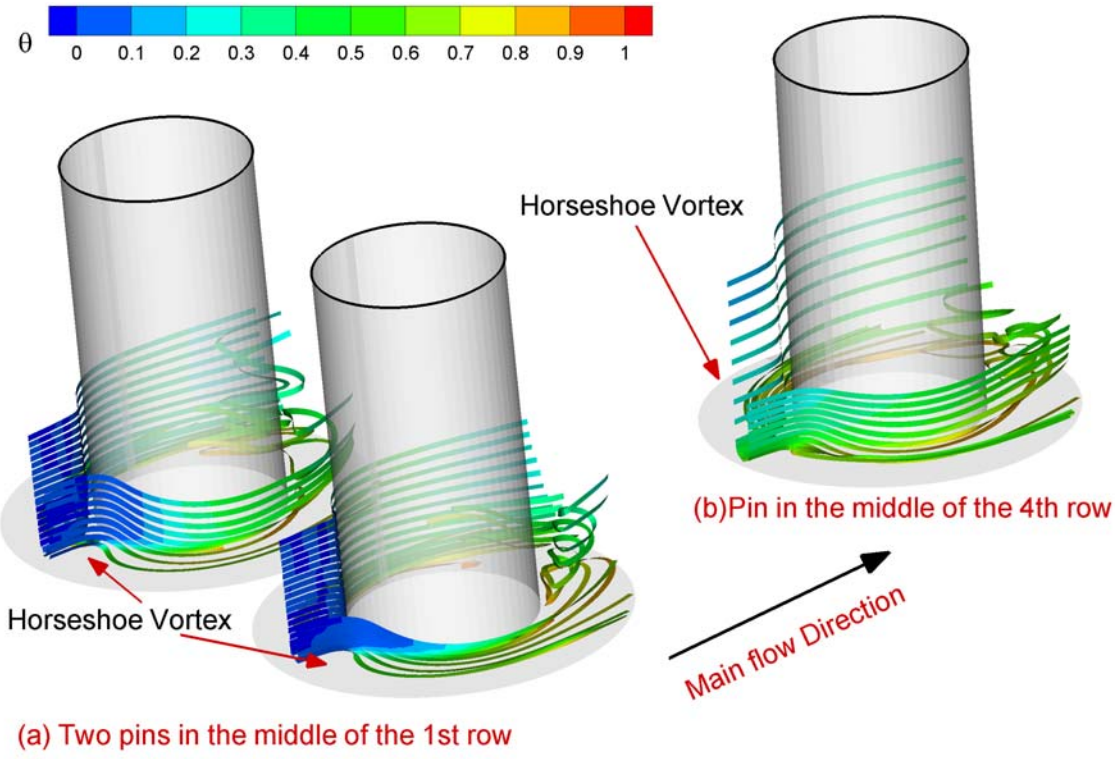

Fig. 4.6 Horseshoe Vortices and Temperature [$\theta=(T-T_i)/(T_w-T_i)$] Contours around Pin-Fins in the Non-Rotating Channel (Re = 10,000, $\Delta\rho/\rho$ =0.122)

4.3 Heat Transfer Coefficient Distribution

The Nusselt numbers presented here are normalized with a smooth tube correlation by Dittus-Boelter for fully developed, turbulent, non-rotating, tube flow.

Effect of rotation on heat transfer coefficient distribution

Fig. 4.7 shows the local Nusselt number ratio contours on the trailing surface of the channel and the pin-fin surfaces for Case 1 with 12 rows of pins. For completeness, the spanwise-averaged Nusselt number distributions were also calculated to provide a better understanding on the heat transfer enhancement due to the pin-fins. The numerical results indicate that the highest Nusselt number ratios are observed on the leading edge region of the pin-fins, while lowest Nusselt number ratios are observed in the wake region on the downstream face of the pin-fins. On the leading and trailing surfaces of the cooling channel, the Nusselt number ratio is high around the junction of the pin-fins and channel end walls due to the presence of the horseshoe vortices. It is also noted that the Nusselt number ratio for the first row pin-fins is quite low since the first row pins are exposed to uniform mainstream flow. In subsequent pin-fin rows, the Nusselt number ratio increases dramatically due to the acceleration of mainstream flow in the narrow gap between the pin-fins and the impingement of mainstream flow on the leading edge of the pin-fins.

It is noted that the spanwise-averaged Nusselt number ratio distribution reaches a maximum value on the third row and reduces only slightly downstream toward the channel exit. This suggests that the coolant is well mixed after the third row and exhibits a nearly periodic flow pattern in subsequent rows. In general, the spanwise-averaged

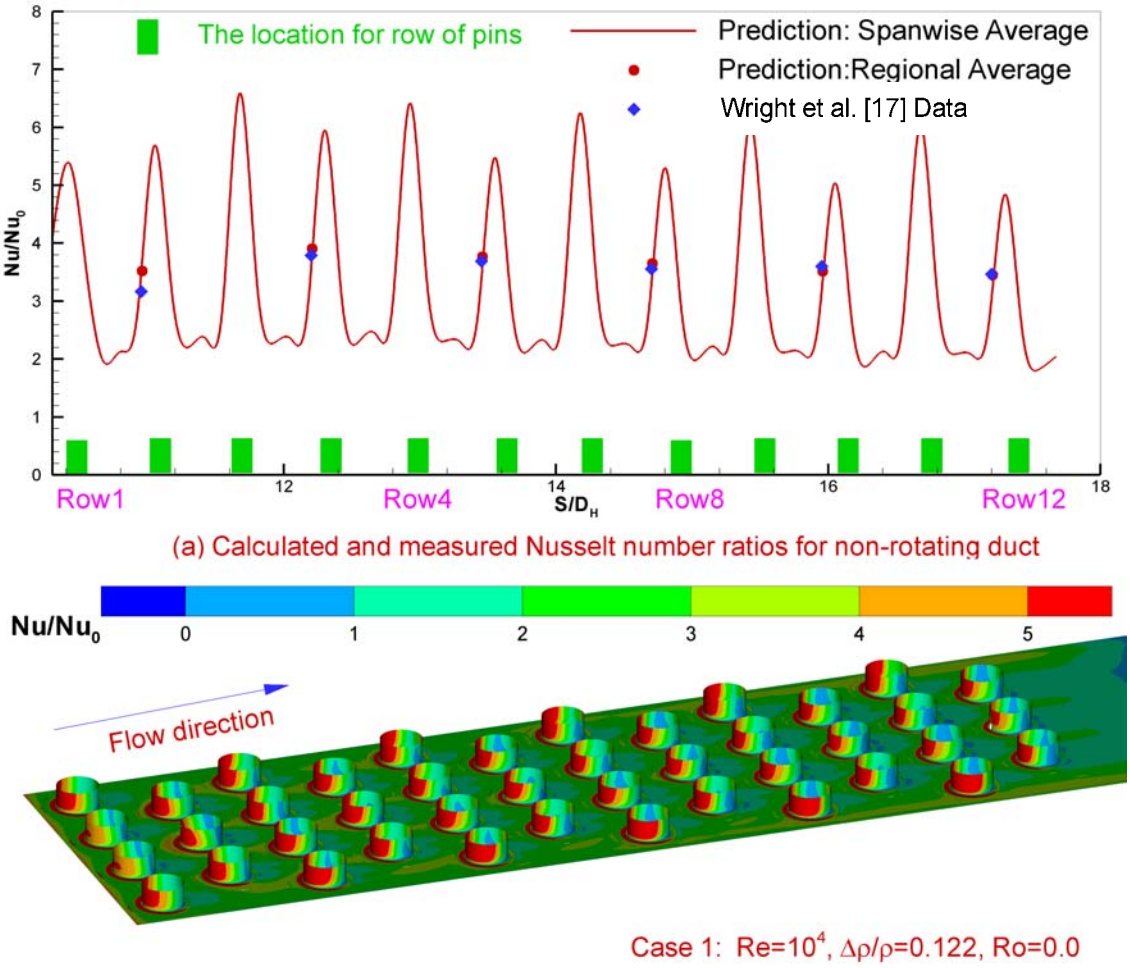

Fig. 4.7 Comparison between the Calculated and Measured Nusselt Number Ratios for the Non-Rotating Duct with 12 Rows of Pin-Fins ($Re = 10^4$, $\Delta\rho/\rho = 0.122$)

Nusselt number ratio is high (Nu/Nu_0 = 5~6.6) around the pin-fins but drops to approximately 2 between two rows of pin-fins. It is also interesting to note that the spanwise-averaged Nusselt number is higher around the odd number rows (except for the first row) since there are four pins on the odd number rows compared to three pins for the even number rows. Finally, it is also worthwhile to note that the calculated regionally-averaged (spanwise-averaged over certain S/D_h value) Nusselt number ratios are in close agreement with the experimental data of Wright et al.[48]. This clearly demonstrates the capability of the present near-wall second-order Reynolds stress closure model for accurate prediction of the heat transfer enhancement in pin-fin channels.

After successful validation of present numerical method for the non-rotating rectangular channel with 12 rows of pin-fins, calculations were then performed for rotating pin-fin channels to investigate the effects of rotation. Since the flow is no longer symmetric with respect to the y and z coordinates under rotating conditions, it is necessary to simulate the full channel configuration in order to correctly resolve the effects of the centrifugal and Coriolis forces. Due to the limitation of available computer resources, it was feasible for us to simulate only six rows of pin-fins for the full channel configurations (i.e., channel B). This is a reasonable simplification since the experimental data of Wright et al.[48] indicates that the Nusselt number ratio changes only slightly after the third row of pin-fins for both the non-rotating and rotating channel configurations. Calculations were performed for five different combinations of rotation number, Reynolds number, and coolant-to-wall density ratios as shown in Table 4.1

(Cases 2-6) for channel B. Note that the simulation for Re = 10,000 non-rotating case (Case 2) was repeated with six rows of pin-fins to facilitate a direct comparison on the effects of rotation and Reynolds number for channel B.

Fig. 4.8 shows the local Nusselt number ratio contours on the leading and trailing surfaces of the channel and pin-fin surfaces for the non-rotating and rotating channels with six rows of pins. Fig. 4.8(1a) and (1b) show that the Nusselt number ratio distribution is the same on both the leading and trailing surfaces for the non-rotating case. Similar to those observed in Fig. 4.6 for 12 rows of pins, the highest Nusselt number ratios are located on the leading edge region of pin-fins, while lowest Nusselt number ratios are located in the wake region near the leading and trailing surface of the non-rotating channel. Also, the Nusselt Number ratios on the pin surface of the third and forth rows of pin-fins are higher than those observed on the other four rows. In the rotating duct shown in Fig. 4.8(2a) and (2b), the rotation number is 0.14 while the density ratio is kept at 0.122. Compared to the non-rotating case, it is seen that the channel rotation leads to a small increase in the Nusselt number ratios on the trailing surface while the Nusselt number ratio on the leading surface changes only slightly. It is also noted that the channel rotation has negligible effect on the Nusselt number distributions on the pin-fin surfaces. In general, the combined effects of the centrifugal and Coriolis forces push the cooler fluid toward the trailing surface for the one-pass channel with radially outward flow. However, the rotation-induced secondary flow is not strong enough to change the turbulent mixing pattern around the short and densely spaced pin-fins.

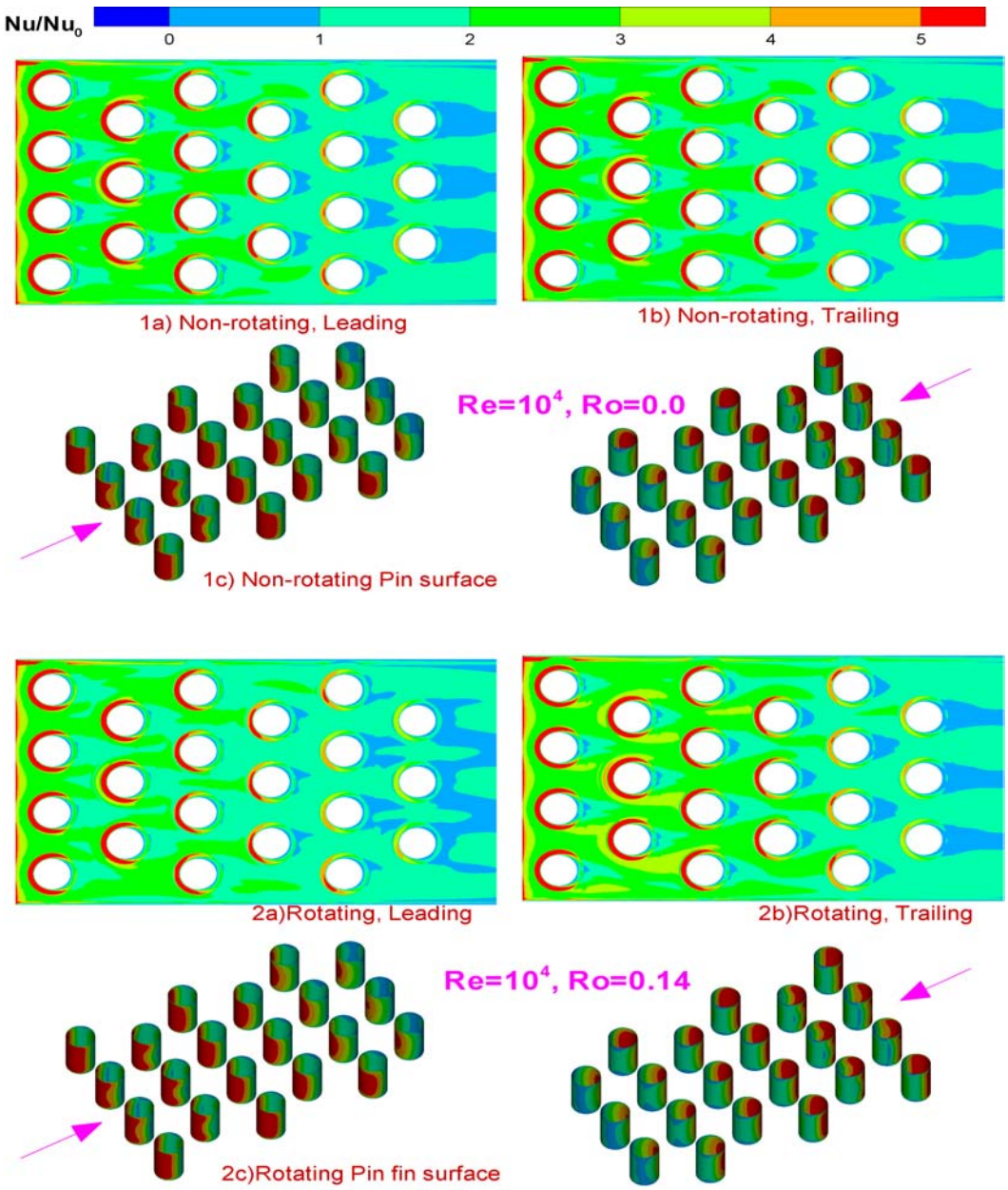

Fig. 4.8 Nusselt Number Ratio Contours on (a) Leading and (b) Trailing Surface for Lower Reynolds Number (Re = 10,000) Cases

Figure 4.9 presents the spanwise-averaged Nusselt number ratios for the non-rotating (Case 2) and rotating (Case 3: $\beta = 150°$) pin-fin channels at Re = 10,000 and $\Delta\rho/\rho$=0.122. Regionally-averaged (spanwise averaged over certain S/D_h value) Nusselt number ratios were also computed and compared to the corresponding experimental data for the same cases. In general, the numerical predictions are in good agreement with the experimental data for both the rotating and non-rotating cases, except for the inlet of the non-rotating case and the exit of the rotating case. This discrepancy may be partially attributed to the constant wall temperature boundary condition used in the present calculations in comparison with the constant wall heat flux boundary condition used in the measurement.

Fig. 4.10 shows the effect of channel rotation on the numerically predicted spanwise-averaged Nusselt number ratio distributions. It is noted that the spanwise-averaged Nusselt number distributions on both the leading and trailing surfaces show periodic peaks, as those seen earlier in Fig. 4.7. The two highest peaks correspond to the first and third rows of pin-fins and are caused primarily by the impingement of mainstream flow on the leading edge region of the four pins. The lower peaks are corresponding to the even number rows with 3 pins, while the lowest Nusselt number ratios are located in the wake region between two rows of pin-fins. As noted earlier, channel rotation leads to a small increase in the Nusselt number on the trailing surface and a very slight decrease in the Nusselt number on the leading surface. The maximum Nusselt number is located at the channel inlet where the thermal boundary layer is very thin. The peak values of the Nusselt number ratio occur next to the odd rows (first,

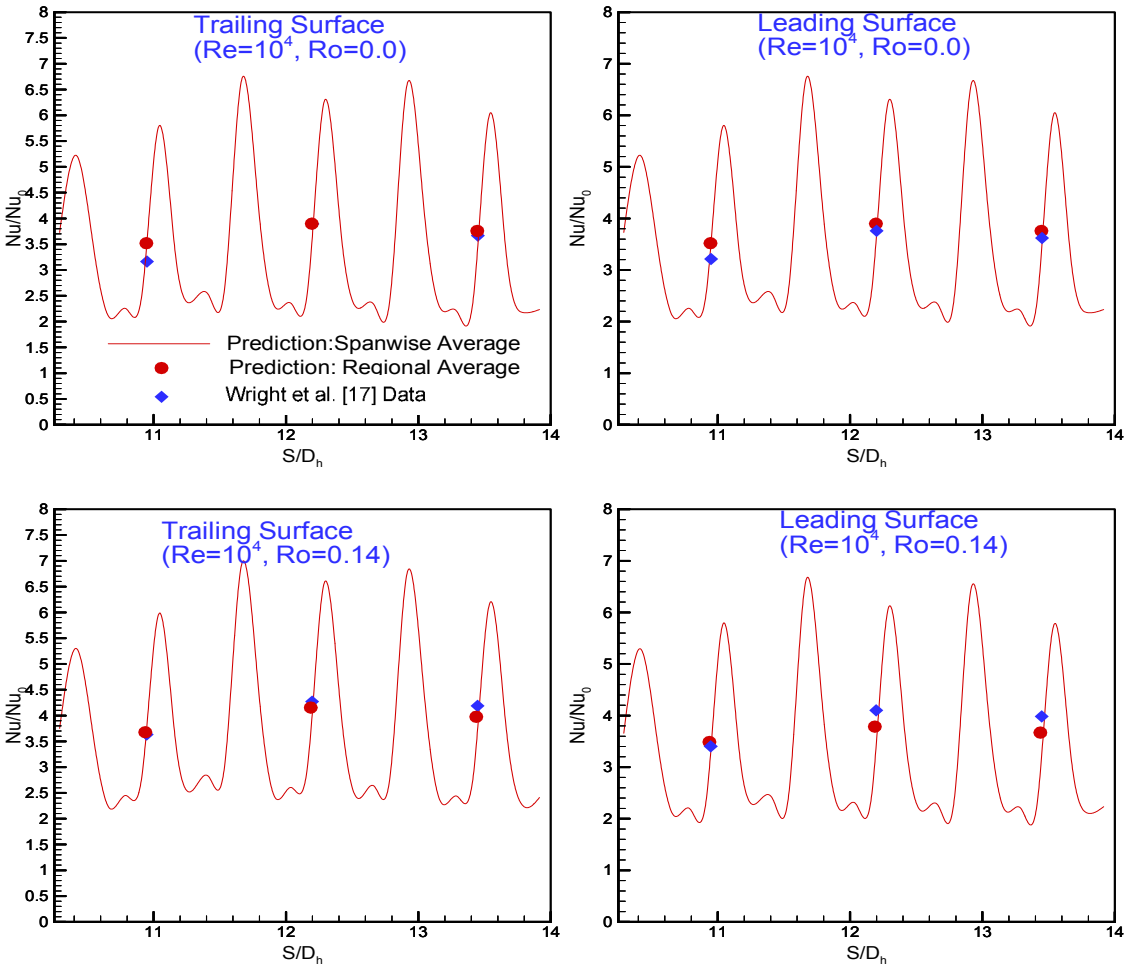

Fig. 4.9 Comparison between Calculated and Measured Nusselt Number Ratios for Non-Rotating and Rotating (Ro=0.14, $\beta = 150°$) Ducts ($Re=10^4$, $\Delta\rho/\rho=0.122$)

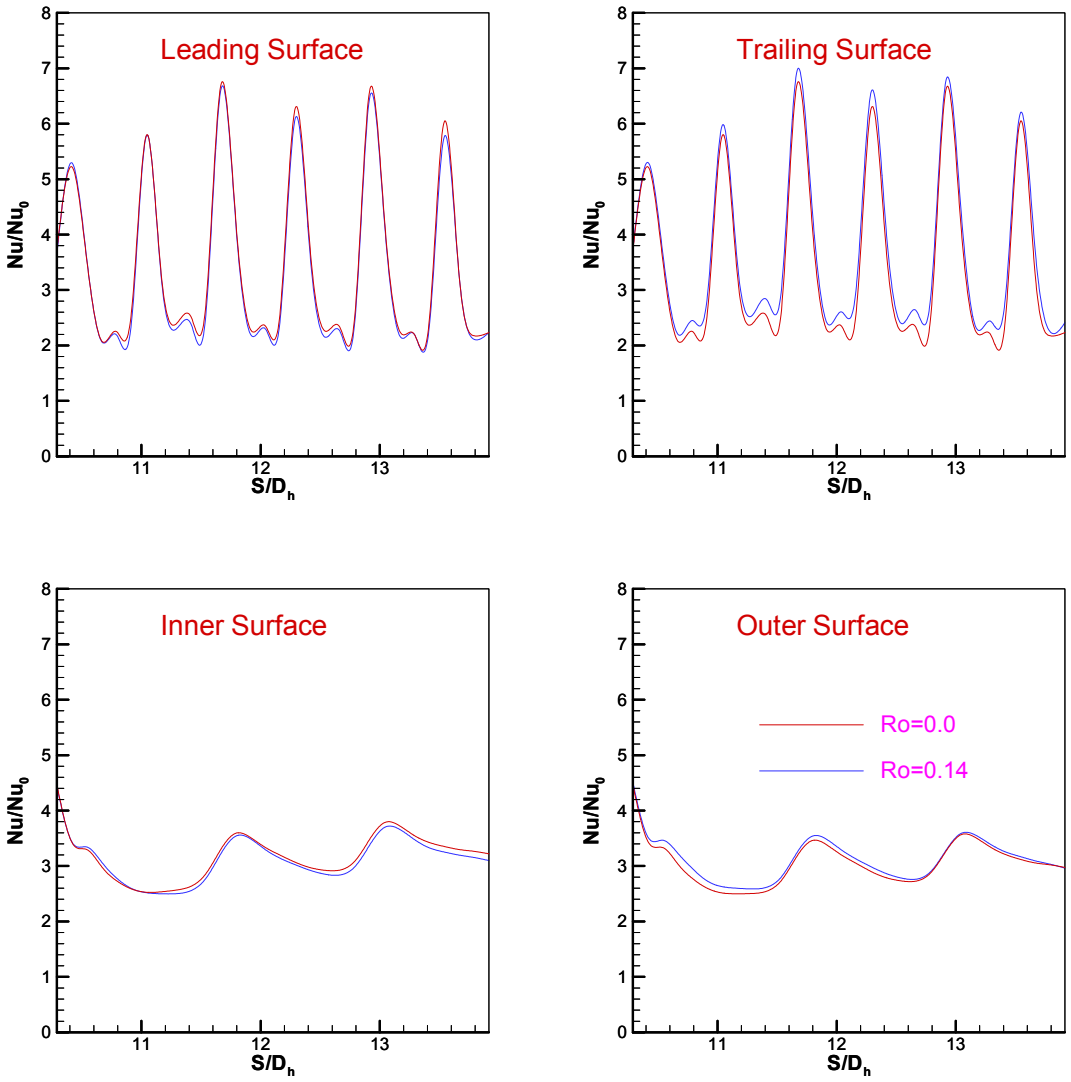

Fig. 4.10 Effect of Rotation on Spanwise-Averaged Nusselt Number Ratios for Lower Reynolds Number (Re = 10,000) Cases

third, and fifth rows) of pin-fins as a result of flow impingement in the narrow gap region between the pin-fins and side walls. The lowest Nusselt number ratios are observed around the second and fourth rows where the interaction between the pin-fins and side walls is weak. It is also noted that the channel rotation has negligible effects on the magnitude of the spanwise-averaged Nusselt number ratios on side walls.

Effect of high Reynolds number on heat transfer coefficient distribution

In addition to the low Reynolds number cases presented above (Cases 2 and 3), calculations were also performed for high Reynolds number, high density ratio, and high rotation number cases (i.e, Cases 4-6) which are closer to the cooling configurations of power generation turbine blades. In these calculations, the Reynolds number is increased from 10^4 to 10^5; the rotation number is doubled from 0.14 to 0.28; and the density ratio is increased from 0.122 to 0.2.

Fig. 4.11 shows the detailed Nusselt number ratio contours on the leading and trailing surfaces of the channel with six rows of pins for the high Reynolds number cases. Similar to those observed in the low Reynolds number cases, the highest Nusselt number ratios are located on the leading edge region of pin-fins, and the lowest Nusselt number ratios are found in the wake region on the leading and trailing surfaces. The maximum Nusselt number ratio is also attained at the third and fourth rows. A comparison of the detailed Nusselt number ratio distributions on the leading, trailing, and pin-fin surfaces indicate that the channel rotation has negligible effect on the heat transfer augmentation. This is to be expected since the Nusselt number for a smooth

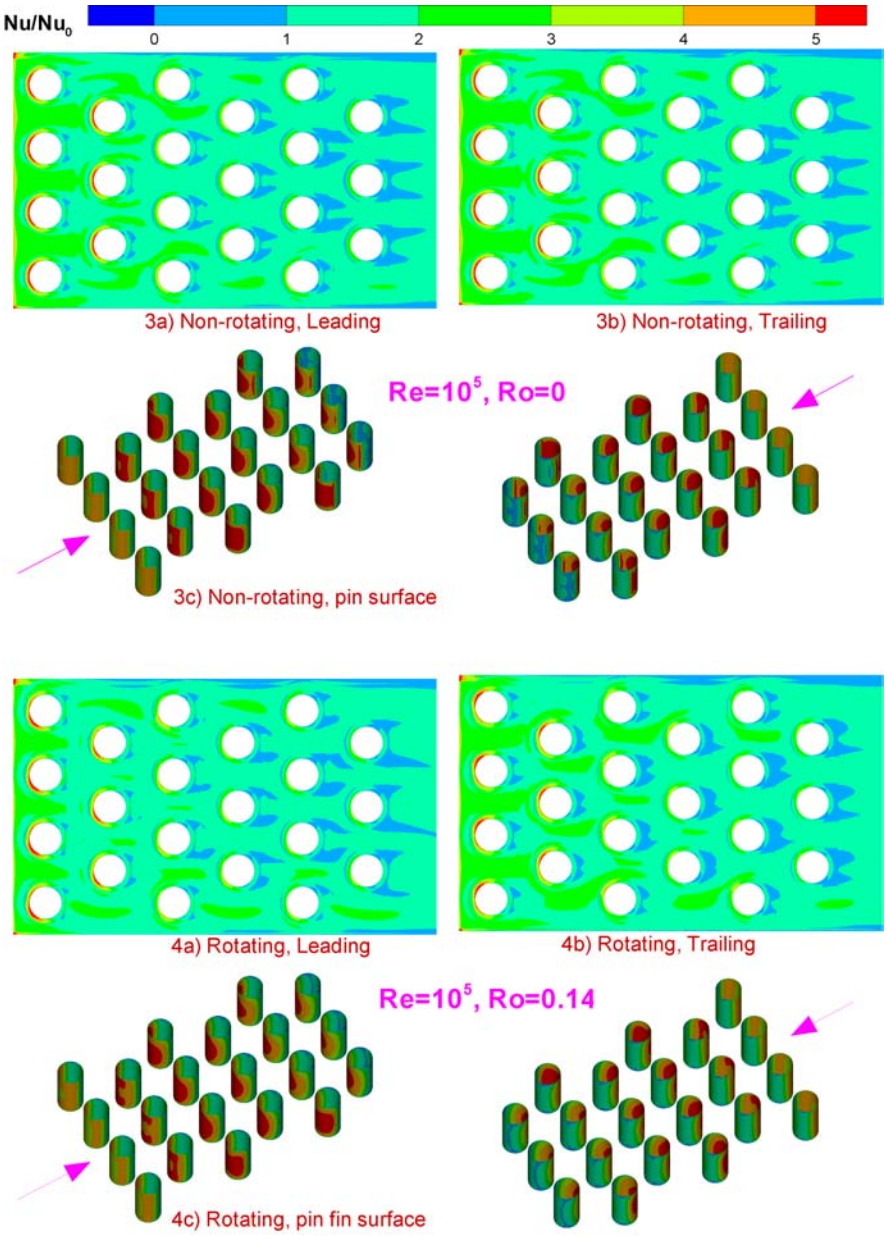

Fig. 4.11 Nusselt Number Ratio Contours on (a) Leading and (b) Trailing Surface for Higher Reynolds Number (Re = 100,000) Cases

duct (proportional to $Re^{0.8}$) is already very high due to high turbulence and a high temperature gradient in the boundary layer.

Fig. 4.12 shows the spanwise-averaged Nusselt number ratios for the non-rotating duct at two different Reynolds numbers of 10^4 and 10^5. It is seen that the Nusselt number ratios decrease sharply on all four walls as the Reynolds number increases. This indicates that the pin-fins produce more heat transfer enhancement for lower Reynolds number flows. However, the actual Nusselt numbers are much higher for the high Re cases because the Nu_o for the smooth duct (proportional to $Re^{0.8}$) is already very high in these cases due to the high turbulence and high temperature gradient in the boundary layer.

Effect of rotation and density ratio on heat transfer coefficient distribution

Fig. 4.13 shows a comparison of the spanwise averaged Nusselt number ratios for high Reynolds number cases under non-rotating (Case 4) and rotating with Ro = 0.14 (Case 5) and Ro = 0.28 (Case 6) conditions. It is seen that the effect of channel rotation has only minor effects on the heat transfer enhancement even if the rotation number is doubled from 0.14 to 0.28 and the density ratio is increased from 0.122 to 0.20. It is quite obvious that the rotation-induced secondary flow is not strong enough to change the flow and heat transfer characteristics which are dominated by strong turbulent mixing induced by pin-fins and high Reynolds number boundary layer flow.

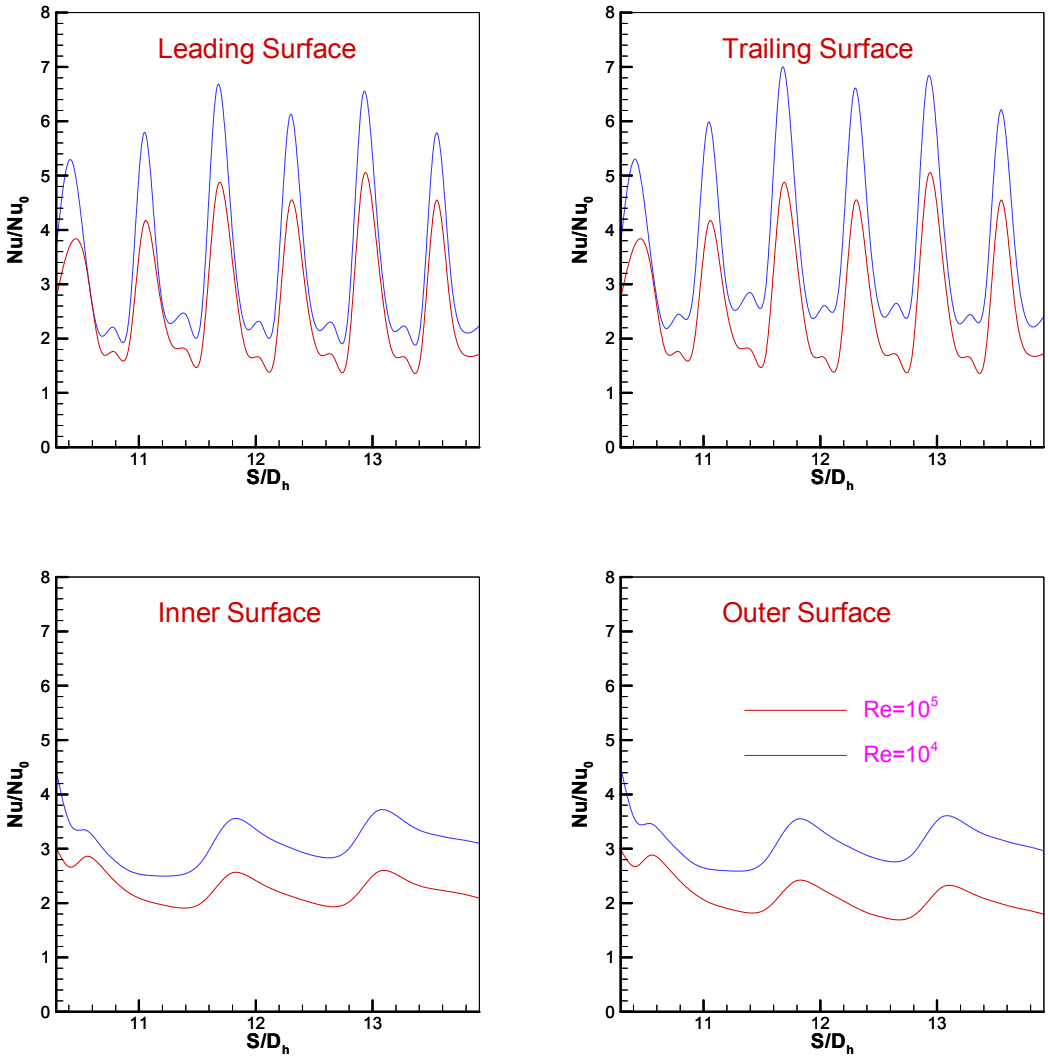

Fig. 4.12 Effect of Reynolds Number on Spanwised-Averaged Nusselt Number Ratios for Non-Rotating Duct (Ro = 0.0, $\Delta\rho/\rho = 0.122$)

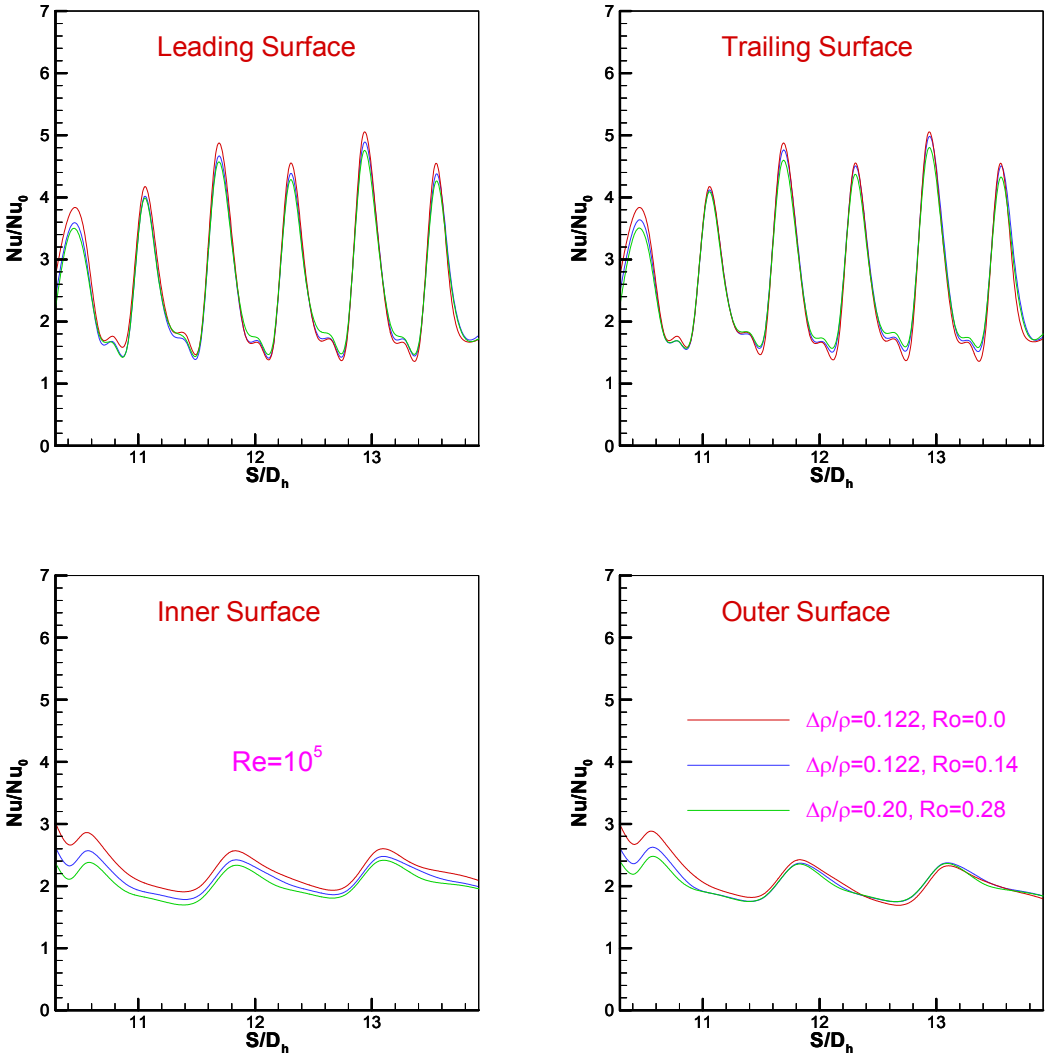

Fig. 4.13 Effect of Rotation and Density Ratio on Spanwise-Averaged Nusselt Number Ratios for High Reynolds Number (Re = 100,000) Cases

CHAPTER V

FLOW AND HEAT TRANSFER IN ROTATING TWO-PASS RECTANGULAR CHANNELS (AR=1:1, 1:2, AND 1:4) WITH SMOOTH WALLS

In this chapter, we perform calculations for rotating/non-rotating two pass rectangular channels (AR=1:1, 1:2, and 1:4) with smooth wall as tested by Fu et al.[63] using the near wall second-order Reynolds stress closure model.

5.1 Description of Problem

A schematic diagram of the geometry for AR=1:4 duct is shown in Fig. 5.1. As mentioned earlier, this investigation covers three channels with different aspect ratios (AR = 1:1, AR = 1:2 and AR = 1:4). For the sake of brevity, however, only the geometry for the AR = 1:4 channel is given in Fig. 5.1. All three ducts have the same length, same bend radius, and the same width between the inner and outer wall. Of the four side walls, the two in the rotational direction are denoted as leading and trailing surfaces, while the other two are denoted as inner and outer surfaces. The total length of the channel, L, equals to 37.47cm (14.75 in), the distance from the inlet of the channel to the axis of rotation is given by R_r = 40.64cm (16 in). The channel consists of an unheated smooth starting section (L_1 = 22.23cm (8.75 in)) and a heated section (L_2 = 15.24cm (6 in)). The radius of curvature of the 180° sharp turn is r_i = 0.635 cm (0.25 in) and the minimum gap G between the inner and outer surfaces of the bend is 1.27 cm (0.5 in). The channel width W is kept the same at 1.27 cm (0.5 in) for all three different aspect ratio channels. The channel height is increased from 1.27 cm (0.5 in) for square duct to 5.08 cm (2.0 in)

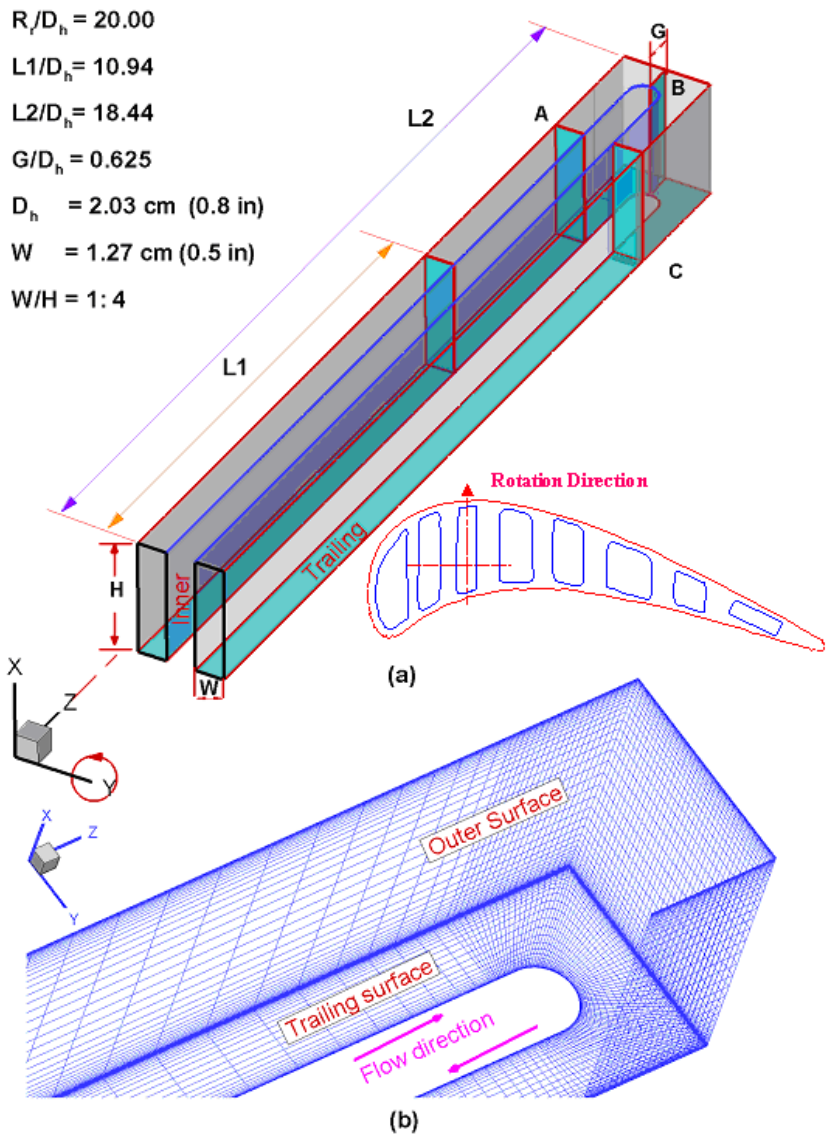

Fig. 5.1 Geometry and Conceptual View of Rotating Channel Orientation for Rectangular Duct (AR=1:4) and Numerical Grid

for AR =W/H = 1:4 channel. It should be noted that the hydraulic diameters D_h are different for different aspect ratio channels with D_h = 1.27 cm, 1.69 cm, and 2.03 cm for AR = 1:1, 2:1, and 4:1 channels, respectively. For the rotating cases, the channel orientations is given as $\beta = 90°$. A summary of all fifteen (15) cases studied is given in Table 5.1. Because the hydraulic radius are different for different aspect ratio ducts, it is necessary to adjust the channel inlet velocity and rotating speed in order to maintain the same Reynolds number and the same rotation number in the present numerical simulations.

Computational grid details

Fig. 5.1(b) shows the computational grid for the smooth rectangular duct with AR = 1:4. For the sake of brevity, the numerical grids for AR = 1:1 and AR = 1:2 channel are not included here. A systematic grid refinement study was performed for all three different aspect ratio ducts. The grid refinement in the axial direction at the bend region has produced only minor changes of Nusselt number ratio. The refinement of cross sectional grids resulted in a maximum improvement of 3.5% in Nusselt number ratios when the grid number increase about 50 %. The minimum grid spacing for the Re = 100,000 cases is maintained at 2×10^{-5} of the hydraulic diameter which corresponds to wall coordinate y^+ on the order of 0.1 also. The refinement in the axial direction at the bend region produced only minor changes of Nusselt number ratio, while the refinement of cross sectional grids caused a maximum of 4.1% improvement at the bend region in Nusselt number ratios when the grid number increase about 50 %.

Table 5.1: Summary of cases studied for two-pass smooth ducts

Case #	**AR**	β	**Re**	**Ro**	$\Delta\rho/\rho$
Case1	1:1	-	10,000	0.0	0.13
Case2	1:1	90^0	10,000	0.14	0.13
Case3	1:2	-	10,000	0.0	0.13
Case4	1:2	90^0	10,000	0.14	0.13
Case5	1:4	-	10,000	0.0.0	0.13
Case6	1:4	90^0	10,000	0.14	0.13
Case7	1:1	-	100,000	0.0	0.13
Case8	1:1	90^0	100,000	0.28	0.20
Case9	1:2	-	100,000	0.0	0.13
Case10	1:2	90^0	100,000	0.28	0.20
Case11	1:4	-	100,000	0.0.0	0.13
Case12	1:4	90^0	100,000	0.28	0.20
Case13	1:1	90^0	100,000	0.28	0.40
Case14	1:2	90^0	100,000	0.28	0.40
Case15	1:4	90^0	100,000	0.28	0.40

5.2 Velocity and Temperature Fields

Fig. 5.2 shows the dimensionless temperature contour (θ) and the velocity vector field in the heated section at the middle plane between the leading and trailing surfaces for all three non-rotating ducts. It is noted that the flow patterns are similar in the first pass before the bend. The flow separations occur almost at the same location since the band radius is the same for all three ducts and the flow is fully developed before reaching the bend. On the other hand, the heat transfer characteristics are significantly different in the second pass because the secondary flows induced by the bend are drastically different for different aspect ratio channels. It can be seen that the high-momentum fluid entering the turn from the inflow passage impinges on the outer wall. As the flow turns into the second passage, the high-momentum flow again impinges on the outer wall. These flow impingements produced two distinct high heat transfer enhancement regions along the outer wall which will be discussed in detail in the next section.

Fig. 5.3 shows the dimensionless temperature contour (θ) and the vector field for Re = 10,000 cases at three axial stations A, B, and C as denoted in Fig. 5.1. Moreover, the Nusselt number ratios on all four walls are also shown in Fig. 5.3 to facilitate a detailed understanding of the heat transfer characteristics in different aspect ratio channels. Note that the Nusselt numbers presented here are normalized by the smooth tube correlation of Dittus-Boelter.

For the three non-rotating ducts, it is seen from that the anisotropy of the turbulent Reynolds stresses produced eight small secondary corner vortices in the first passage for

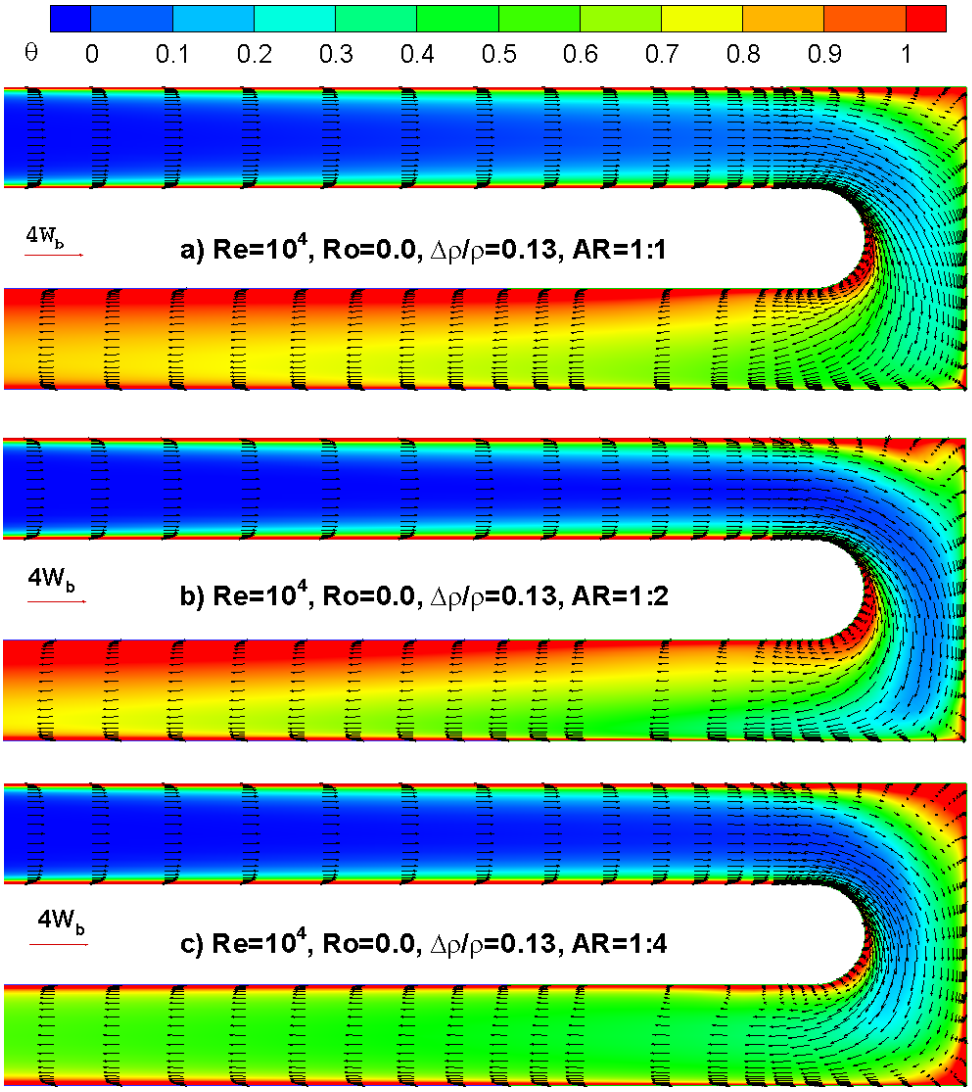

Fig. 5.2 Velocity and Dimensionless Temperature [$\theta = (T-T_i)/(T_w-T_i)$]

Contours in the Middle Plane of Symmetry of the Non-Rotating Channel

(Re = 10,000, $\Delta\rho/\rho = 0.13$)

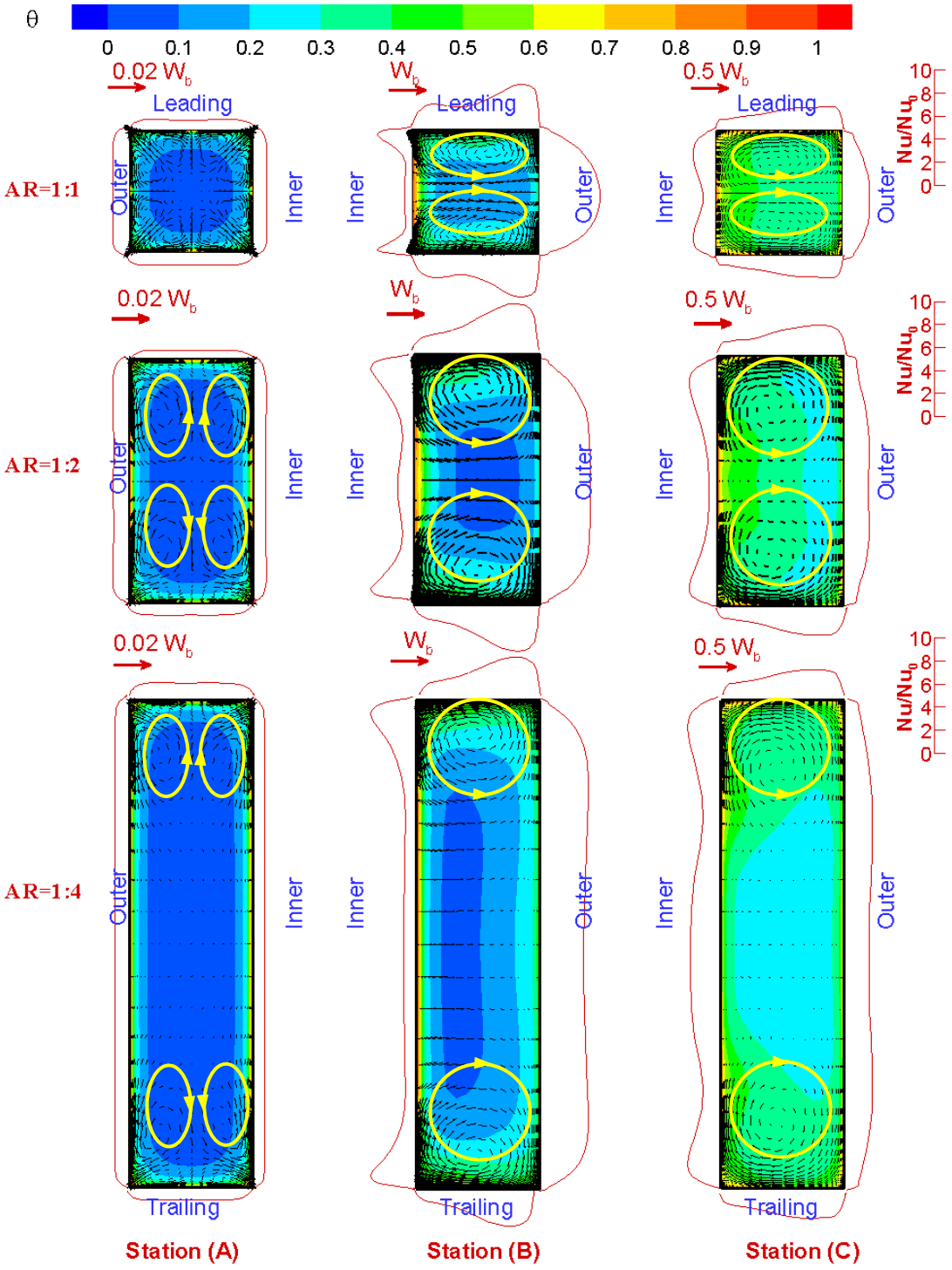

Fig. 5.3 Secondary Flow, Temperature [$\theta=(T-T_i)/(T_w-T_i)$] Contours, and Nusselt Number Ratios for Non- Rotating Ducts (Re=10,000, $\Delta\rho/\rho=0.13$)

all three channels. These vortices grow in the vertical direction as the channel aspect height was increased from AR = 1:1 to AR = 1:2. However, the vortices cease to expand in the vertical direction when the channel height was further increased to AR = 1:4. It should be noted that these Reynolds-stresses-driven vortices are rather weak and did not significantly alter the Nusselt number ratios along the channel surfaces. As the fluid flows through the180° bend, the centrifugal forces arising from the curvature and the associated pressure gradients (low pressure at inner surface, high pressure at outer surface) produced a pair of counter-rotating vortices in the bend. These vortices are significantly stronger than those vortices observed in the first passage and are responsible for the transport of cool fluid from the core toward the outer surface. Before the bend, the cooler fluid is located in the core region. After the bend, however, the cooler fluid is pushed toward the outer surface by the centrifugal force induced by the streamline curvatures. This leads to steeper temperature gradients on the outer wall than on the inner wall after the bend as shown in Station (C) of Fig. 5.3.

It is further noted in Fig. 5.3 that there are distinct differences in the secondary flow patterns for different aspect ratio ducts. For the square duct, the counter-rotating vortex pair generated by the bend is squashed in the vertical direction due to the tight spacing between the leading and trailing surfaces. In the low aspect ratio rectangular ducts, however, the vortices induced by the 180° turn tend to maintain circular shapes up to the space limitations rather than expanding continuous in the vertical direction. In the AR = 1:1 and 1:2 channels, the counter-rotating vortices occupy the entire channel and bring cooler fluid in the core region towards the outer surface at both Stations (B) and

(C). For the AR = 1:4 channel, however, the nearly circular vortex pair are confined to the leading and trailing surfaces. Even though the secondary flow is very weak in the middle section of the AR = 1:4 channel, the additional pressure gradients induced by the counter-rotating vortices still apply over the entire channel cross-section. Consequently, the cooler fluid in the middle section of the AR = 1:4 channel was pushed by the vortex-induced pressure gradients back towards the inner surface as seen in Station (B).

Fig. 5.4 shows the cross-stream velocity vectors and the temperature contours for the Re = 10,000 rotating ducts at the same location as those presented in Fig. 5.3. It is quite clear that the flow patterns in both the first and second passages were significantly modified by the rotation-induced vortices. In the first passage, the Coriolis forces produce a pair of counter-rotating vortices which moves cooler fluids in the core region toward the trailing surface of the rotating ducts. In the second passage, the Coriolis force acts in the opposite direction, which pushes the cold fluid toward the leading surface. In the bend, the vortex pair formed in the first passage by channel rotation is overpowered by the bend-induced vortices. The combined effects of the rotation- and turn-induced vortices increases the strength and size of the vortex near the leading surface as seen in Fig. 5.4(B). In the second passage, the larger vortex near the leading surface continued to grow and eventually occupied almost the entire space. This flow pattern is further modified by the centrifugal buoyancy force which plays an opposite role in the second passage as it does in the first passage. The combination of these forces influences the heat transfer characteristics which will be presented in the next section.

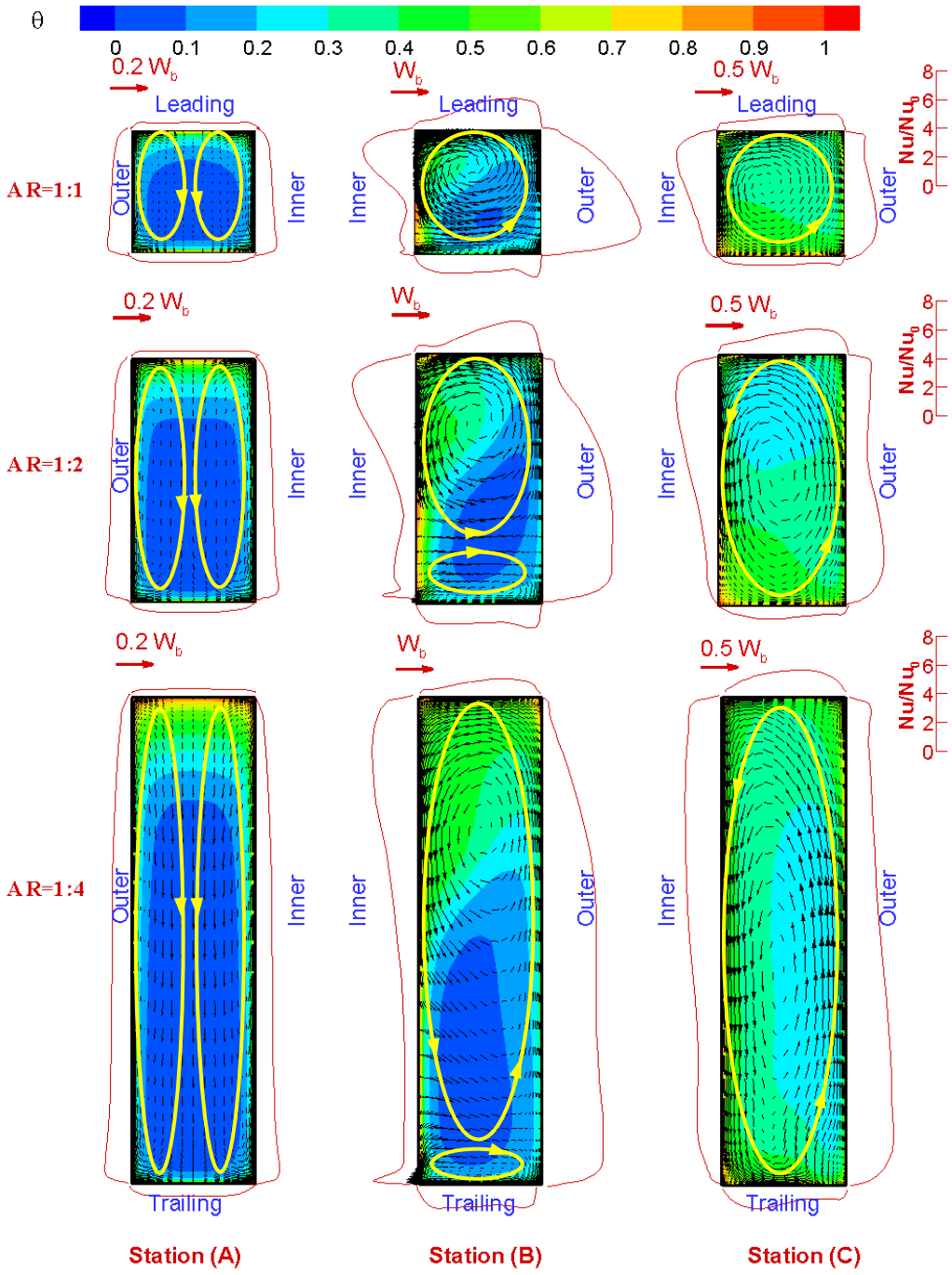

Fig. 5.4 Secondary Flow, Temperature [$\theta=(T-T_i)/(T_w-T_i)$] Contours, and Nusselt Number Ratios for Rotating Ducts (Re=10,000, Ro=0.14, $\Delta\rho/\rho=0.13$)

Fig. 5.5 shows the velocity and temperature contours for non-rotating ducts for the high Reynolds number (Re=100,000) cases. Comparing Fig. 5.5 with Fig. 5.3 for non-rotating ducts, the thermal boundary layers become thinner at higher as the Reynolds number increases. The overall secondary flow patterns are quite similar between the low and high Reynolds number cases, but the bend-induced vortices are somewhat stronger at Re = 100,000. For the AR = 1:1 and 1:2 channels, the cooler fluids at section (B) were pushed toward the outer surface by the centrifugal force and the bend-induced vortices which occupy the entire channel cross-section. For the AR = 1:4 channel, however, the counter-rotating vortices were again confined to the leading and trailing surfaces and the cooler fluid in the middle section was pushed toward the inner surface by the vortex-induced pressure gradients.

Fig. 5.6 shows the effects of high Reynolds number (Re = 100,000) and high rotation number (Ro = 0.28) on the temperature contours and secondary flow vectors. Comparing to the low-Re and low-Ro cases shown in Fig. 5.4, it is clearly seen that the rotation-induced vortices become stronger when both the Reynolds number and rotation number were increased. In the bend region, however, the vortices induced by the turn were also strengthened as the Reynolds number was increased from Re = 10,000 to Re = 100,000. It is noted that the rotation-induced vortices are still relatively weak in comparison with the bend-induced vortices (see Fig. 5.5) even though the rotation number was doubled from 0.14 to 0.28. In the second passage, the vortex adjacent to the leading surface grows considerably but the vortex next to the trailing surface remains

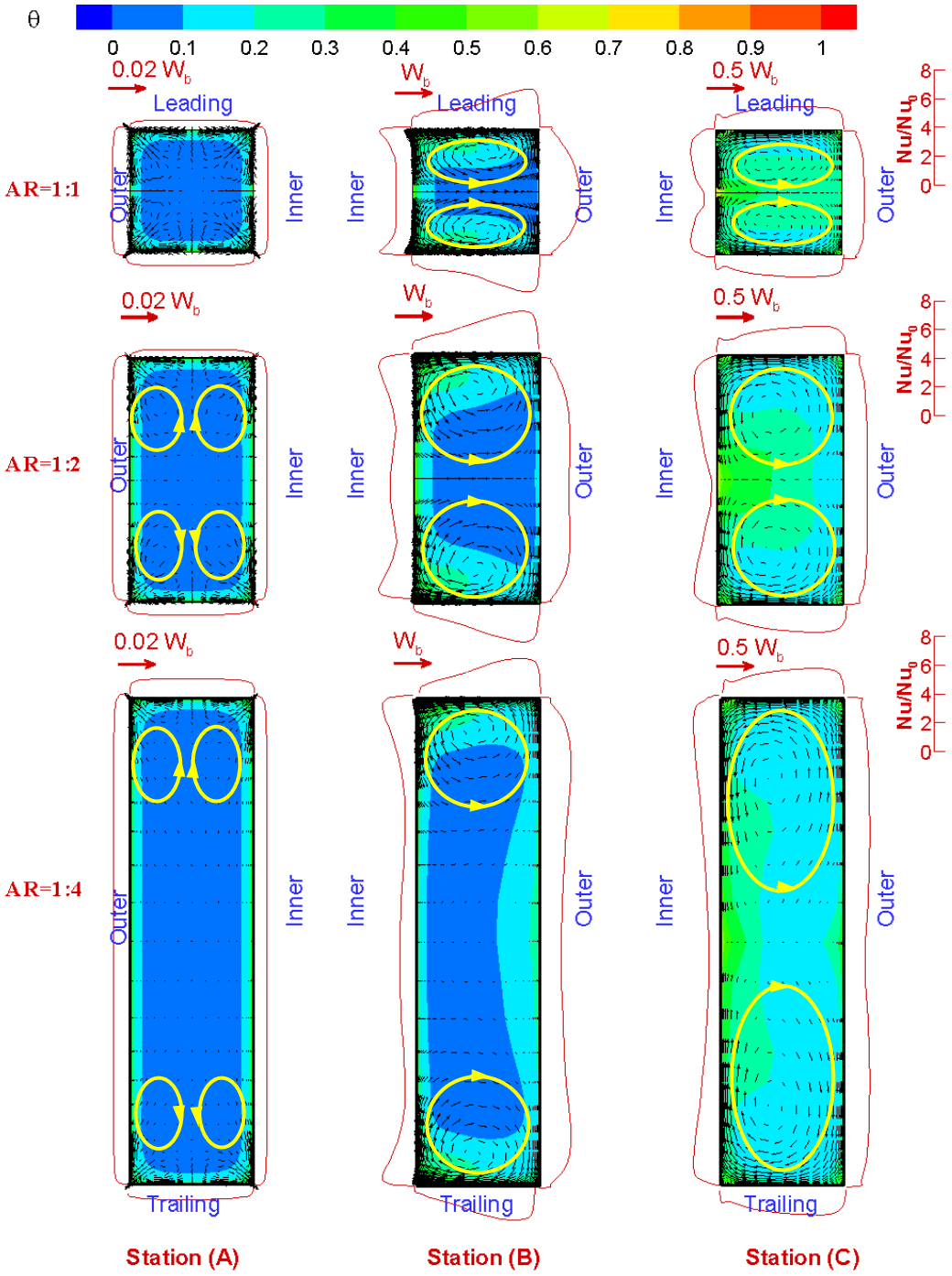

Fig. 5.5 Secondary Flow, Temperature [$\theta=(T-T_i)/(T_w-T_i)$] Contours, and Nusselt Number Ratios for Non- Rotating Ducts (Re=100,000, $\Delta\rho/\rho=0.13$)

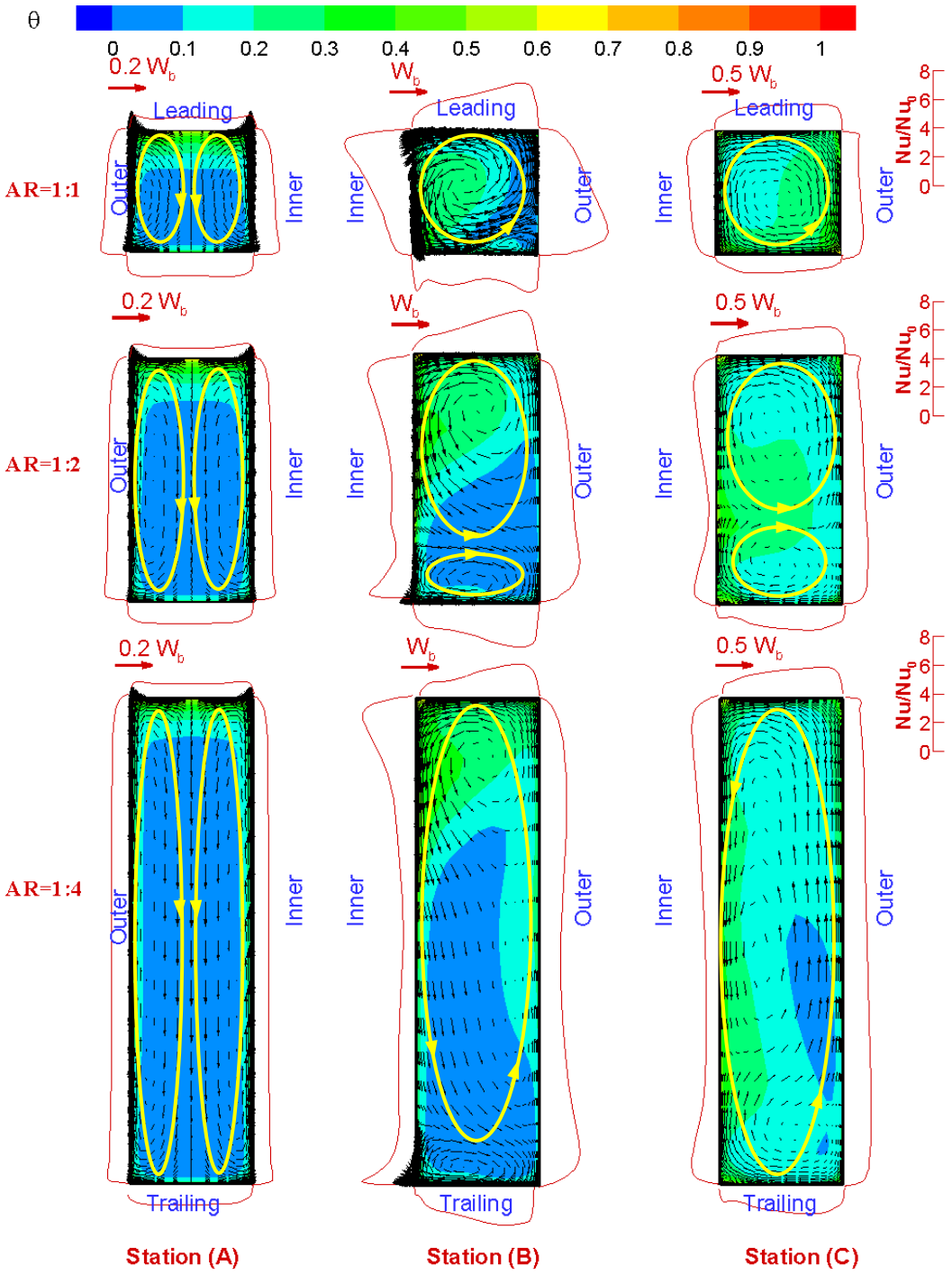

Fig. 5.6 Secondary Flow, Temperature [$\theta=(T-T_i)/(T_w-T_i)$] Contours, and Nusselt Number Ratios for Rotating Ducts (Re=100,000, Ro=0.28, $\Delta\rho/\rho$=0.20)

clearly visible. This suggests that the rotation effect is not strong enough to suppress the bend-induced vortices completely in these high Reynolds number rotating ducts.

5.3 Heat Transfer Coefficient and Friction Factor Distribution

The Nusselt numbers presented here are normalized by the smooth tube correlation by Dittus-Boelter for fully developed, turbulent, non-rotating, tube flow which was defined earlier. Similarly, the friction factors are also normalized by the following smooth tube correlation:

$$Cf_0 = 0.078\, Re^{-0.25} \tag{5-1}$$

Effect of channel aspect ratio and rotation on heat transfer coefficient distribution

Fig. 5.7 shows the Nu/Nuo contour plots on the leading and trailing surfaces of all three channels with different aspect ratios for the rotating and non-rotating cases. For the non-rotating ducts (Cases 1, 3 and 5), three common features are observed in both the square and rectangular channels: 1) In the first passage, the Nusselt number ratio is high near the inlet due to the thin thermal boundary layers; 2) The heat transfer in the bend is high due to the secondary flows induced by the centrifugal forces and the associated pressure gradients. Especially, at the middle part of bend, the heat transfer is high due to the combined effects of flow impingement and bend-induced vortices. Near the end of the bend, the mainstream flow again impinges on the outer wall and produces another high heat transfer region after the second sharp corner; 3) Downstream in the second passage, the heat transfer coefficient decreases and asymptotically approaches the fully developed value. It is noted that the difference of Nusselt number ratios among the three non-rotating ducts are not widely different, except in the bend.

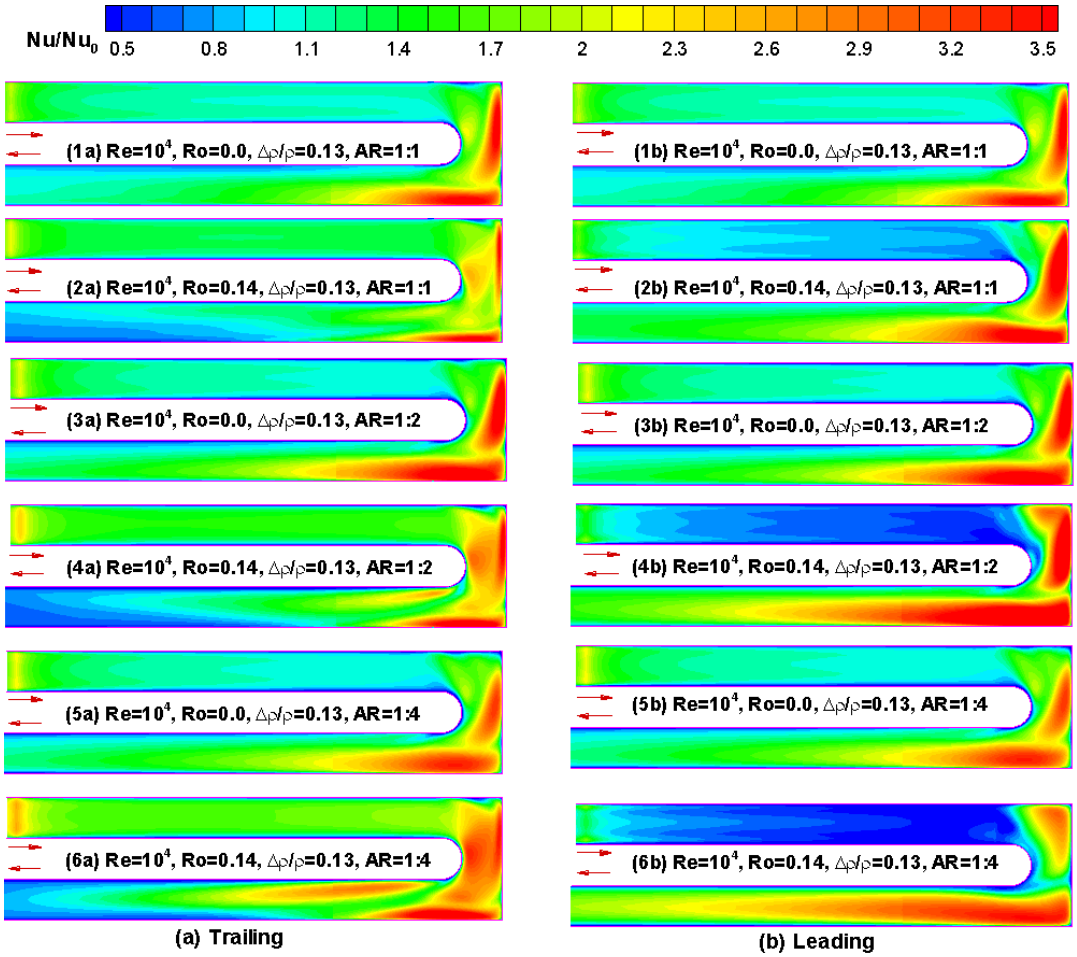

Fig. 5.7 Nusselt Number Ratio Contours on (a) Leading and (b) Trailing Surface for Lower Reynolds Number (Re = 10,000) Cases

For the rotating ducts (Cases 2, 4 and 6), the following common heat transfer characteristics are also observed in all three channels: 1) In the first passage, the Nusselt number ratio on the trailing surface is higher than that on the leading surface. In contrast, in the second passage, the Nusselt number ratio on the leading surface is higher than that on the trailing surface. This agrees well with the analysis of the flow and temperature fields; 2) On the leading surface, the Nusselt number ratio reaches minimum in the middle of the first passage and increases significantly in the bend. In the second passage, the Nusselt number ratio reaches a higher level than that on the same location in non-rotating ducts. For the trailing surface, the Nusselt number ratio increases sharply in the streamwise direction compared with the non-rotating counterpart and reaches a maximum value in the bend region. In the second passage, the Nusselt number ratio decreases gradually along the duct. In general, the observed differences in the Nusselt number ratios among the rotating ducts is more pronounced than those among the non-rotating ducts. This clearly indicated that the channel aspect ratio has a more significant effect on the Nusselt number ratios in rotating ducts although this effect is still small. This can be attributed to the differences in the secondary flow pattern for different aspect ratio ducts.

Fig. 5.8 presents the spanwise-averaged Nusselt number ratios for both the non-rotating Case 5 and the rotating Case 6. Regional averaged (averaged spanwise and over certain S/D_h values) Nusselt number ratios are compared to the experimental data obtained by Fu et al. (2004) for the same cases to validate the numerical results in this study. It is seen that the numerical predictions are in agreement with the experimental

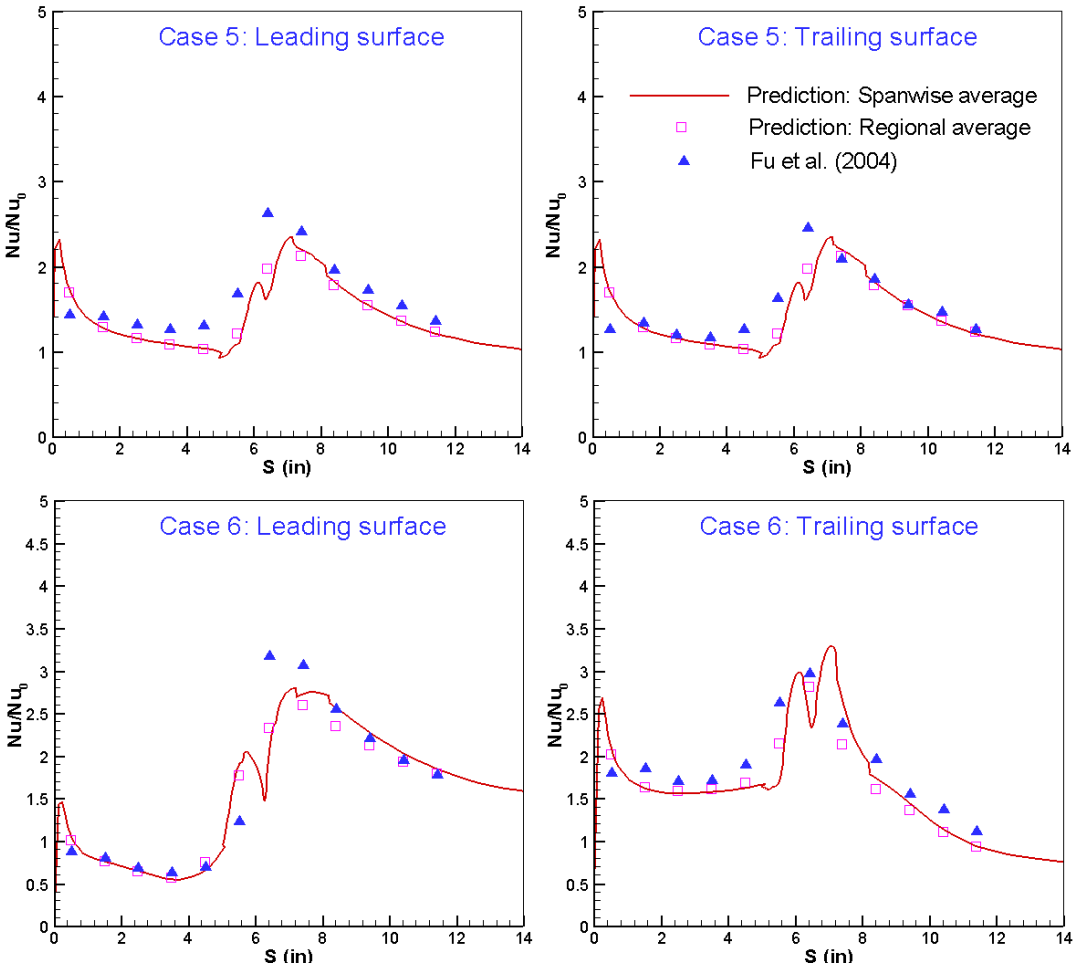

Fig. 5.8 Comparison between Calculated and Measured Nusselt Number Ratios for Non-Rotating and Rotating (Ro=0.14, β = 90°) Ducts (Re=10,000, Δρ/ρ=0.13, AR=1:4)

data except in the bend region. This discrepancy may be due to the fact that the flow conditions and thermal boundary conditions in the measurement are not completely consistent with the idealized condition in numerical prediction.

Fig. 5.9 presents the spanwise-averaged Nusselt number ratios for the rotating ducts (Cases 2, 4 and 6). Referring to the detailed Nusselt number ratio contours (Fig. 5.7), one can see that the spanwise-average Nusselt number ratios on the trailing surface of the first passage and on the leading surface of the second passage were increased by rotation. It is quite clear that the effects of channel aspect ratio become more pronounced under rotating conditions. In the first passage, the Coriolis force pushes colder fluid towards the trailing surface and the rotation-induced vortices brings hotter fluid back to the leading surface. The rotation-induced vortices becomes stronger when the channel aspect ratio is reduced from AR=1:1 to AR=1:4. Consequently, the Nusselt number increases on the trailing surface and reduces on the leading surfaces as the channel aspect ratio reduces. This trend is reversed in the second passage since the Coriolis force acts in the opposite direction after the bend. In the bend region, the Nusselt number ratio on all four surfaces of the AR = 1:2 duct is higher than those observed in the square duct. As the channel aspect ratio was reduced further to AR = 1:4, however, the Nusselt number ratios on the leading and outer surfaces drop sharply since the heat transfer enhancement due to the bend-induced vortices are confined to the leading and trailing surfaces for low aspect ratio ducts.

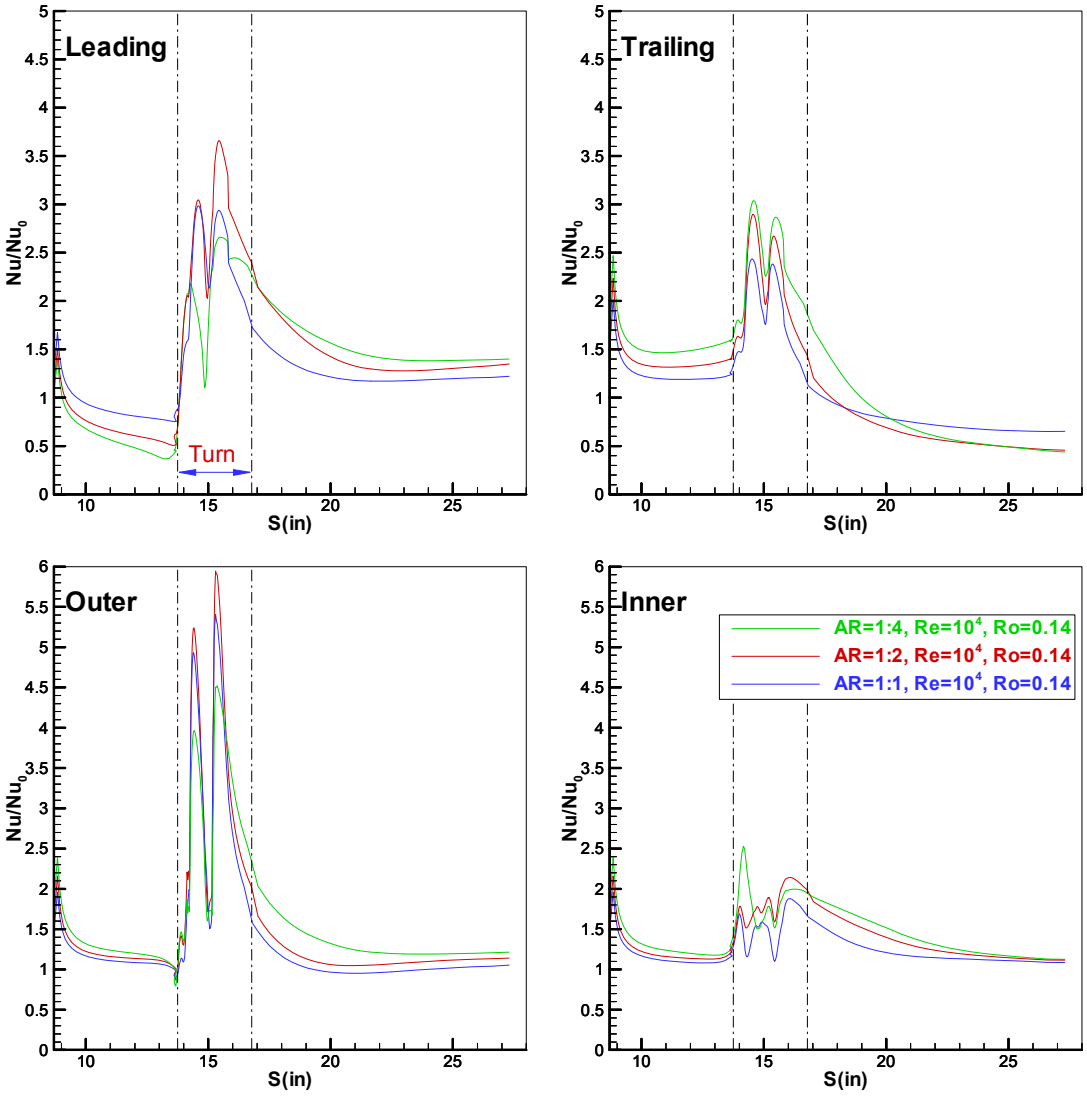

Fig. 5.9 Effect of Channel Aspect Ratio on Spanwise-Averaged Nusselt Number Ratios for Lower Reynolds Number (Ro=0.14, Re=10,000, $\Delta\rho/\rho$=0.13) Cases

Effect of high Reynolds number on heat transfer coefficient distribution

In addition to the non-rotating and rotating ducts with a relatively low Reynolds number presented above (Cases 1-6), calculations were also performed for high Reynolds number, high density ratio, and high rotation number cases (i.e. Cases 7-15) which are closer to power-generation turbine blade cooling conditions. In these calculations, the Reynolds number is increased from 10^4 to 10^5; the rotation number is doubled from 0.14 to 0.28; and the density ratio is increased from 0.13 to 0.4.

Fig. 5.10 shows the detailed Nusselt number ratio contours of the leading and trailing surfaces for high Reynolds number cases. When comparing to the low Reynolds number results shown in Fig. 5.7, it is clearly seen that the Nusselt number ratio decreases in both the non-rotating and rotating ducts when the Reynolds number is increased. In general, the Nusselt number ratios are high on the outer surface of the bend due to flow impingement. Another high heat transfer region was observed after the bend as the flow enters the second passage. For the non-rotating cases (Cases 7, 9 and 11), the effects of channel aspect ratios are relatively small and the Nusselt number ratio contours are very similar among three different aspect ratio ducts.

For the high Reynolds number and high rotation number conditions (Cases 8, 10 and 12), the effects of rotation lead to an increase of the heat transfer on the first pass trailing surface and a decrease of Nusselt number ratios on the first pass leading surface since the Coriolis force induced vortices push the cold fluid toward the trailing surface. The trend is reversed in the second passage as the Coriolis force acts in the opposite direction. Compared to the non-rotating ducts, the effects of channel aspect ratios are

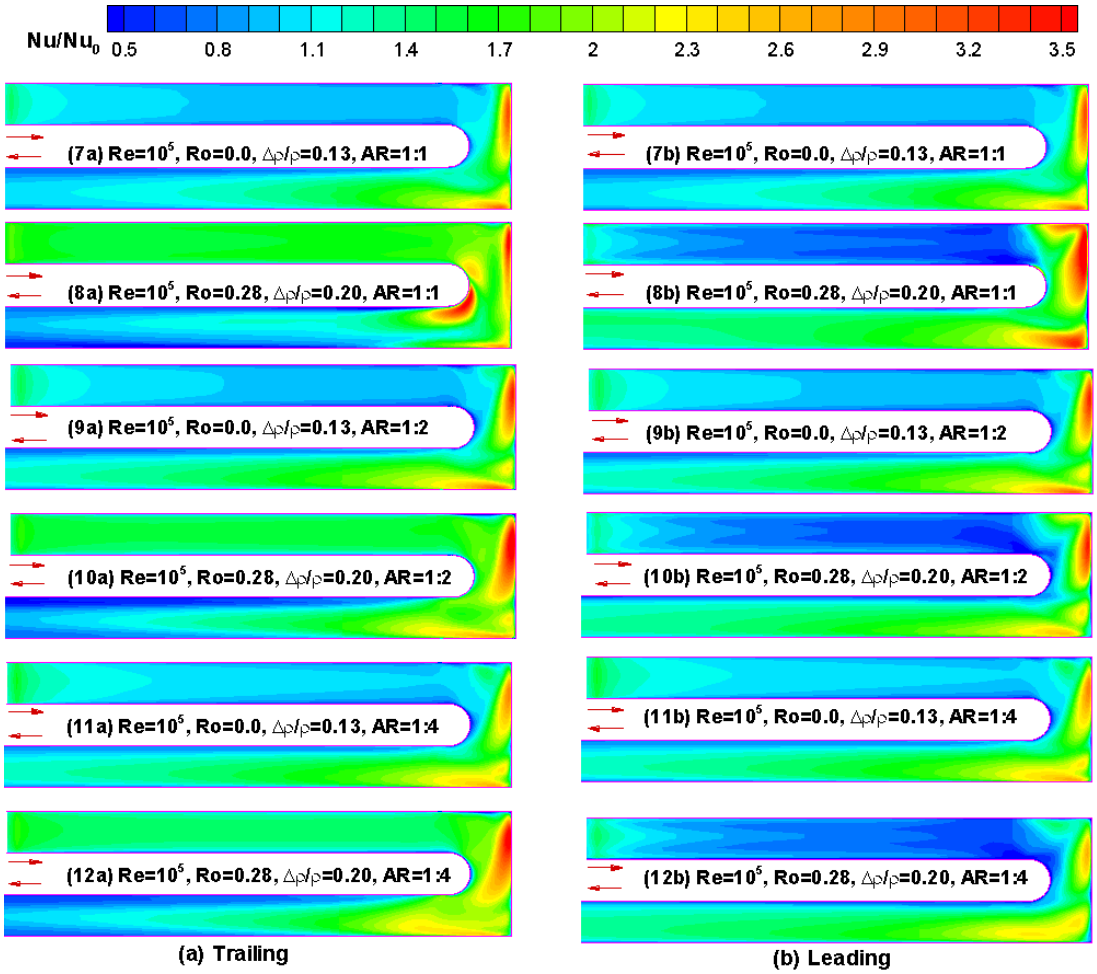

Fig. 5.10 Nusselt Number Ratio Contours on (a) Leading and (b) Trailing Surface for Higher Reynolds Number (Re = 100,000) Cases

more significant in rotating ducts because the size and shape of the secondary flow vortices (see Fig. 5.6) are strongly affected by the channel cross-sectional geometry under rotating conditions.

Fig. 5.11 compares the numerically predicted spanwise-averaged Nusselt number ratio for the non-rotating conditions. It is seen that the AR = 1:2 rectangular duct has the highest Nusselt number ratio (Nu/Nu_o) at the turn region since the counter-rotating vortices are stronger than those observed in either the AR = 1:1 or 1:4 ducts. Near the exit, the Nusselt number ratios (Nu/Nu_o) for all three ducts approach nearly the same value. This confirmed the previous observation that the flow pattern and heat transfer characteristics are not widely different in non-rotating channels with different aspect ratios. It should be noted here, however, the actual heat transfer coefficient (h) is significantly higher for the square duct in comparison with the rectangular ducts since the square duct has the smallest hydraulic diameter and hence the highest mean velocity.

Fig. 5.11 also shows the spanwise-averaged Nusselt number ratios for the non-rotating duct at two different Reynolds numbers of 10,000 and 100,000 for three different aspect ratio channels. In general, the Nusselt number ratios Nu/Nu_0 on the four surfaces decrease as the Reynolds number increases. However, it should be note that Nu_0 increases rapidly (proportional to $Re^{0.8}$) when the Reynolds number was increased from 10,000 to 100,000. Therefore, the actual heat transfer coefficients are still increase very significantly at Re = 100,000 even though the heat transfer enhancement decreases.

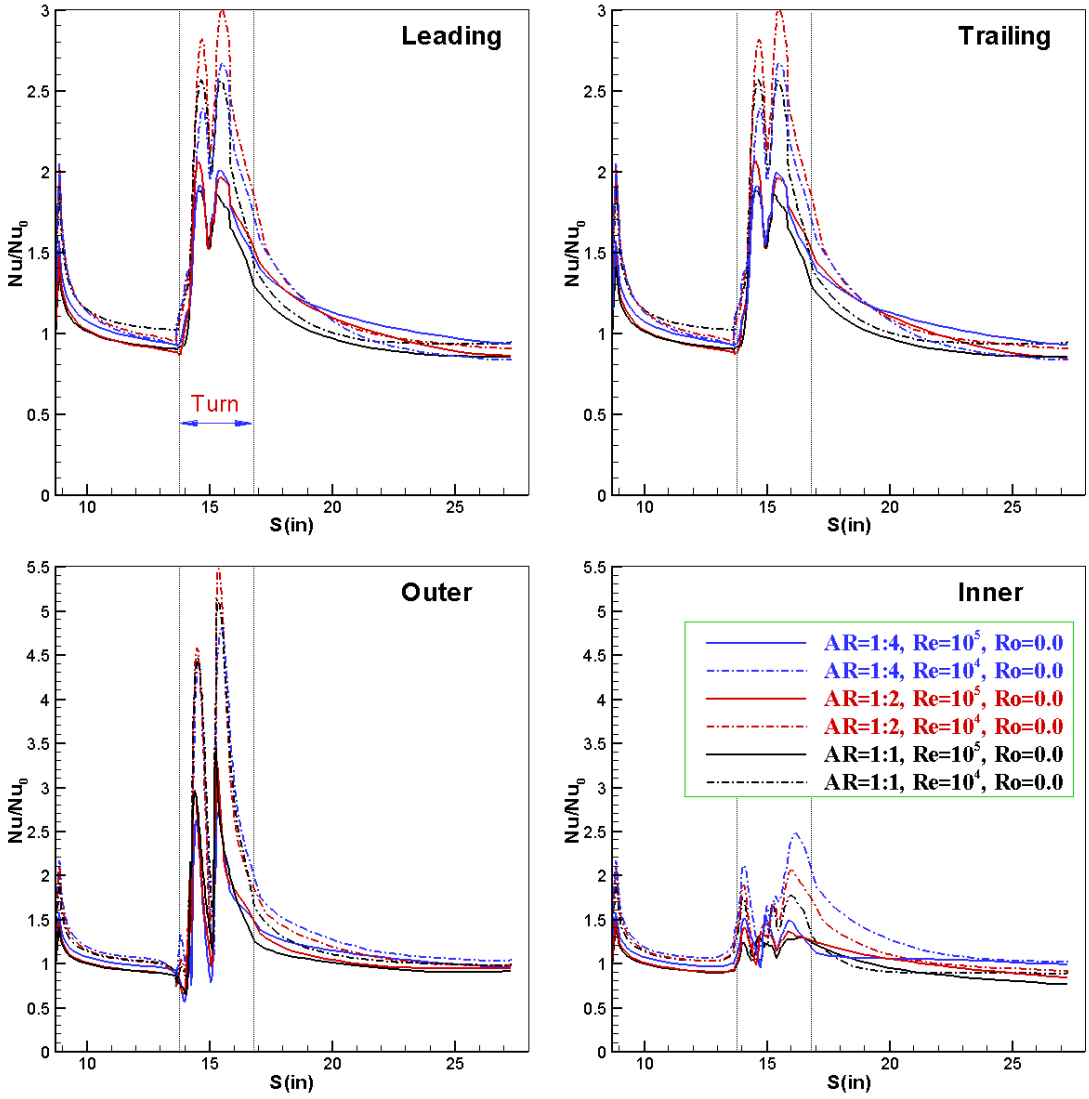

Fig. 5.11 Effect of Reynolds Number on Spanwised-Averaged Nusselt Number Ratios for Non-Rotating Duct with Aspect Ratio of 1:1, 1:2 and 1:4 (Ro=0.0, $\Delta\rho/\rho$=0.13)

Effect of density ratio on heat transfer coefficient distribution

Fig. 5.12 shows the effect of inlet coolant-to-wall density ratio on the spanwise-averaged Nusselt number ratios for the rotating ducts with different aspect ratios. We will focus on the high Reynolds number (Re = 100,000) and high rotation number (Ro = 0.28) conditions with two different density ratios of 0.20 and 0.40. In the first passage of the square ducts (AR = 1:1), an increase in density ratio leads to a large increase of heat transfer on the trailing surface and a fairly significant decrease of Nusselt number ratios on the leading surface. However, the density ratio effect diminishes quickly in the low aspect ratio rectangular ducts of AR = 1:2 and 1:4. In the second passage, an increase in density ratio leads the Nusselt number ratios to decrease on both the leading and trailing surface. Near the exit, however, the effect of density ratio on Nusselt number ratio diminishes for the AR = 1:1 and 1:2 ducts.

Effect of aspect ratio and Reynolds number on spanwise averaged friction factor

Fig. 5.13 shows the spanwise-averaged friction factor ratio C_f/C_{f0} for the heated section of all three non-rotating channels for Re=10,000 and Re=100,000. It is seen that the friction factors for the first passage maintain the fully developed values until a short distance ahead of the bend. Around the inner surface of the bend, the friction factor ratio increase sharply around the bend entrance due to local flow acceleration. Further downstream, the friction factor ratios drop sharply as the flow separates from the inner wall. The friction factor ratios fall below 1 in the separation region and increase again after the reattachment point. On the outer surface of the bend, the friction factor ratios drop significantly around the bend entrance due to the sudden expansion of the channel

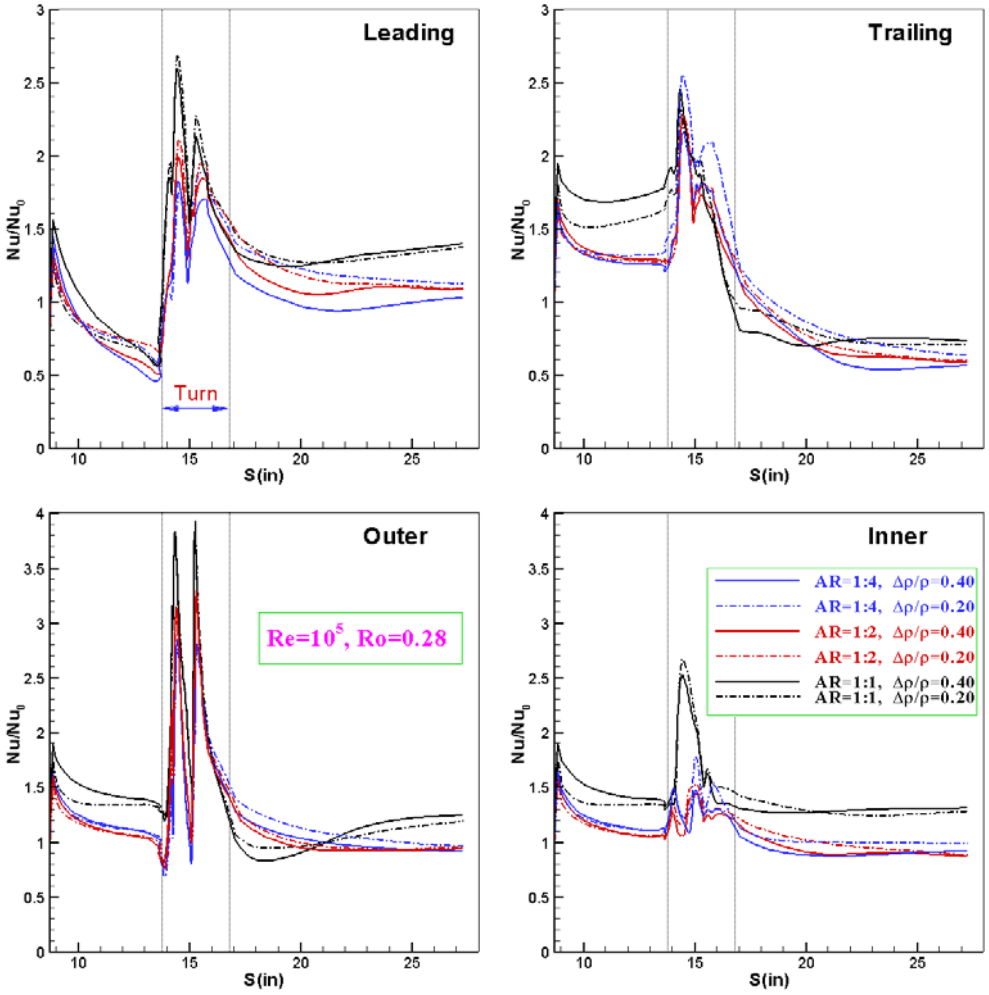

Fig. 5.12 Effect of Density Ratio on Spanwised-Averaged Nusselt Number Ratios for Rotating Duct with Aspect Ratio of 1:1, 1:2 and 1:4 (Re=100,000, Ro=0.28)

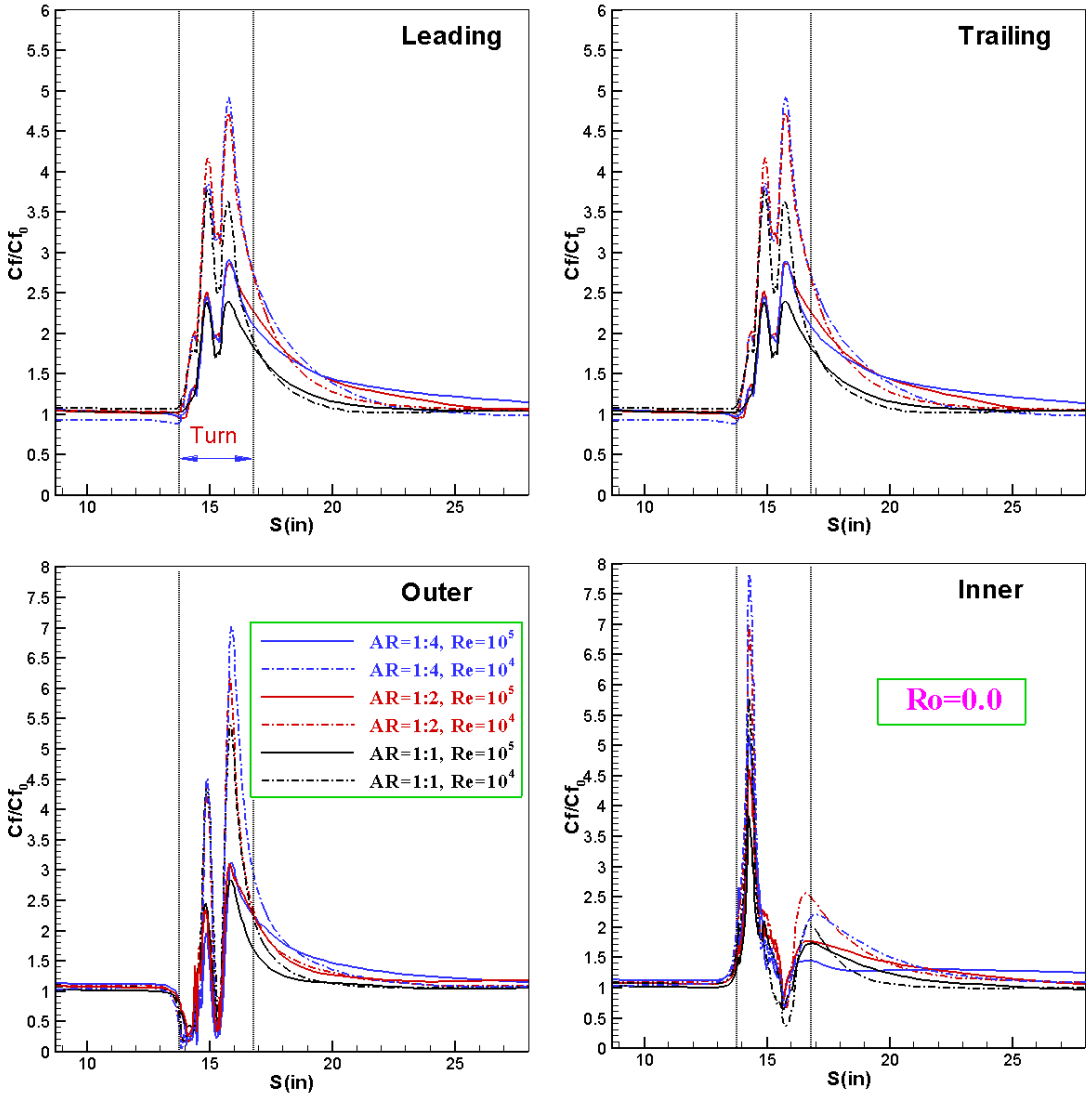

Fig. 5.13 Effect of Reynolds Number on Friction Factor Ratios in Non-Rotating Ducts with Aspect Ratio of 1:1, 1:2 and 1:4 (Ro=0.0, $\Delta\rho/\rho$=0.13)

cross section in the bend region. In the bend, the high momentum is pushed toward the outer surface by the centrifugal force induced by the streamline curvature. This leads to flow impingements on two different locations of the outer surface. The first impingement occurs just behind the shape corner of the first passage, while the second impingement occurs after the second shape corner near the entrance to the second passage. These flow impingements produced two sharp peaks in the bend region as seen in Fig.5.13. It is further noted that the friction factor ratios also increase sharply along the leading and trailing surfaces of the bend. These increases are caused by the Coriolis force induced counter-rotating vortices (see Fig. 5.3) which enhance the mixing of high-momentum fluids in the core region with the low-momentum fluids in the near-wall region. After the bend, the friction factor ratios return gradually their fully developed values in the second passage. In general, the friction factor ratios are somewhat higher for rectangular ducts since the counter-rotating vortices were able to grow into circular shapes and reach full strength.

Fig. 5.13 also shows the effect of the Reynolds number on the spanwise-averaged friction factor ratios for the non-rotating ducts with three different aspect ratios. In the first passage, the friction factor ratio changes only slightly when the Reynolds number was increased from 10,000 to 100,000. However, the actual friction factors are considerably lower for higher Reynolds number cases since Cf_0 is proportional to $Re^{-0.25}$. Around the bend region, the friction factor ratios at Re = 100,000 were about 40-50% lower than the corresponding values at Re = 10,000. After the bend, the friction

factor ratios in all three ducts return gradually to about 1.0 for both the low and high Reynolds number flow conditions.

Effects of rotation on spanwise-averaged friction factor

Fig. 5.14 shows the spanwise-averaged friction factor ratio C_f/C_{f0} on the heated section of all three rotating channels with Ro = 0.14. In the first passage, the Coriolis force pushed the high-momentum fluid toward the trailing surface which creates a thinner boundary layer with increased friction factor ratios on the trailing surface. The same Coriolis force also caused the thickening of the boundary layer and a reduction of the friction factor ratios on the leading surface. In the bend region, the Nusselt number ratios increase on all four walls due to the mixing of high and low momentum fluids, the flow impingement on the outer surface, and the boundary layer flow reattachment on the inner surface. After the bend, the Coriolis force in the second passage acts in the opposite direction of that observed in the first passage. Consequently, the friction factor increases on the leading surface and decreases on the trailing surface as the fluid moves radially inward in the second passage. It is also observed that the effect of the channel aspect ratio on the friction factor is significant on the leading surfaces and side walls of the second passage of the rotating ducts.

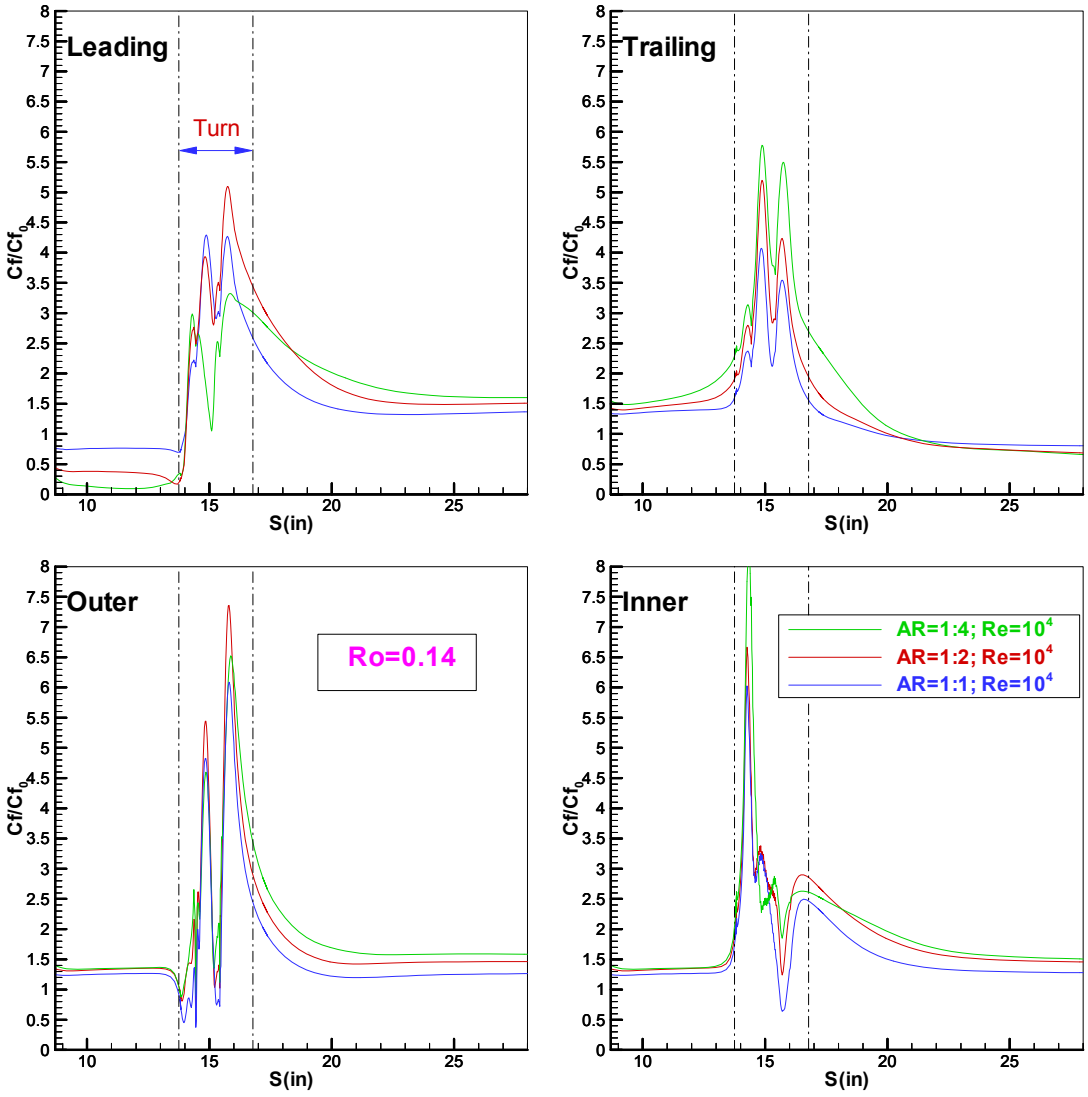

Fig. 5.14 Effect of Rotation on Friction Factor Ratios for Rotating Ducts with Lower Reynolds Number Cases (Ro=0.14, Re=10,000, $\Delta\rho/\rho$=0.13)

CHAPTER VI

TRANSFER IN TWO-PASS ROTATING RECTANGULAR CHANNELS (AR=1:1, AR=1:2, AR=1:4) WITH 45-DEG ANGLED RIBS

In this chapter, we present calculations for rotating/non-rotating two pass rectangular channels (AR=1:1, 1:2, and 1:4) with ribbed wall using the near wall second-order Reynolds stress closure model.

6.1 Description of Problem

A schematic diagram of the geometry for AR=1:4 duct is shown in Fig. 6.1. As mentioned earlier, this investigation covers three channels with different aspect ratios (AR = 1:1, AR = 1:2 and AR = 1:4). For the sake of brevity, however, only the geometry for the AR = 1:4 channel is given in Fig. 6.1. All three ducts have the same length, same bend radius, and the same width between the inner and outer wall. Of the four side walls, the two in the rotational direction are denoted as leading and trailing surfaces, while the other two are denoted as inner and outer surfaces. The total length of the channel, L, equals to 37.47cm (14.75 in), the distance from the inlet of the channel to the axis of rotation is given by R_r = 40.64cm (16 in). The channel consists of an unheated smooth starting section (L_1 = 22.23cm (8.75 in)) and a heated section (15.24cm (6 in)). The radius of curvature of the 180° sharp turn is r_i = 0.635 cm (0.25 in) and the minimum gap G between the inner and outer surfaces of the bend is 1.27 cm (0.5 in). The channel width W is kept the same at 1.27 cm (0.5 in) for all three different aspect ratio channels. The channel height is increased from 1.27 cm (0.5 in) for square duct to

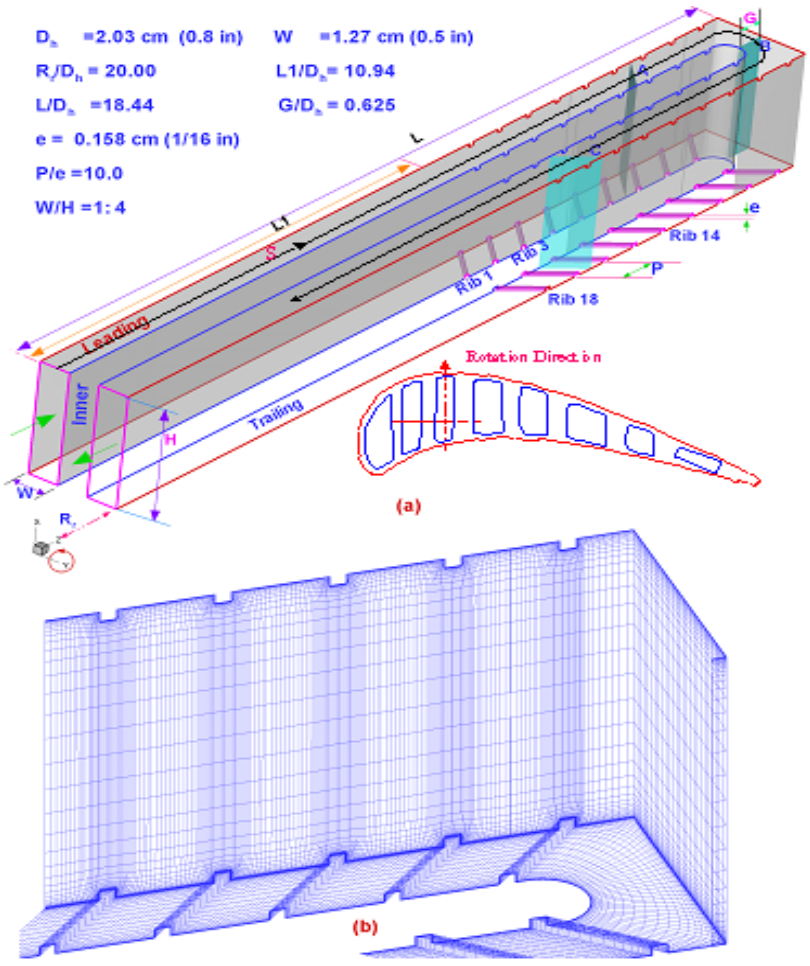

Fig. 6.1 Geometry and Conceptual View of Rotating Channel Orientation for Rectangular Duct (AR=1:4) with Angle Ribs and Numerical Grid

5.08 cm (2.0 in) for AR =W/H = 1:4 channel. It should be noted that the hydraulic diameters D_h are different for different aspect ratio channels with D_h = 1.27 cm, 1.69 cm, and 2.03 cm for AR = 1:1, 2:1, and 4:1 channels, respectively. The leading and trailing surfaces are roughened by nine equally-spaced 45° ribs with square cross section. The ribs are parallel (inline on leading and trailing surfaces) and point upstream. The rib height is fixed at 0.158 cm (0.0625 in) and the rib-pitch-to-height ratio (P/e) is 10, but the rib height-to-hydraulic diameter ratios (e/D_h) are 0.125, 0.094, and 0.078, for AR=1:1, AR=1:2, and AR=1:4 channel, respectively. For the rotating cases, the channel orientations is given as $\beta = 90°$. A summary of all fifteen (15) cases studied is given in Table 6.1. It should be remarked here that the square duct has the highest inlet velocity and highest rotating speed under the same Reynolds number and same rotation number conditions since it has the smallest hydraulic diameter among the three ducts considered.

Computational grid details

Fig. 6.1(b) shows the computational grid for the rectangular duct with AR = 1:4. For the sake of brevity, the numerical grids for AR = 1:1 and AR = 1:2 channel are not included here. Systematic grid-refinement studies were performed for all three channels for Re = 10,000 cases. The grid refinement in the axial direction at the bend region has produced only minor changes of Nusselt number ratio. The refinement of cross sectional grids resulted in a maximum improvement of 3.1% in Nusselt number ratios. The minimum grid spacing for the Re = 100,000 cases is maintained at 2×10^{-5} of the hydraulic diameter which corresponds to wall coordinate y^+ on the order of 0.1 also. The grid-refinement study for all three channels at this Reynolds number was also performed.

Table 6.1: Summary of cases studied for two-pass ducts with ribs

Case #	**AR**	β	**Re**	**Ro**	$\Delta\rho/\rho$
Case1	1:1	-	10,000	0.0	0.13
Case2	1:1	90^0	10,000	0.14	0.13
Case3	1:2	-	10,000	0.0	0.13
Case4	1:2	90^0	10,000	0.14	0.13
Case5	1:4	-	10,000	0.0.0	0.13
Case6	1:4	90^0	10,000	0.14	0.13
Case7	1:1	-	100,000	0.0	0.13
Case8	1:1	90^0	100,000	0.28	0.20
Case9	1:2	-	100,000	0.0	0.13
Case10	1:2	90^0	100,000	0.28	0.20
Case11	1:4	-	100,000	0.0.0	0.13
Case12	1:4	90^0	100,000	0.28	0.20
Case13	1:1	90^0	100,000	0.28	0.40
Case14	1:2	90^0	100,000	0.28	0.40
Case15	1:4	90^0	100,000	0.28	0.40

The results indicate that the refinement in the axial direction at the bend region produced only minor changes of Nusselt number ratio, while the refinement of cross sectional grids caused a maximum of 2.8 % improvement at the bend region in Nusselt number ratios. In all calculations, the root-mean-square (rms) and maximum absolute errors for both the mean flow and turbulence quantities were monitored for each computational block to ensure complete convergence of the numerical solutions and a convergence criterion of 10^{-5} was used for the maximum rms error.

Results and discussion

This section presents the three-dimensional mean flow, the temperature field and the Nusselt number ratios for the ducts with three different aspect ratios of AR = 1:1, AR = 1:2, and AR = 1:4, respectively. The Nusselt numbers presented here are normalized with a smooth tube correlation by Dittus-Boelter for fully developed turbulent non-rotating tube flow.

6.2 Velocity and Temperature Fields

Fig.6.2 shows the dimensionless temperature contour (θ) and the vector field for Re = 10,000 cases at three axial stations A, B, and C as denoted in Fig. 6.1. The station A of Fig.6.2 is viewed from the inlet, while the stations B and C of Fig. 6.2 are viewed from the outlet. In order to view the secondary flow in station (B), the velocity vector is scaled as half of the original velocity. Moreover**,** the Nusselt number ratios on all four walls are shown in Fig. 6.2 to facilitate a detailed understanding of the heat transfer characteristics in different aspect ratio channels.

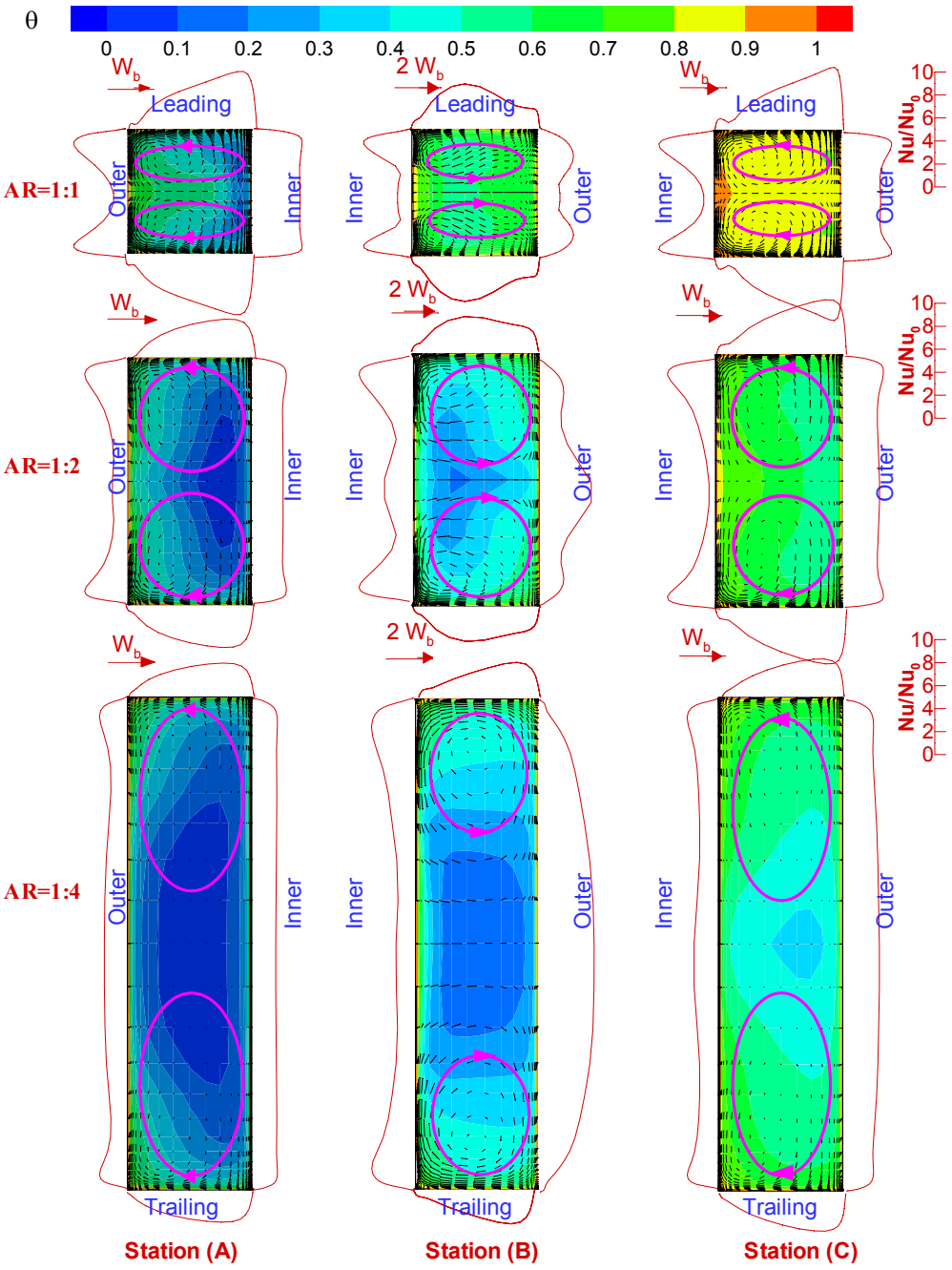

Fig. 6.2 Secondary Flow, Temperature [$\theta=(T-T_i)/(T_w-T_i)$] Contours, and Nusselt Number Ratios for Non- Rotating Ducts (Re=10,000, $\Delta\rho/\rho=0.13$)

For the three non-rotating ducts, as the fluid approaches the rib, the rib-induced fast secondary flow moves towards the outer surface and returns back to the inner surface along the centerline of the inclined cross-stream plane, two symmetric counter-rotating vortices are generated in the first passage for all three channels. Upon entering the turn, the curvature-induced secondary flow (which pushes fluid from the inner to outer surface) is combined with the existing secondary flow induced by the ribs, that complicates secondary flow pattern and its effect is reflected by temperature contour in the turn region (Fig. 6.2). In the second passage the rib-induced flow is reversed in direction due to the opposite rib angle compared to the first passage. Here, the rib-induced secondary flow moves from the outer to the inner surfaces and returns back to the outer surface along the centerline of the inclined cross-stream plane. As a result, two symmetric counter-rotating vortices are formed in the second passage for all three channels.

It is noted that the secondary flows at station (**A**) of the first passage and station (**C**) of the second passage are dominated by rib-induced vortices. These vortices expand in the vertical direction as the channel height was decreased from AR = 1:1 to AR = 1:4. However, the strengths of the rib-induced vortices become weaker in the lower aspect ratio channels. As noted earlier, the hydraulic diameter increases in lower aspect ratio channels since the channel height increases while the channel width and rib dimensions remain the same. Consequently, the rib height-to-hydraulic-diameter ratios (e/D_h) are smaller in the lower aspect channels. Furthermore, the inlet velocities in AR = 1:2 and AR = 1:4 ducts are also reduced to only 75% and 62.5%, respectively, of that in the

square (AR = 1:1) channel under the same Reynolds number condition. The combined effects of lower inlet velocity and smaller e/D_h have led to a significant drop of the Nusselt number ratios on the ribbed surfaces as the channel aspect ratio decreases.

It is further noted in Fig. 6.2 that there are distinct differences in the secondary flow patterns at station (B) in the turn region for different aspect ratio ducts. As mentioned earlier, the secondary flow development in the bend region can be attributed to the combined effects of the existing secondary flow induced by the ribs and the curvature-induced secondary flow. The secondary flow induced by the 180° turn tends to maintain circular shapes up to the space limitations rather than expanding continuous in the vertical direction. For the AR = 1:1 channel, the bend-induced vortices were squashed in the vertical direction due to the tight spacing between the leading and trailing surfaces. As the channel aspect ratio decreases to AR = 1:2, the bend-induced vortices become fully circular and occupy the entire channel. However, the curvature-induced vortices ceased to expand in the vertical direction when the channel height was further increased to AR = 1:4. In general, the strongest heat transfer enhancement is observed in the AR = 1:2 channel since the bend-induced vortices are nearly circular and occupy the entire channel cross section. It is also worthwhile to note that the bend-induced vortices are significantly stronger than the rib-induced vortices in the bend region, but the effect diminishes gradually in the second pass.

Fig. 6.3 shows the cross-stream velocity vectors and the temperature contours for the Re = 10,000 rotating ducts at the same location as those presented in Fig. 6.2. It is clear that the flow patterns in both the first and second passages were significantly

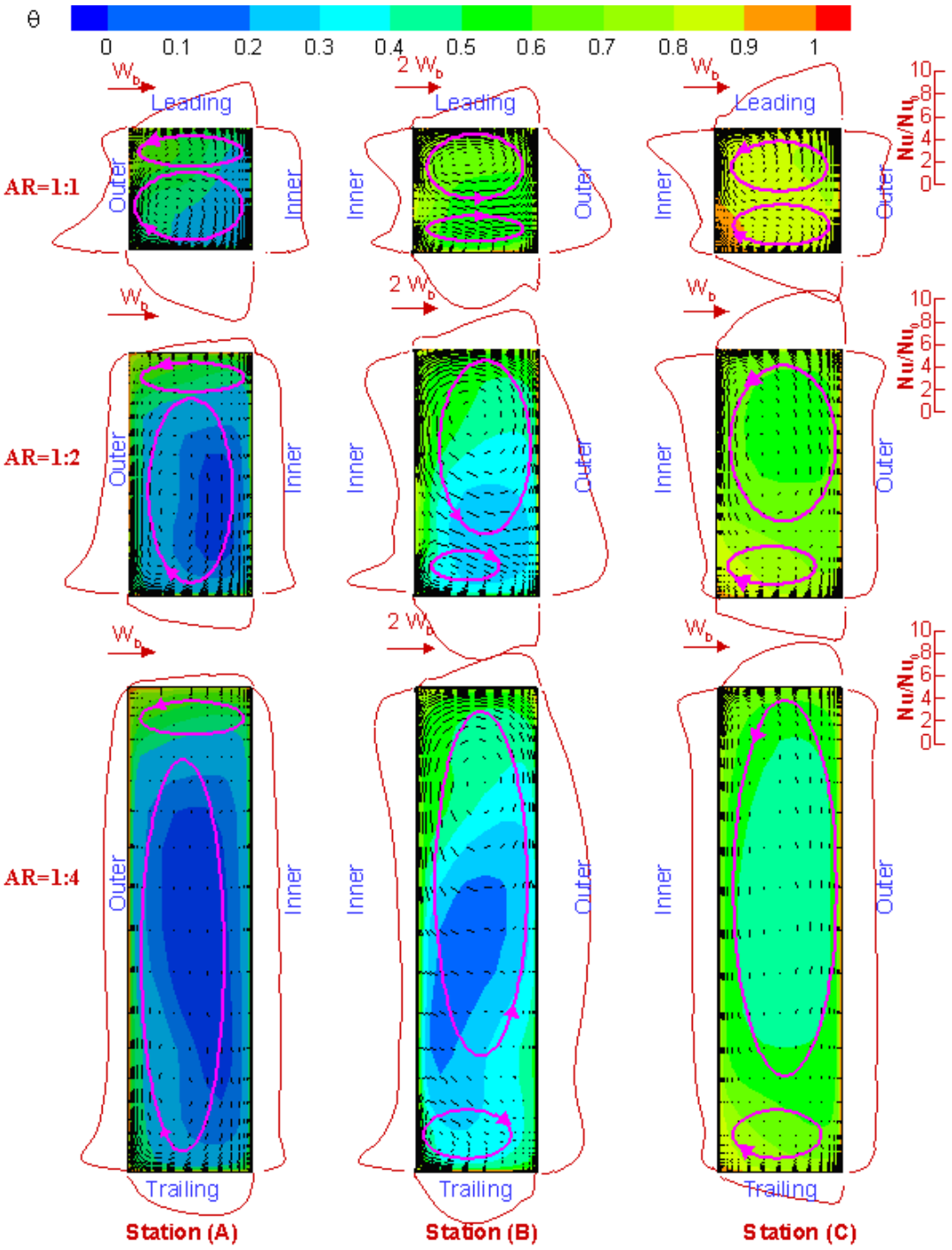

Fig. 6.3 Secondary Flow, Temperature [$\theta=(T-T_i)/(T_w-T_i)$] Contours, and Nusselt Number Ratios for Rotating Ducts (Re=10,000, Ro=0.14, $\Delta\rho/\rho=0.13$)

modified by the rotation-induced vortices. In the first passage, the Coriolis forces produce a pair of counter-rotating vortices which moves cooler fluids in the core region toward the trailing surface of the rotating ducts. Comparing to the non-rotating cases shown in Fig. 6.2, it is clearly seen that the symmetric vortices induced by the inclined ribs were significantly modified by the channel rotation. In the first passage at station (**A**), the rib-induced vortex near the trailing surface was expanded to occupy a large part of the channel, while the vortex near the leading surface was strongly suppressed. In the second passage, the Coriolis force acts in the opposite direction, which pushes the cold fluid toward the leading surface, consequently the vortex induced by the rib near the leading surface was enlarged and the vortex near the trailing surface was reduced. In the bend region, the rotation- and rib-induced vortices in the first passage were combined with the much stronger bend-induced vortices to form a large vortex near the leading surface and a smaller vortex adjacent to the trailing surface as seen in Fig. 6.3(B). The combination of these vortices influences the heat transfer characteristics which will be presented in the next section.

Fig. 6.4 shows the velocity vectors and temperature contours for non-rotating ducts for the high Reynolds number (Re=100,000) cases. Comparing Fig. 6.4 with Fig. 6.2 for the non-rotating ducts, the overall secondary flow patterns are quite similar between the low and high Reynolds number cases, but the vortices are somewhat stronger at Re = 100,000 since the inflow velocity is increased and the thermal boundary layer becomes thinner at higher Reynolds number.

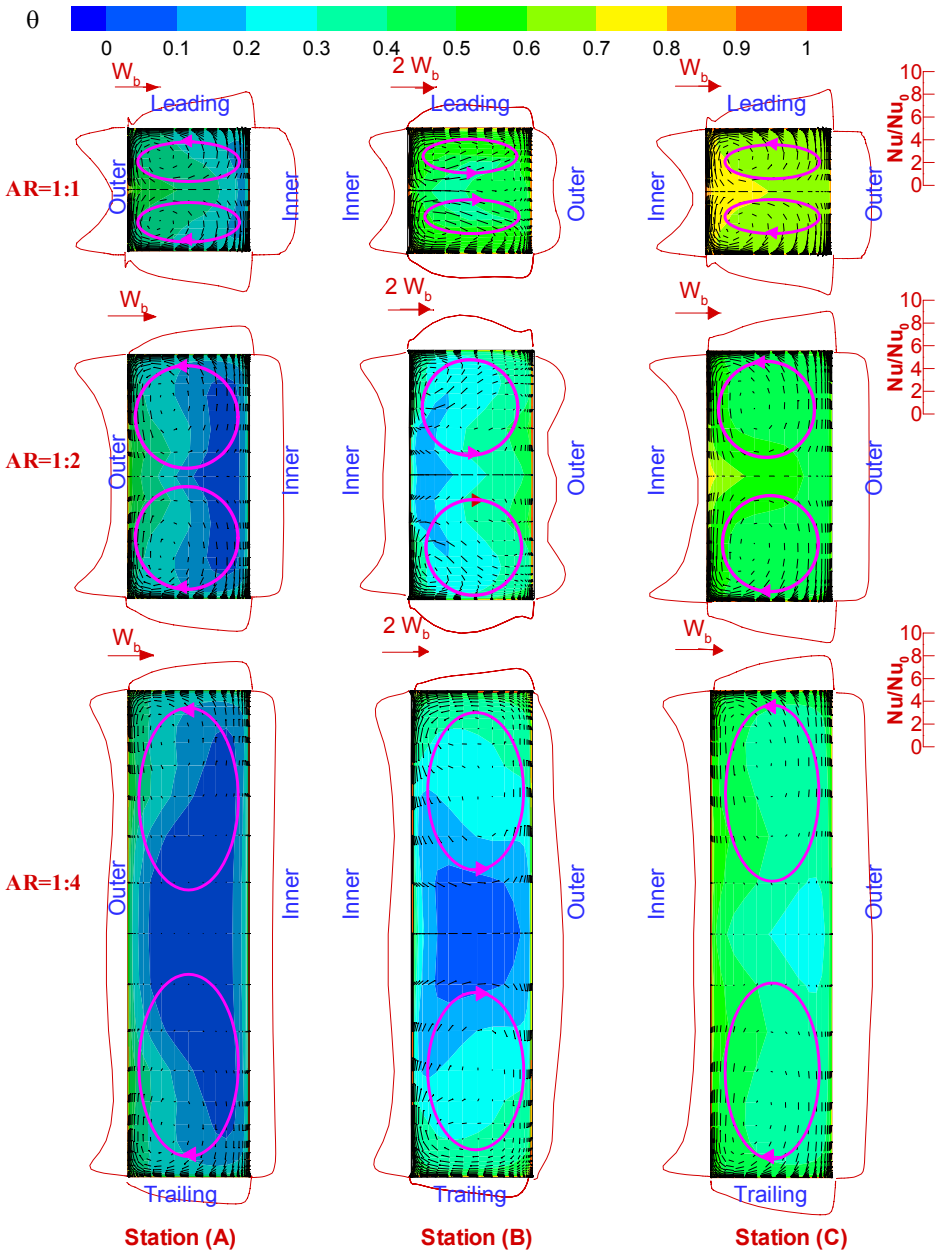

Fig. 6.4 Secondary Flow, Temperature [$\theta=(T-T_i)/(T_w-T_i)$] Contours, and Nusselt Number Ratios for Non- Rotating Ducts (Re=100,000, $\Delta\rho/\rho=0.13$)

Fig. 6.5 shows the effects of high Reynolds number (Re = 100,000) and high rotation number (Ro = 0.28) on the temperature contours and secondary flow vectors. Comparing to the low-Re and low-Ro cases shown in Fig. 6.3, it is clearly seen that the rotation-induced vortices become stronger when both the Reynolds number and rotation number were increased. In the first passage of the AR=1:4 channel, the vortex induced by rotation overpowered the vortex induced by the ribs. In the bend region, however, the vortices induced by the turn were also strengthened as the Reynolds number was increased from Re = 10,000 to Re = 100,000. The secondary vortices induced by the ribs and rotations were combined with those generated by the 180° turn to form a larger vortex near the leading surface. However, the Coriolis forces distorted the secondary flows more dramatically in comparison with those observed in Fig. 6.3 as the rotation number was doubled from 0.14 to 0.28. The rotation effect is particularly evident for the square (AR = 1:1) channel where two rotation-induced vortices are clearly visible near the trailing surface. In the second passage, the Coriolis force acts in the opposite direction while the turn-induced vortices diminish gradually. In general, the secondary flow patterns at station (**C**) are similar to those shown in Fig. 6.3 for lower Reynolds number and lower rotation number cases.

6.3 Heat Transfer Coefficient Distribution

The Nusselt numbers presented here are normalized by the smooth tube correlation.

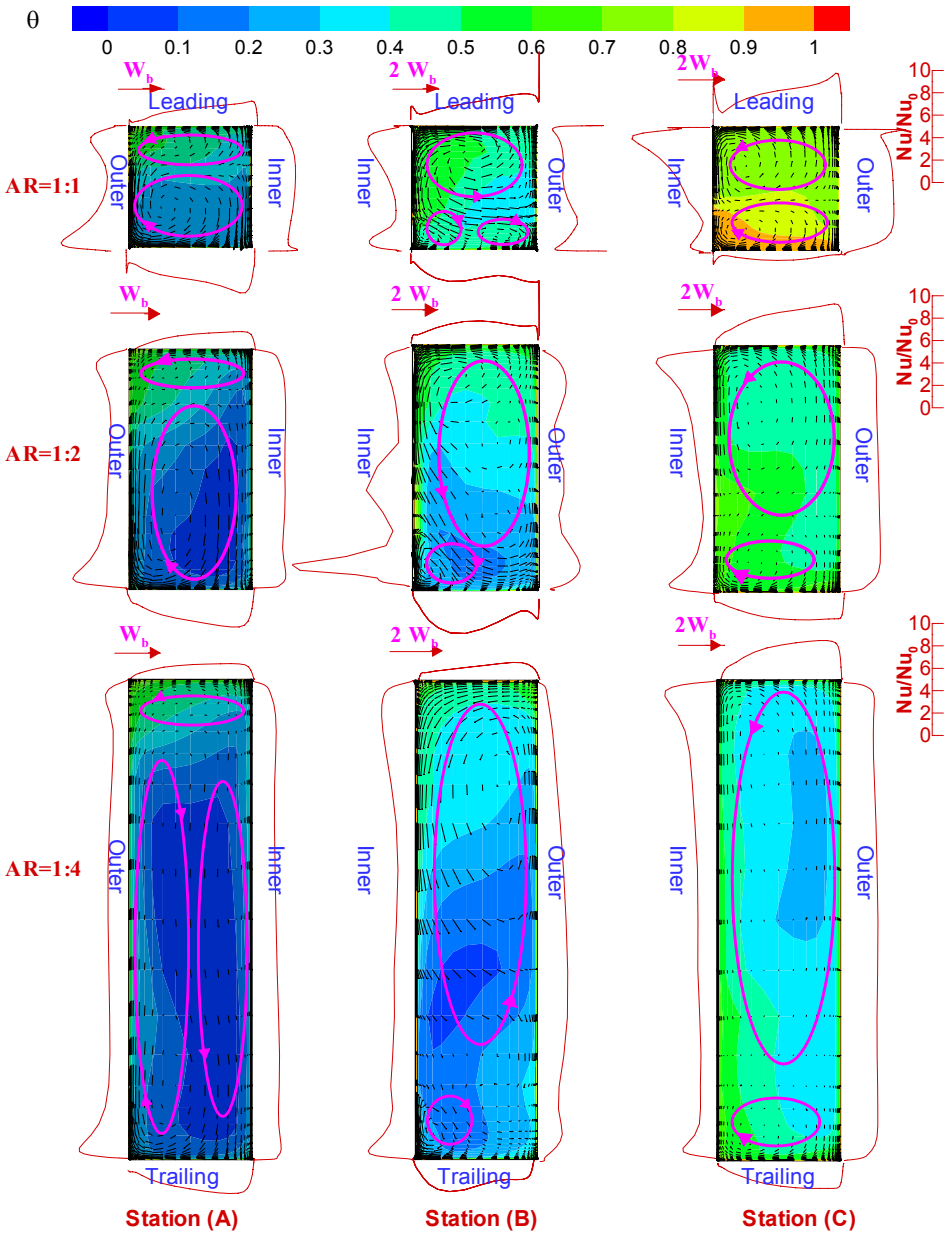

Fig. 6.5 Secondary Flow, Temperature [$\theta=(T-T_i)/(T_w-T_i)$] Contours, and Nusselt Number Ratios for Rotating Ducts (Re=100,000, Ro=0.28, $\Delta\rho/\rho=0.20$)

Effect of channel aspect ratio and rotation on heat transfer coefficient distribution

Fig. 6.6 shows the Nu/Nuo contour plots on the leading and trailing surfaces of all three channels with different aspect ratios for the rotating and non-rotating cases. For the non-rotating ducts (Cases 1, 3 and 5), the entrance and exit regions were cut off to focus on the ribbed heated section, three common features are observed in both the square and rectangular channels: 1) The highest Nusselt number ratios are located near the top of the ribs, while lowest Nusselt number ratios are located right before and after the ribs for the first and second passages. Between any two opposite ribs in the first passage, the Nusselt number ratios are highest near the inner wall and decrease as the fluid moves towards the outer wall. This is due to the rib-induced secondary flow moving from the inner wall to the outer wall as shown in Fig. 6.2**.** Moreover, the Nusselt number ratios between the ribs increased gradually along the first passage until the flow approaches the seventh rib, where it decreases gradually until the ninth rib. 2) The Nusselt number ratios in the turn are high due to the combined effects of the flow impingement and the turn-induced vortices. 3) In the second passage (between any two opposite ribs), the Nusselt number ratios are higher near the outer surface and decrease as we move toward the inner surface. Again, this is a result of the rib-induced secondary flow in the second passage as shown earlier in Fig. 6.2.

As noted earlier, the heat transfer characteristics in non-rotating channels are affected by the secondary flows induced by the ribs and the 180° turn. In the first passage, the Nusselt number ratios in the square duct are higher than those in the lower aspect ratio ducts since the square duct has the highest inlet velocity and largest e/D_h

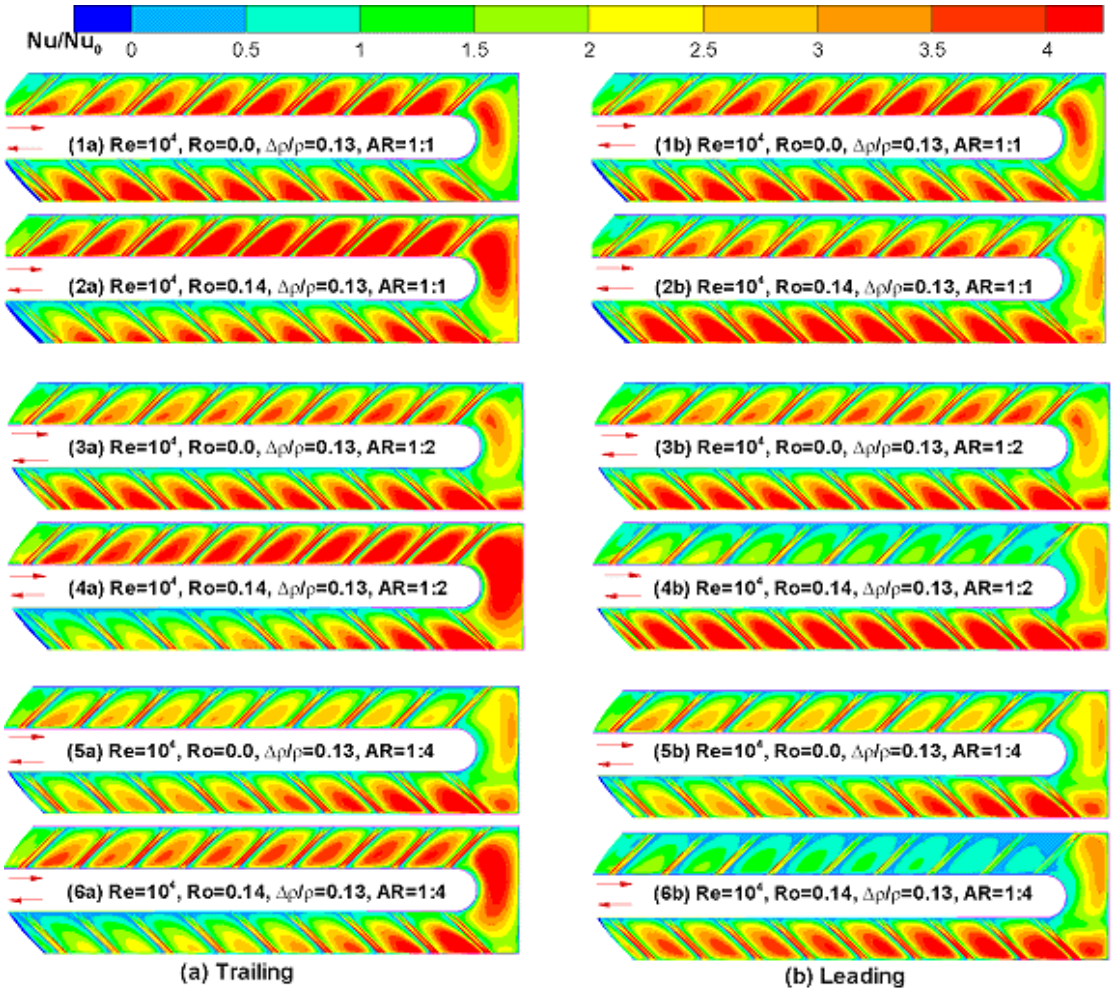

Fig. 6.6 Nusselt Number Ratio Contours on (a) Leading and (b) Trailing Surface for Lower Reynolds Number (Re = 10,000) Cases

among the three ducts at the same Reynolds number. In the second passage, however, the highest Nusselt number ratios were observed in the AR = 1:2 channel since the rotation-induced vortices are stronger than those generated by either the AR = 1:1 or AR = 1:4 ducts as noted in earlier discussions.

For the rotating ducts (Cases 2, 4 and 6), the following common heat transfer characteristics are also observed in all three channels: 1) In the first passage, the Nusselt number ratio on the trailing surface is higher than that on the leading surface. In contrast, in the second passage, the Nusselt number ratio on the leading surface is higher than that on the trailing surface. This agrees well with the analysis of the flow and temperature fields; 2) The Nusselt number in the bend is much higher on the trailing surface for all three channels when compared to the non-rotating case, also much higher than that on the leading surface.

In rotating channels, the Nusselt number ratios decrease on both the leading and trailing surfaces as the channel aspect ratio was reduced from AR = 1:1 to 1:2 and 1:4. This can be attributed to the fact that the inlet velocity and e/D_h are smaller in lower aspect ratio ducts for the same Reynolds number. In the bend region and immediately downstream of the bend, however, the highest Nusselt number ratios were observed in the AR = 1:2 duct when the turn-induced vortices are nearly circular and occupy the entire channel cross section.

Fig. 6.7 compares the numerically predicted spanwise-averaged Nusselt number ratios among Cases 1, 3 and 5 for the non-rotating conditions, the Nusselt number ratios around rib 6 and rib 16 are enlarged in Fig. 6.7 in order to be viewed clearly. For three

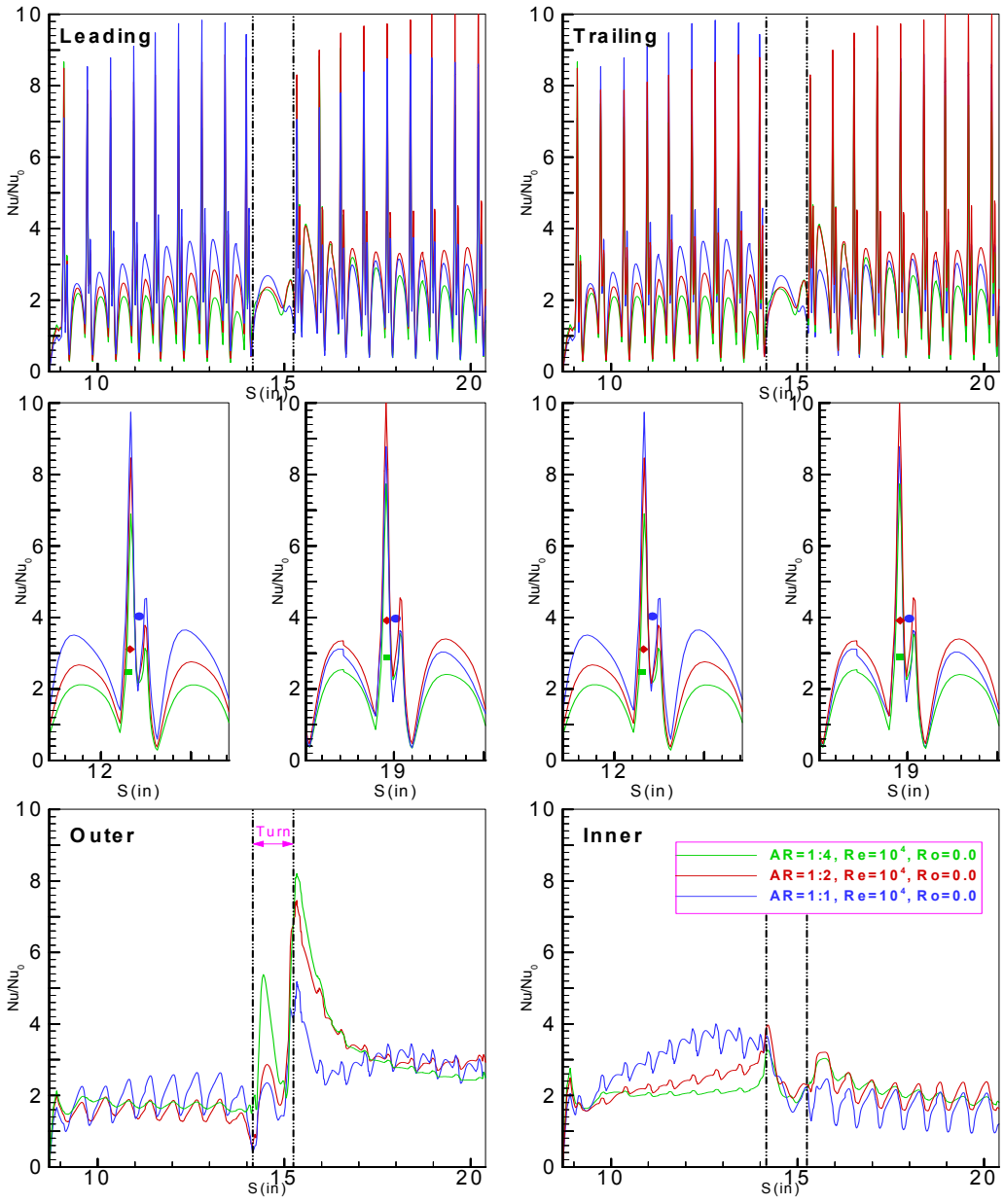

Fig. 6.7 Effect of Channel Aspect Ratio on Spanwise-Averaged Nusselt Number Ratios for Lower Reynolds Number (Ro=0.00, Re=10,000, $\Delta\rho/\rho$=0.13) Cases

channels, the spanwise-averaged Nusselt number distributions on the leading and trailing surfaces show periodic spikes. The higher spikes are caused by the flow impingement on the ribs, and the lower spikes are caused by the flow reattachment between the ribs. The Nusselt number ratios are lower just upstream and downstream of the ribs and higher in the regions between the ribs. In the first passage, the Nusselt number ratios decrease as the channel aspect ratios were reduced from AR = 1:1 to 1:4. The highest heat transfer enhancement was observed in the square duct since it has the smallest hydraulic diameter and hence the highest mean velocity and largest e/D_h under the same Reynolds number conditions. In the second passage, the highest Nusselt number ratios were obtained in the AR = 1:2 duct since the bend-induced secondary flow reaches maximum strength when the vortices are nearly circular and occupy the entire channel as shown earlier in Fig. 6.2.

The comparision between the numerical prediction and measured regional average is not present here since the prediction can not agree well with the experimental data. After the hard-time of investagation, the author think several reasons result in this unprediction, one is the current turbulence model is not prefert, especially the energy equation still has room to improve the accuracy of prediction, the second is the boundary condiction is impossible to consist with the experimental condition.

Fig. 6.8 presents the spanwise-averaged Nusselt number ratios for the rotating ducts (Cases 2, 4 and 6). Also the Nusselt number ratios around rib 6 and rib 16 are enlarged in Fig. 6.8. Referring to the detailed Nusselt number ratio contours (Fig. 6.6), one can see that the spanwise-averaged Nusselt number ratios on the trailing surface of

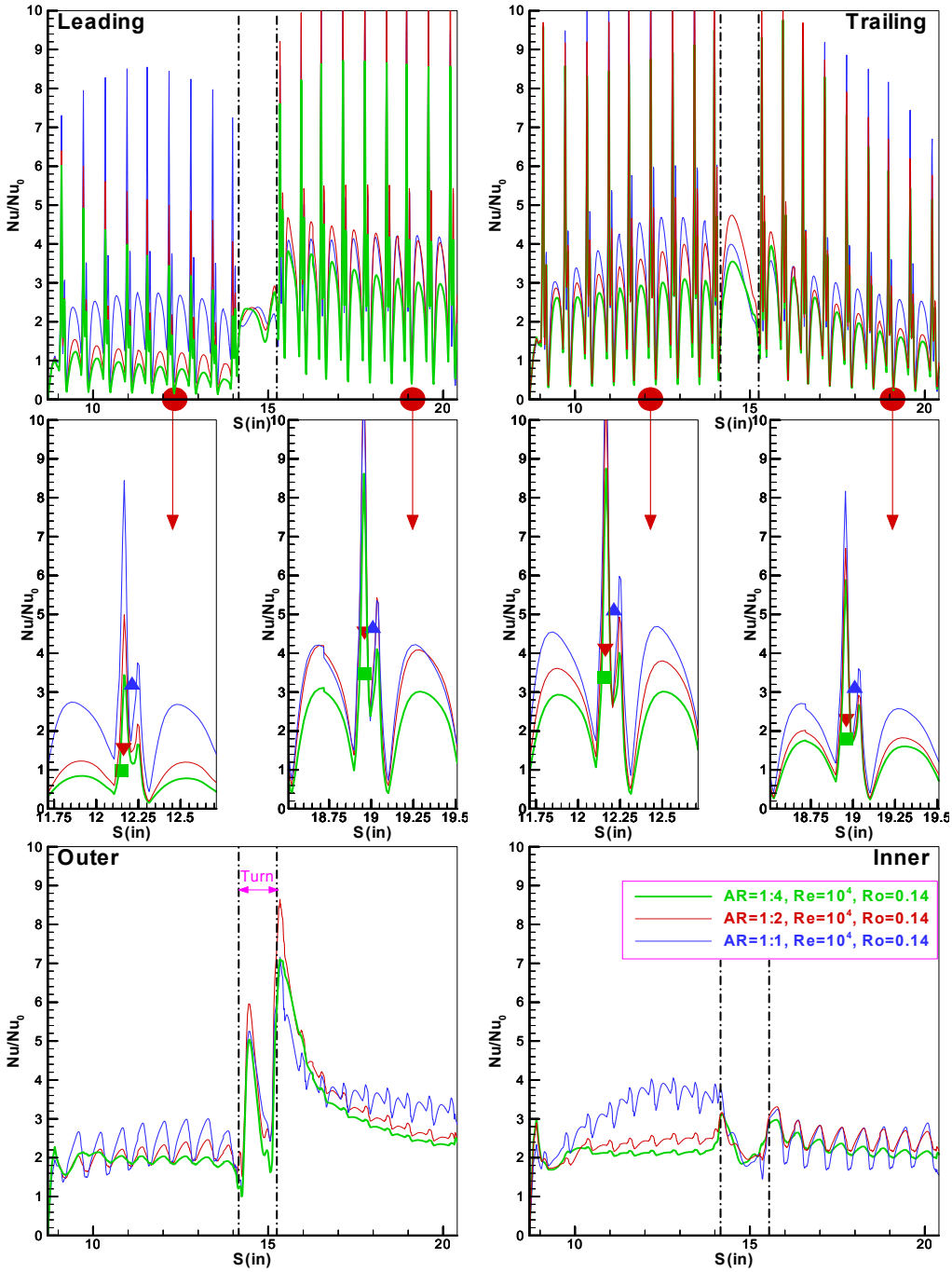

Fig. 6.8 Effect of Channel Aspect Ratio on Spanwise-Averaged Nusselt Number Ratios for Lower Reynolds Number (Ro=0.14, Re=10,000, $\Delta\rho/\rho$=0.13) Cases

the first passage and on the leading surface of the second passage were increased by rotation. In the first passage, the Coriolis force pushes colder fluid towards the trailing surface and the rotation-induced vortices brings hotter fluid back to the leading surface. Consequently, the Nusselt number ratios increase on the trailing surface and reduce on the leading surfaces in the first passage. This trend is reversed in the second passage since the Coriolis force acts in the opposite direction after the bend. As noted earlier, the square duct has the smallest hydraulic diameter, largest rib height-to-hydraulic diameter ratio (e/D_h), and highest inlet velocity for the same Reynolds number. Furthermore, the actual rotating speed is also significantly higher (inverse proportional to D_h^2) for the square duct under the same rotation number. Consequently, the Nusselt number ratios in square duct are higher in both the leading and trailing surfaces of the first passage. In the bend region and immediately after the turn, the highest heat transfer enhancement was still observed in the AR = 1:2 duct since it has the strongest bend-induced vortices. Further downstream in the second passage, the bend-induced vortices diminish gradually and the highest Nusselt numbers ratios were again observed in the AR = 1:1 duct due to the presence of stronger rotation-induced and rib-induced vortices in the ribbed square channel.

Effect of high Reynolds number and high rotation number on heat transfer coefficient distribution

In addition to the non-rotating and rotating ducts with a relatively low Reynolds number presented above (Cases 1-6), calculations were also performed for non-rotation cases at high Reynolds number (i.e. Case 7, 9, and 11) and high density ratio, and high

rotation number cases (i.e. Cases 8, 6, and 12) which are closer to power-generation turbine blade cooling conditions. In these calculations, the Reynolds number is increased from 10^4 to 10^5; the rotation number is doubled from 0.14 to 0.28; and the density ratio is increased from 0.13 to 0.2 and then to 0.4.

Fig.6.9 shows the detailed Nusselt number ratio contours of the leading and trailing surfaces for high Reynolds number cases. It is clearly seen that these Nusselt number ratio distributions are similar to those presented earlier in Fig. 6.6 for lower Reynolds number channels. However, the magnitude of the Nusselt number ratio decreases in both the non-rotating and rotating ducts when the Reynolds number is increased as also noted in Fig. 6.4 vs. Fig. 6.2 perimeter Nu ratios. For the non-rotating cases (Cases 7, 9 and 11), the effects of channel aspect ratios are still visible: when the aspect ratio decreases from 1:1 to 1:4, the Nusselt number ratios decrease since the larger rib roughness (e/D_h) and higher main flow velocity induced stronger secondary flow in the square duct. For the high density ratio and high rotation number conditions (Cases 8, 10 and 12), the effects of rotation lead to an increase of the heat transfer on the first pass trailing surface and a decrease of Nusselt number ratios on the first pass leading surface since the Coriolis force induced vortices push the cold fluid toward the trailing surface. The trend is reversed in the second passage as the Coriolis force acts in the opposite direction.

Fig. 6.10 shows the spanwise-averaged Nusselt number ratios for the non-rotating cases at two different Reynolds numbers of 10,000 and 100,000 for the three different aspect ratio channels. The Nusselt number ratios around rib 6 and rib 16 are also

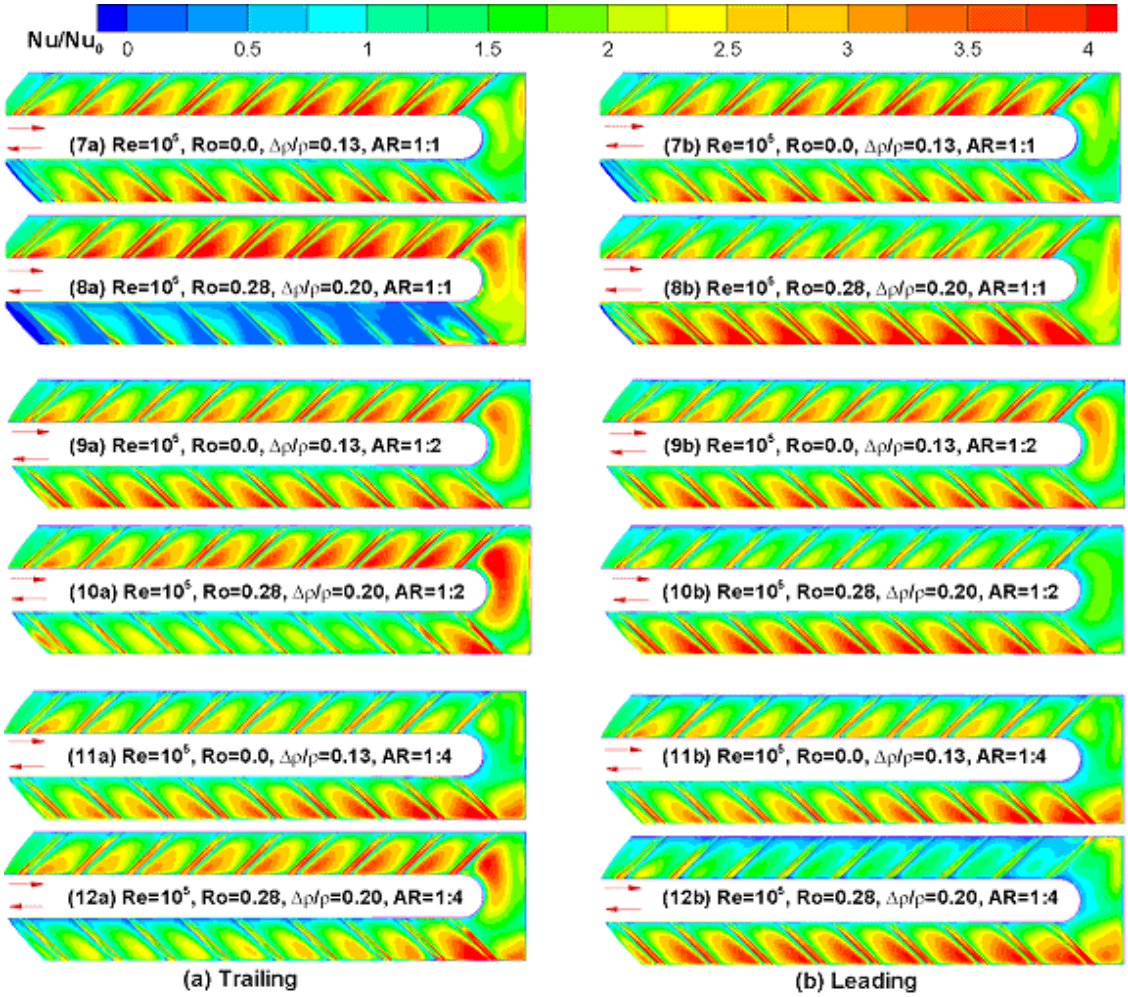

Fig. 6.9 Nusselt Number Ratio Contours on (a) Leading and (b) Trailing Surface for Higher Reynolds Number (Re = 100,000) Cases

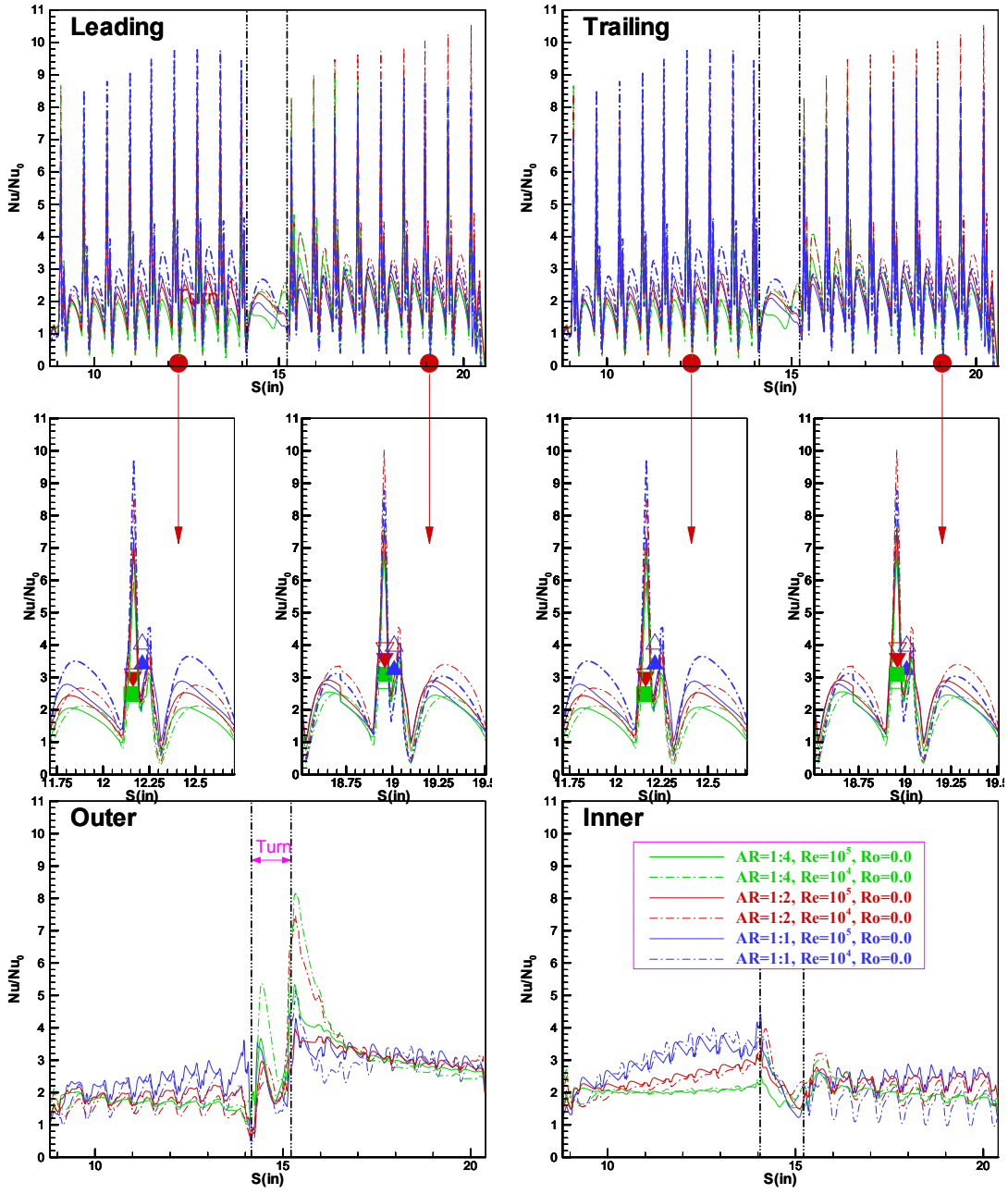

Fig. 6.10 Effect of Reynolds Number on Spanwised-Averaged Nusselt Number Ratios for Non-Rotating Duct with Aspect Ratio of 1:1, 1:2 and 1:4 (Ro=0.0, $\Delta\rho/\rho$=0.13)

enlarged as plots in Fig. 6.10**.** In general, the Nusselt number ratios Nu/Nu_0 on all four surfaces decrease as the Reynolds number increases. However, it should be noted that Nu_0 increases rapidly (proportional to $Re^{0.8}$) when the Reynolds number was increased from 10,000 to 100,000. Therefore, the actual heat transfer coefficients still increase very significantly at Re = 100,000 even though the heat transfer enhancement decreases.

In order to quantify the effects of rotation on different aspect ratio channels, it is desirable to examine the differences of Nusselt number ratios ($\Delta Nu/Nu_0$) between the leading and trailing surfaces directly for both the low and high rotation number cases. Fig.6.11 shows the $\Delta Nu/Nu_0$ distributions for the low-Re and low-Ro channels (Cases 2, 4 and 6) and high-Re, high-Ro channels to facilitate a detailed comparison of the rotation effects on different aspect ratio ducts. For the low Reynolds number and low rotation number cases, the strongest rotation effects were observed in the AR = 1:2 channel due to the presence of strong secondary flows in both the first and second passages as shown in Fig. 6.3. The effect of rotation reduces very significantly when the channel aspect ratio was reduced from AR = 1:2 to 1:4. As the rotation number increases from 0.14 to 0.28, the strength of the rotation-induced vortices increase rapidly while bend-induced as well as the rib-induced vortices remain about the same. Consequently, the highest differences in Nusselt number ratios were seen in the square duct which has the highest inlet velocity, largest e/D_h, and highest rotating speed under the same Reynolds number and the same rotation number conditions.

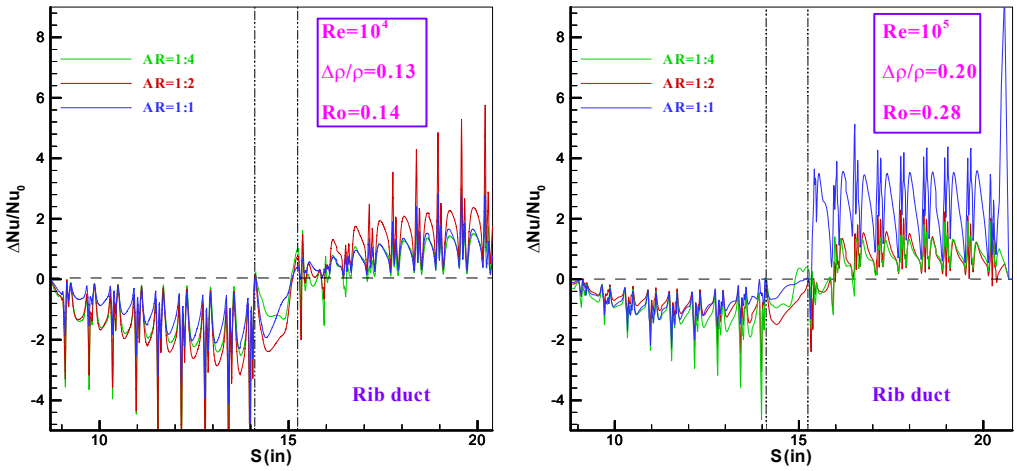

Fig. 6.11 Effect of Rotation on the Differences on Spanwised-Averaged Nusselt Number Ratios between the Leading and Trailing Surfaces for Rotating Ribbed Ducts of Aspect Ratios 1:1, 1:2, and 1:4

Effect of density ratio on heat transfer coefficient distribution

Fig. 6.12 shows the effect of inlet coolant-to-wall density ratio on the spanwise-averaged Nusselt number ratios for the rotating ducts with the different aspect ratios. The Nusselt number ratios on leading and trailing surface around rib 6 and rib 16 are enlarged as plots in Fig. 6.12**.** We will focus at the high Reynolds number (Re = 100,000) and high rotation number (Ro = 0.28) conditions with two different density ratios of 0.20 and 0.40 (i.e. case 8, 10, 12-15). In the first passage, an increase in density ratio leads to a decrease of heat transfer on the leading surface and a slight increase on the trailing surface in all three channels. This is because the centrifugal buoyancy force in the first passage acts in the same direction as the Coriolis force to increase the rotation effects. In the second passage, the rotational buoyancy force acts in the opposite direction of the Coriolis force. The Nusselt number ratios on the trailing surfaces of the AR = 1:2 and 1:4 ducts were dramatically reduced in the second passage when the density ratio was increased from 0.2 to 0.4. On the other hand, the density ratio has relatively small effect in the second passage of the square duct.

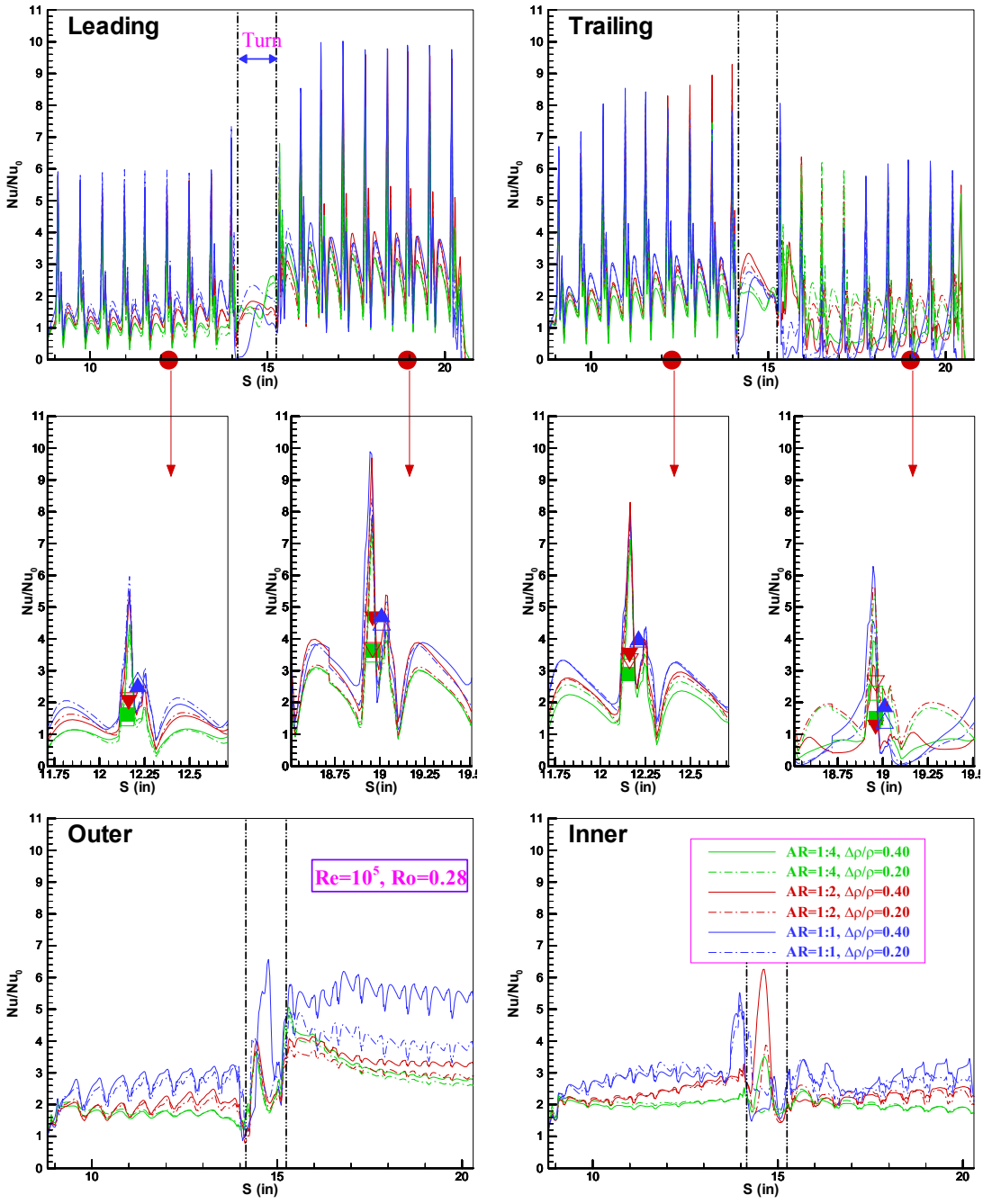

Fig. 6.12 Effect of Density Ratio on Spanwised-Averaged Nusselt Number Ratios for Rotating Duct with Aspect Ratio of 1:1, 1:2 and 1:4 (Re=100,000, Ro=0.28)

CHAPTER VII

SUMMARY AND CONCLUSIONS

A multi-block RANS method was employed to predict three-dimensional flow and heat transfer in rotating rectangular channel with several turbulators. It predicted fairly well the complex three-dimensional flow and heat transfer characteristics resulting from the different channel aspect ratios, rotation, centrifugal buoyancy forces, and channel orientation. The main findings from this study are summarized as follows.

For channel with V-shaped ribs:

1. The Nusselt number ratios predicted by the present near-wall second-moment closure model are in very good agreement with the experimental data for both the non-rotating and rotating cases.
2. The V-shaped ribs induce four counter-rotating vortices that oscillate in size along the streamwise direction. For the non-rotating case, the secondary flow results in steep temperature gradients and high heat transfer coefficients on the surfaces with V-shaped ribs as well as side walls.
3. For rotating cases, the rotation-induced cross-stream secondary flow distorts the V-shaped rib-induced vortices and affects the heat transfer on both the leading and trailing surfaces.
4. The V-shaped ribs create a symmetric heat transfer enhancement from the channel centerline towards the sidewalls. The rotation increases heat transfer enhancement

on the trailing surface and decreases heat transfer enhancement on the leading surface.

5. High Reynolds numbers tend to weaken the heat transfer enhancement effect of the V-shaped rib-induced secondary flow.
6. For high Reynolds number cases, an increase in rotation number and density ratio leads the Nusselt number ratios on the leading surface to further decrease, and the Nusselt number ratios on the side walls to further increase.

For channel with pin-fins:

1. The Nusselt number ratios predicted by the second moment closure model for both the non-rotating and rotating cases are in good agreement with the experimental data.
2. The pin-fins are very effective in heat transfer enhancement due to turbulent mixing caused by flow separation around the pin-fins and the formation of horseshoe vortices in the junction between the pin-fins and channel walls.
3. The Nusselt number ratio reaches a maximum value around the third row and decreases slightly towards the channel exit.
4. Both the rotation and density ratio have only minor effects on the heat transfer enhancement.
5. High Reynolds numbers tend to reduce the heat transfer enhancement effect of the pin-fins.

For smooth channels with different aspect ratios:

1. For non-rotating ducts, a pair of symmetric counter-rotating vortices was generated in the bend region. The highest heat transfer enhancement was observed in AR = 1:2

duct when the counter-rotating vortices grow to full strength and occupy the entire channel. As the aspect ratio reduces to AR = 1:4, the vortices and the heat transfer enhancements are confined to the leading and trailing surfaces.

2. For all three rotating ducts at $\beta = 90°$ channel orientation, the Coriolis force produce a pair of counter-rotating vortices perpendicular to the bend-induced vortices. The combined effects of rotation and turn lead to the growth of the vortex near the leading surface. The leading surface vortex continue to expand in the vertical direction as the channel aspect ratio was reduced from AR = 1:1 to AR = 1:4.
3. For all three different aspect ratio ducts, the Nusselt number ratios decrease with increasing Reynolds numbers. The friction factor ratios also decrease when the Reynolds number was increased from 10,000 to 100,000.
4. For non-rotating ducts, the channel aspect ratio has a small effect on spanwise-averaged Nusselt number ratio and friction factor ratio except for the turn region.
5. The channel rotation leads to higher heat transfer on first pass trailing surface and lower heat transfer on first pass trailing surface. This trend is reversed in the second pass. The effects of rotation on Nusselt number ratio become much more pronounced for low aspect ratio (AR = 1:2 and 1:4) rectangular channels.

For rib-roughed channels with different aspect ratios:

1. The calculations for three different aspect ratio channels were performed using the same channel width, the same rib height and rib pitch, but different channel heights. The square duct has the highest inlet velocity and highest rotating speed under the

same Reynolds number and same rotation number conditions since it has the smallest hydraulic diameter and largest e/D_h.

2. In the non-rotating channels, the size and strength of the secondary flow vary with the channel aspect ratio. In the first passage, the square duct (AR = 1:1) produced the highest heat transfer enhancement due to the relatively higher rib roughness, higher inlet velocity, and the strong mixing of the rib-induced secondary flows in the core region. In the second passage, however, the highest heat transfer enhancement were observed in the AR = 1:2 duct since the bend-induced secondary flow reaches maximum strength when the vortices are nearly circular and occupy the entire channel cross section.
3. For all three rotating ducts at Re = 10,000 and Ro = 0.14, the square duct again produced the highest heat transfer enhancement on both the leading and trailing surfaces of the first passage. High Nusselt number ratios were also obtained in the second passage far downstream away from the bend. In the 180° bend region, however, the AR = 1:2 channel still produces the highest Nusselt number ratios due to the presence of strong turn-induced vortices.
4. For the low-Ro and low-Re cases, the rotation effect on the Nusselt number is more significant in the AR = 1:2 channel than those observed in either the square or AR = 1:4 ducts due to the presence of strong turn-induced vortices. For the high-Ro and high-Re cases, however, the rotation effect decreases continuously when the channel aspect ratio was changed from AR = 1:1 to 1:2 and 1:4 since the bend-induced vortices are less important under the high rotation number conditions.

5. For all three different aspect ratio ducts, the heat transfer enhancement decreases when the Reynolds number was increased from 10,000 to 100,000.
6. At higher rotation number and higher Reynolds number, the density ratio increase has a dramatic effect on reduced heat transfer in the second passage of the lower aspect ratio duct. In general, the Nusselt number ratio decreases with increasing density ratios.

REFERENCES

[1]Stephens, M. A., Shih, T. I-P., and Civinskas, K. C., "Computation of Flow and Heat Transfer in a Rectangular Channel with Ribs," AIAA Paper 95-0180, January, 1995.

[2]Stephens, M. A., Chyu, M. K., and Shih, T. I-P., "Computation of Convective Heat Transfer in a Square Duct with Inclined Ribs of Rounded Cross Section," ASME Paper 96-WA/HT-12, 1996.

[3]Lin, Y.-L., Shih, T. I-P., Stephens, M. A., and Chyu, M. K., "A Numerical Study of Flow and Heat Transfer in a Smooth and a Ribbed U-duct with and without Rotation," *Journal of Heat Transfer*, Vol. 123, 2001, pp. 219-232.

[4]Prakash, C. and Zerkle, R., "Prediction of Turbulent Flow and Heat Transfer in a Ribbed Rectangular Duct with and without Rotation," *Journal of Turbomachinery,* Vol. 177, 1995, pp. 255-264.

[5]Bonhoff, B., Tomm, U., Johnson, B. V. and Jennions, I., "Heat Transfer Predictions for Rotating U-Shaped Coolant Channels with Skewed Ribs and with Smooth Walls," ASME Paper 97-GT-162, 1997.

[6]Iacovides, H., "Computation of Flow and Heat Transfer through Rotating Ribbed Passage," *International Journal of Heat and Fluid Flow*, Vol. 19, 1998, pp. 393-400.

[7]Chen, H. C., Jang, Y. J., and Han, J. C., "Computation of Heat Transfer in Rotating Two-pass Square Channels by a Second-Moment Closure Model," *International Journal of Heat and Mass Transfer*, Vol. 43, No. 9, May, 2000, pp. 1603-1616.

[8]Chen, H. C., Jang, Y. J., and Han, J. C., "Near-Wall Second-Moment Closure for Rotating Multi-pass Cooling Channels," *Journal of Thermophysics and Heat Transfer,* Vol. 14, No. 2, 2000, pp. 201-209.

[9]Jang, Y. J., Chen, H. C., and Han, J. C., "Computation of Flow and Heat Transfer in Two-Pass Channels with 60° Ribs," *Journal of Heat Transfer*, Vol. 123, No. 3, 2001, pp. 563-575.

[10]Jang, Y. J., Chen, H. C., and Han, J. C., "Numerical Prediction of the Flow and Heat Transfer in a Two-Pass Square Duct with 90° Ribs," *International Journal of Rotating Machinery,* Vol.7, No. 3, 2001, pp. 195-208.

[11]Ekkad S.V. and Han, J. C., "Detailed Heat Transfer Distributions in Two-Pass Square Channels with Rib Turbulators," *International Journal of Heat and Mass Transfer*, Vol. 40, No.11, 1997, pp. 2525-2537.

[12]Jang, Y. J., Chen, H. C., and Han, J. C., " Flow and Heat Transfer in a Rotating Square Channel with 45° Angled Ribs by Reynolds Stress Turbulence Model," *Journal of Turbomachinery*, Vol. 123, No. 1, 2001, pp. 124-132.

[13]Johnson, B. V., Wagner, J. H., Steuber, G. D., and Yeh, F. C., "Heat Transfer in Rotating Serpentine Passage with Trips Skewed to the Flow," *Journal of Turbomachinery*, Vol. 116, 1994, pp. 113-123.

[14]Al-Qahtani, M. S., Jang, Y. J., Chen, H. C., and Han, J. C., "Prediction of Flow and Heat Transfer in Rotating Two-Pass Rectangular Channels with 45° Rib Turbulators," *Journal of Turbomachinery*, Vol. 124, No. 2, 2002, pp. 242-250.

[15]Azad, G. S., Uddin, M. J., Han, J. C., Moon, H. K., and Glezer, B., "Heat Transfer in a Two-Pass Rectangular Rotating Channel with 45° Angled Rib Turbulators" *Journal of Turbomachinery*, Vol. 124, No. 2, 2002, pp. 251-259.

[16]Al-Qahtani, M. S., Chen, H. C., and Han, J. C., "A Numerical Study of Flow and Heat Transfer in Rotating Rectangular Channels (AR = 4) with 45° Rib Turbulators by Reynolds Stress Turbulence Model," *Journal of Turbomachinery*, Vol. 125, No. 1, pp. 19-26.

[17]Griffith, T. S., Al-Hadhrami, L. and Han, J. C., "Heat Transfer in Rotating Rectangular Cooling Channels (AR=4) with Angled Ribs," *Journal of Heat Transfer*, Vol. 124, No. 3, 2002, pp. 617-625.

[18]Jia, R., Saidi, A., and Sunden, B., "Heat Transfer Enhancement in Square Ducts with V-Shaped Ribs of Various Angles," ASME Paper GT-2002-30209, 2002.

[19]Han, J. C. and Park, J. S., "Developing Heat Transfer in Rectangular Channel with Rib Turbulators," *International Journal of Heat and Mass Transfer*, Vol. 31, No. 1, 1988, pp. 183-195.

[20]Han, J. C., Zhang, Y. M. and Lee, C. P., "Augmented Heat Transfer in Square Channels with Parallel, Crossed, and V-Shaped Angled Ribs," *Journal of Heat Transfer,* Vol. 113, 1991, pp. 590-596.

[21]Liou T.-M. Tzeng, Y.-Y., and Chen, C.-C., "Fluid Flow in a 180 Deg Sharp Turning Duct with Different Divider Thicknesses," ASME Paper 98-GT-189, 1998.

[22]Wagner, J. H., Johnson, B. V. and Kopper, F. C., "Heat Transfer in Rotating Serpentine Passage with Smooth Walls," *Journal of Turbomachinery*, Vol. 113, No. 3, 1991, pp. 321-330.

[23]Dutta, S. and Han, J. C., "Local Heat Transfer in Rotating Smooth and Ribbed Two-Pass Square Channels with Three Channel Orientations," *Journal of Heat Transfer*, Vol. 118, No. 3, 1996, pp. 578-584.

[24]Soong, C. Y., Lin, S. T., and Hwang, G. J., "An Experimental Study of Convective Heat Transfer in Radially Rotating Rectangular Ducts," *Journal of Heat Transfer*, Vol. 113, 1991, pp. 604-611.

[25]Wagner, J. H., Johnson, B. V., Graziani, R. A., and Yeh, F. C., "Heat Transfer in Rotating Serpentine Passages with Trips Normal to the Flow," *Journal of Turbomachinery*, Vol. 114, No. 4, 1992, pp. 847-857.

[26]Johnson, B. V., Wagner, J. H., Steuber, G. D., and Yeh, F. C., "Heat Transfer in Rotating Serpentine Passage with Selected Model Orientations for Smooth or Skewed Trip Walls," *Journal of Turbomachinery*, Vol. 116, 1994, pp. 738-744.

[27]Parsons, J. A., Han, J. C., and Zhang, Y. M., "Effects of Model Orientation and Wall Heating Condition on Local Heat Transfer in a Rotating Two-Pass Square Channel with Rib Turbulators," *International Journal of Heat and Mass Transfer*, Vol. 38, No. 7, 1995, pp. 1151-1159.

[28]Zhang, Y. M., Han, J. C., Parsons, J. A., and Lee, C. P., "Surface Heating Effect on Local Heat Transfer in a Rotating Two-pass Square Channel with 60 deg Angled Rib Turbulators," *Journal of Turbomachinery*, Vol. 117, 1995, pp. 272-280.

[29]Al-Hadhrami, L. and Han, J.C., "Effect of Rotation in Two-Pass Square Channels with Five Different Orientations of 45° Angled Rib Turbulators," *International Journal of Heat and Mass Transfer*, Vol. 46, 2003, pp. 653-669.

[30]Al-Hadhrami, L., Griffith, T. S., and Han, J.C., "Heat Transfer in Two-Pass Rotating Rectangular Channels (AR = 2) with Five Different Orientations of 45° V-shaped Rib Turbulators," *Journal of Heat Transfer*, Vol. 125, No. 2, 2003, pp. 232-242.

[31]Lee, E., Wright, L.M., and Han, J.C., "Heat Transfer in Rotating Rectangular Channels (AR=4:1) with V-Shaped and Angled Rib Turbulators with and without Gaps," ASME Paper No. GT-2003-38900.

[32]Metzger, D. E., Berry, R. A., and Bronson, J. P., "Developing Heat Transfer in Rectangular Ducts with Staggered Arrays of Short Pin-fins," *ASME Journal of Heat Transfer*, Vol. 104, 1982, pp. 700-706.

[33]Metzger, D. E. and Haley, S. W., "Heat Transfer Experiments and Flow Visualization for Arrays of Short Pin-fins," ASME Paper No. 82-GT-138, 1982.

[34]Metzger, D. E., Shepard, W. B., and Haley, S. W., "Row Resolved Heat Transfer Variations in Pin-Fin Arrays Including Effects of Non-Uniform Arrays and Flow Convergence," ASME Paper No. 86-GT-132, 1986.

[35]VanFossen, G. J., "Heat-Transfer Coefficients for Staggered Arrays of Short Pin-fins," *ASME Journal of Engineering for Power*, Vol. 104, 1982, pp. 268-274.

[36]Brigham, B. A. and VanFossen, G. J., "Length to Diameter Ratio and Row Number Effects in Short Pin-fin Heat Transfer," *ASME Journal of Engineering for Gas Turbines and Power*, Vol. 106, 1984, pp. 241-245.

[37]Chyu M. K. and Goldstein, R. J., "Influence of an Array of Wall-Mounted Cylinders on the Mass Transfer from a Flat Surface," *International Journal of Heat and Mass Transfer*, Vol. 34, No.9, 1991, pp. 2175-2186.

[38]Chyu, M. K. and Hsing, Y. C., "Convective Heat Transfer of Cubic Fin Arrays in a Narrow Channel," *ASME Journal of Turbomachinery*, Vol. 120, 1998, pp. 362-367.

[39]Chyu, M. K., Hsing, Y. C. and Shih, T.I.-P., "Heat Transfer Contributions of Pins and Endwall in Pin-Pin Arrays: Effects of Thermal Boundary Condition Modeling," ASME Paper No. 98-GT-175, 1998.

[40]Uzol, O. and Camci, C., "Elliptical Pin-fins as an Alternative to Circular Pin-fins for Gas Turbine Blade Cooling Applications, Part 1: Endwall Heat Transfer and Total Pressure Loss Characteristics," ASME Paper No. 2001-GT-0180, 2001.

[41]Hwang, J., and Lui, C., "Measurement of Endwall Heat Transfer and Pressure Drop in a Pin-Fin Wedge Duct", *Int. J. of Heat and Mass Transfer*, Vol. 45, 2001, pp. 877-88.

[42]Hwang, J., Lia, D. Y. and Tsia, J. P., "Heat Transfer and Pressure Drop in Pin-Fin Trapezoidal Ducts," ASME Paper No. 98-GT-110, 1998.

[43]Lau, S. C., Kim, Y. S., and Han, J. C., "Local Endwall Heat /Mass Transfer Distributions in Pin Fin Channels," *AIAA Journal of Thermophysics and Heat Transfer*, Vol. 1, 1987, pp. 365-372.

[44]Lau, S. C., Han, J. C., and Kim, Y. S., "Turbulent Heat Transfer and Friction in Pin Fin Channels with Lateral Flow Ejection," *ASME Journal of Heat Transfer,* Vol. 111, 1989, pp. 51-58.

[45]Lau, S. C., Han, J. C., and Batten, T., "Heat Transfer, Pressure Drop, and Mass Flow Rate in Pin Fin Channels with Long and Short Trailing Edge Ejection Holes," *ASME Journal of Turbomachinery*, Vol. 111, 1989, pp. 116-123.

[46]Willett, F. T. and Bergles, A. E., "Heat Transfer in Rotating Narrow Rectangular Pin-Fin Ducts," *Experimental Thermal and Fluid Science,* Vol. 25, 2002, pp. 573-582.

[47]Willett, F. T. and Bergles, A. E., "Heat Transfer in Rotating Narrow Rectangular Ducts with Heated Sides Oriented at 60°to the R-Z Plane," ASME Paper No. 2000-GT-224, 2000.

[48]Wright, L. M., Lee, E., and Han, J. C., "Effect of Rotation on Heat Transfer in Narrow Rectangular Cooling Channels (AR = 8:1 and 4:1) with Pin-Fins," ASME GT2003-38340, 2003.

[49]Donahoo, E. E., Kulkarni, A. K., Belegundu, A. D., and Camci, C., "Determination of Optimal Row Spacing for a Staggered Cross-Pin Array in a Turbine Blade Cooling Passage," *Journal of Enhanced Heat Transfer,* Vol. 8, 2001, pp. 41-53.

[50]Donahoo, E. E., Camci, C., Kulkarni, A. K., and Belegundu, A. D., "A Computational Visualization of Three Dimensional Flow: Finding Optimum Heat Transfer and Pressure Drop Characteristics from Short Cross-Pin Arrays and Comparison with Two-Dimensional Calculations," ASME Paper 99-GT-257, ASME Turbo Expo 1999, June 7-9, Indianapolis, Indiana, USA.

[51]Hamilton, L. J., Adametz, D. S., Lind, E. K., and Gropinath, A., "Numerical Analysis of the Performance of a Staggered Cross-Pin Array Heat Exchanger," 8th AIAA/ASME Joint Thermophysics and Heat Transfer Conference, 2002.

[52]Parsons, J. A., Han, J. C., and Zhang, Y. M., "Wall Heating Effect on Local Heat Transfer in a Rotating Two-Pass Square Channel with 90° Rib Turbulators," *Int. J. Heat Mass Transfer*, Vol. 37 (9), 1994, pp. 1411–1420.

[53]Parsons, J.A., Han, J. C., and Zhang, Y. M., "Effects of Model Orientation and Wall Heating Condition on Local Heat Transfer in a Rotating Two-Pass Square Channel with Rib Turbulators*," Int. J. Heat Mass Transfer*, Vol. 38 (7), 1995, pp. 1151– 1159.

[54]Dutta, S., Han, J. C., and Lee, C. P., "Local Heat Transfer in a Rotating Two-Pass Ribbed Triangular Duct with Two Model Orientations," *Int. J. Heat Mass Transfer*, Vol. 39, 1996, pp. 707–715.

[55]Park, C. W., and Lau, S. C., "Effect of Channel Orientation of Local Heat (Mass) Distributions in a Rotating Two-Pass Square Channel with Smooth Walls," *ASME J. Heat Transfer,* Vol. 120, 1998, pp. 624–632.

[56]Park, C. W., Yoon, C., and Lau, S. C., "Heat (Mass) Transfer in a Diagonally Oriented Rotating Two-Pass Channel with Rib-Roughened Walls," *ASME J. Heat Transfer*, Vol. 122, 2000, pp. 208–211.

[57]Chen, Y., Nikitopoulos, D. E., Hibbs, R., Acharya, S., and Myrum, T. A., "Detailed Mass Transfer Distribution in a Ribbed Coolant Passage with a 180° Bend," *Int. J. Heat and Mass Transfer*, Vol. 43, 2000, pp. 1479-1492.

[58]Al-Hadhrami, L., and Han, J. C., "Effect of Rotation on Heat Transfer in Two-Pass Square Channels with Five Different Orientations of 45° Angled Rib Turbulators," *Int. J. Heat and Mass Transfer*, Vol. 46, 2003, pp. 653-669.

[59]Liou, T. M., Tzeng, Y. Y., and Chen, C. C., "Fluid Flow in a 180 Degree Sharp Turning Duct with Different Divider Thicknesses," *ASME J. Turbomachinery*, Vol. 121, 1999, pp. 569-575.

[60]Liou, T. M., and Chen, C. C., "LDV Study of Developing Flows through a Smooth Duct with a 180 Degree Straight-Corner Turn," *ASME J. Turbomachinery*, Vol. 121,1999, pp. 167-174.

[61]Liou, T. M., and Chen, C. C., "Heat Transfer in a Rotating Two-Pass Smooth Passage with a 180° Rectangular Turn," *Int. J. Heat And Mass Transfer*, Vol. 42, 1999, pp. 231-247.

[62]Hubbard, B. J. and Chen, H. C., "A Chimera Scheme for Incompressible Viscous Flows with Applications to Submarine Hydrodynamics," AIAA Paper 95-2210, 1995.

[63]Fu, W.L., Wright, L. and Han, J.C. **,** **"**Heat Transfer in Two-Pass Rotating Rectangular Channels (AR=1:2 and AR=1:4) with 45° Angled Rib Turbulators", ASME Paper GT-2004-38651, 2004.

VITA

Guoguang Su was born on July 12, 1969 in Lai Zhou, Shandong, China. He received his B.S. degree in July 1992 from Chongqing University and his M.S. degree in July 1999 from the Chinese Academy of Science, both in mechanical engineering. He worked at the Chinese Academy of Science before he came to Texas A&M University for his Ph.D. degree in September 2001. He worked as a Research Assistant at the Turbine Heat Transfer Laboratory and received his Ph.D. degree in December 2005.

Department of Mechanical Engineering

Texas A&M University

College Station, TX 77843-3123